Ion Transport in Temperature Sensitive Polyelectrolytes

Thesis by
Linghui Wang

In Partial Fulfillment of the Requirements for the
Degree of
Doctor of Philosophy in Applied Physics

Caltech

CALIFORNIA INSTITUTE OF TECHNOLOGY
Pasadena, California

2023
Defended Feburary 22, 2023

ACKNOWLEDGEMENTS

I would like to thank all people who have helped, supported, and accompanied me through my Ph.D. First of all, I would like to express my deepest gratitude to my supervisor, Professor Chiara Daraio, for her invaluable guidance and support over these years. Her intelligence, enthusiasm for research, and kindness have greatly inspired me. I am truly grateful for her belief in me and for the opportunity to learn and work in her lab. Also, I would like to extend my appreciation to Professor Zhen-Gang Wang for providing me with feedback and support throughout my research. Furthermore, I would like to thank the rest of my thesis committee members, Professor Austin Minnich and Professor Marco Bernardi, for their advice on my research directions and for agreeing to be on my thesis committee.

This thesis would not have been possible without the support and help of the Daraio group members and many other Caltech members. I especially would like to thank the following collaborators: Vincenzo Costanza, a remarkable researcher, who helped me immensely with experiments and also shared his knowledge on this project with me; Nick Higdon, who taught me a lot about organic chemistry and density functional theory; Luca Bonanomi, for helping me get started with my research in the lab and giving me advice on both research and life; Kevin Kim, for giving me guidance in setups and fabrication techniques. I must also thank Connor McMahan, Gunho Kim, Eleftheria Roumeli, Behrooz Yousefzadeh, Edmond Zhou, Ahmad Omar, Alexandros Tsamopoulos, and Jingjing Jiang for a wide range of helpful discussions. I also wish to thank Dr. Bruce S. Brunschwig for helping me with the infrared spectroscopy. Additionally, I'd like to acknowledge Carolina Oseguera, Lynn Seymour, and Jennifer Blankenship for their great administrative work.

I am also grateful for all my friends who have made this journey more enjoyable. I appreciate the countless words of encouragement and the many moments of laughter and joy shared. It is impossible for me to list all of them, but I especially would like to thank YingShi Teh, Ge Chen, and Weiyi Tang for their support and lasting friendship.

Last, I am infinitely grateful for my mon Xiaohuang Wang and my dad Jiehua Hou, who have always shown unwavering faith in me and offered me wholehearted support. I also would like to express my deep appreciation to my grandfather Shibo

Wang, who served as a constant source of inspiration throughout my life.

ABSTRACT

Temperature sensors are widely employed and play a key role in many industries, such as automotive vehicles, medical devices, environmental monitoring, and process control. The state-of-the-art thermal sensing elements are made of rigid and costly inorganic materials, such as vanadium oxide and platinum. These materials have limitations for emerging applications such as wearable devices and prosthetic devices. Ideal temperature sensing materials for such applications need to be flexible, reliable under mechanical deformation, and suitable for large-area production. Electrical conductive polymers were found to be a promising solution because of their flexibility and solution processability. However, they often lag in temperature resolution compared to their inorganic counterparts.

A recent discovery revealed that the ionic conductivity of crosslinked pectin, a biopolymer extracted from plant cell walls, has a record-high temperature response. It is biocompatible, flexible when hydrated, and solution-processable, making it a strong candidate for wearable temperature sensing and conformal temperature mapping. However, open questions remain about the origin of its temperature sensitivity and the principles governing its ion transport. Furthermore, the heterogeneity of the complex molecular structure of pectin presents challenges to its integration in sensing devices.

In this thesis, we study the origin of the high thermal sensitivity in pectin and develop a synthetic polyelectrolyte that mimics its key structure and properties. In Chapter 3, we focus on the ion transport mechanism in crosslinked pectin. We show that the binding between multivalent ions and certain chemical functional groups of pectin plays a critical role in its temperature sensitivity. In Chapter 4, the impact of water content on the ion transport and dielectric processes in crosslinked pectin is also investigated. In the following chapter, we present a novel synthetic polyelectrolyte designed to mimic pectin with a simpler structure. It has superior flexibility, high temperature sensitivity, and is stable under mechanical deformation. To further study this new material, we examine its ion transport dynamics under varying humidity and temperature conditions in Chapter 7. We discover that temperature and humidity have a similar effect on ion transport. Overall, we showed a biomimetic approach to design temperature sensitive polymers where the strong ion-polymer binding is the key to the ultrahigh temperature response.

PUBLISHED CONTENT AND CONTRIBUTIONS

[1] Vincenzo Costanza, Luca Bonanomi, Giovanni Moscato, Linghui Wang, Yeong Suk Choi, and Chiara Daraio. Effect of glycerol on the mechanical and temperature-sensing properties of pectin films. *Applied Physics Letters*, 115(19):193702, 2019. doi: 10.1063/1.5121710.
L. W. performed the infrared spectroscopy and corresponding data analysis.

[2] Tae Hyun Kim, Zhun Zhou, Yeong Suk Choi, Vincenzo Costanza, Linghui Wang, Joong Hwan Bahng, Nicholas J Higdon, Youngjun Yun, Hyunbum Kang, Sunghan Kim, and Chiara Daraio. Flexible biomimetic block copolymer composite for temperature and long-wave infrared sensing. *Science Advance, in press*, 2023.
L. W. contributed to the conception of the project and the design of the research. L. W. participated in building the setup and in performing electrical characterizations, preliminary material development, mechanical tests, and data analysis.

[3] Linghui Wang and Chiara Daraio. Effect of water content on the ion transport in pectin films. *Under preparation*, 2023. L. W. participated in the conception of the project and the design of this project. L. W. conducted the electrical measurement and data analysis. L. W. participated in writing and revising the manuscript.

[4] Linghui Wang*, Vincenzo Costanza*, Nicholas J Higdon, Tae Hyun Kim, and Chiara Daraio. Ion transport phenomena in thermally responsive polyelectrolytes. *in preparation*, 2022.
L. W. and V. C. contributed equally to this work. L. W. participated in the conception of the project and the design of the research. L. W. performed DSC measurements and data analysis. L. W. participated in electrical characterization and analysis. L. W. participated in the writing and revising of the manuscript.

[5] Linghui Wang, Tae Hyun Kim, Vincenzo Costanza, Nicholas J Higdon, and Chiara Daraio. Ion transport in thermally responsive pectin films. *Under review, Applied Physics Letters*, 2023. L. W. participated in the conception of the project and the design of this project. L. W. conducted out the electrical measurement, infrared spectroscopy and data analysis. L. W. participated in writing and revising the manuscript.

TABLE OF CONTENTS

LIST OF TABLES

LIST OF ILLUSTRATIONS

Chapter 1

INTRODUCTION

1.1 Research objectives

The primary goal of this work is to understand and develop temperature-sensitive polymer electrolytes for applications such as conformal temperature sensing and uncooled infrared sensing. The specific objectives are:

- Understand the ion transport and thermal sensing mechanism of the biopolymer pectin.

- Develop a pectin-mimicking synthetic polyelectrolyte with higher temperature sensitivity and increased flexibility.

- Study how ion transport is affected by temperature and humidity in this synthetic polyelectrolyte.

This work offers physical insights into the ion transport phenomenon in temperature sensitive polyelectrolytes and provides new directions for the development of thermal sensing material.

1.2 Advantages of organic electronics

An increased interest in devices fabricated with organic materials has emerged in recent decades. Compared to traditional silicon-based electronics, organic devices, including polymer-based devices, have many advantages, such as stretchability, flexibility, low cost, light weight, large-area processability, and biocompatibility [1, 2]. Most organic materials are processed in liquid solutions and, therefore, can be fabricated to satisfy unique form factors [2]. In addition, compared to common techniques for fabricating inorganic devices, such as evaporation deposition and sputtering, which typically require a vacuum and high temperatures, solution processing techniques, such as spray coating, spin coating, screen printing, inkjet printing, and gravure printing, are more energy -efficient and cos t-effective [1]. Especially, due to the flexibility of organic devices, roll-to-roll processing can be easily achieved, enabling high-throughput, large-area, and low-cost production [3]. Another attractive feature of organic materials is their flexibility, which is

especially important for applications such as flexible displays, wearable electronics, robotics, and artificial skin. One popular strategy for making flexible devices is to embed inorganic fillers in flexible and insulating materials, such as graphene-polymer composites and metal-polymer composites [4–6]. However, the electrical conductivity of these composite materials is typically percolation dependent, which leads to undesirable properties, such as strain sensitivity, low conductivity, and low cycle stability [7]. The intrinsically flexible organic materials are therefore more desirable. Furthermore, the immense design space of organic materials allows one to optimize multiple material properties simultaneously by tailoring molecular structures and compositions, which is appealing for a wide range of applications such as flexible electronics. Additionally, many organic materials can be easily functionalized and are compatible with other types of materials.

One of the most successfully commercialized organic electronics is the organic light-emitting diode (OLED). OLEDs contain an electroluminescent layer made of conjugated organic molecules with delocalized electrons [8]. With the applied bias, electrons and holes are transported across neighboring molecules via the overlapping π-orbitals. In the end, they combine and form excitons, which decay with photon emission. Other types of devices that utilize conjugated molecules, such as organic photovoltaics and organic transistors, have also seen significant advancements in terms of mass production and commercialization.

Besides electron-conducting organic materials, ion-conducting polymer electrolytes are also widely used as active materials in flexible organic devices. Most previous research on polymer electrolytes focuses on energy storage and conversion applications, such as lithium-ion batteries and fuel cells. However, in recent years, polymer-electrolyte-based electronics for actuation and sensing have also gained increasing attention, such as bending actuators [9, 10], gas sensing [11, 12], touch sensing [13], humidity sensing [14, 15] and temperature sensing [16–18]. For most of these applications, ion transport plays a critical role. For example, poly(mercaptopropyl polyhedral oligomeric silsesquioxane-1,4-divinylbenzene-sodium p-styrene sulfonate hydrate) (PMDS) has been shown to have a fast and large response to humidity and can be used for respiration monitoring [19]. Its ionic conductivity increases by two orders of magnitude when the relative humidity (RH) increases from 54% to 95%. This increase in ionic conductivity was attributed to the hydration-driven ionization of Na^+ and H_3O^+.

1.3 Organic temperature sensors

Motivations for thermal sensing

Temperature sensors are extensively utilized and are indispensable in many industries, such as automotive vehicles, medical devices, environmental monitoring, and process control [20–22]. The temperature sensitivity of a temperature sensor is usually described by the temperature coefficient α:

$$\alpha = \frac{1}{R}\frac{dR}{dT} \tag{1.1}$$

where R is the temperature-dependent physical property of the sensing material and T is the temperature. Currently, commercially available temperature sensors are based on inorganic materials and are divided into three categories: i) resistive temperature detectors (RTD), ii) thermistors, iii) thermocouples. RTDs are based on metals, such as platinum and copper. Their resistance linearly increases with temperature, making them easy to measure and calibrate. However, their temperature sensitivity is generally low, with an α of 0.003925 Ω/(Ω·°C) for platinum[23]. On the other hand, thermistors, usually made of semiconductors such as metal oxides, exhibit high sensitivity to temperature. However, they are limited by the small sensing temperature range and suffer from drifting issues due to the aging of semiconductor materials [24]. Thermocouples are composed of two different metal wires that are fused to form a junction. Due to the Seebeck effect, the voltage across the junction is dependent on temperature differences between the fused junction and a reference junction. To obtain an absolute temperature reading, either a thermal bath is needed to keep the reference junction at a constant known temperature or an independent measurement of temperature at its reference junction is required, which complicates the circuitry and fabrication. In the latter case, the accuracy of the temperature measurement relies on accurately measuring and compensating for the temperature at the reference junction. Thermocouples are renowned for their broad temperature measurement range and rapid response. Nevertheless, the output voltage they produce is relatively low, typically in the millivolt range. This necessitates the use of meticulous voltage measurement techniques to achieve accurate temperature readings [25]. In general, thermocouples exhibit lower accuracy compared to resistance temperature detectors (RTDs) and are prone to drift under high temperature and pressure conditions [24] . Overall, these temperature sensors are made of rigid inorganic materials. Although they have been sufficient for a variety of traditional applications albeit their drawbacks, new technology is required for emerging industries and applications such as wearable devices and uncooled

infrared sensing.

Wearable technology has rapidly developed in the recent decade and has the potential to revolutionize healthcare. It continuously senses and collects physiological data, providing valuable information for health diagnosis, disease monitoring, and disease prevention [26]. These small portable medical devices usually consist of sensors that can track vital signs, such as heart rate, temperature, and blood pressure. Among these physiological data, temperature measurement is particularly important. In fact, the local temperature increase is widely recognized as a cardinal sign of inflammation. As a result, being able to map temperature on skin or other tissue is critical for the prevention and monitoring of health conditions. For example, studies found that for patients with diabetic feet, once daily foot temperature monitoring could significantly lower the rate of hospitalizations and extremity amputation [21]. To obtain accurate and precise temperature measurements on the skin, the sensor used must be conformable, flexible, and remain reliable when subject to deformation. Traditional rigid temperature sensing materials are not suitable for this purpose. As such, organic temperature-sensing materials are needed.

Organic temperature sensors can also be beneficial for infrared sensing technologies. Thermal imaging has been increasingly adopted by civilian applications, such as automobiles, medical devices, and security systems, which require uncooled detectors with low cost [27]. The vanadium-oxide-based microbolometer is the most widely used type of uncooled detector[28]. A vanadium oxide microbolometer comprises three layers, including a layer of vanadium oxide as thermal sensing (2-3%/K) [29], a layer for infrared absorber, and a layer for thermal insulation. The reason for the latter two additional layers is that vanadium oxide has a high reflection at far-infrared regions and relatively high thermal conductivity, making the fabrication costly and large-area production challenging [30]. This process could be avoided with a thermally sensitive material with good infrared absorption, low thermal conductivity, and large-area processability. Organic materials are promising candidates for this purpose [30, 31].

State of the art of organic temperature sensing material

High temperature sensitivities have been reported with conductive-filled polymer composites [6, 32]. Its temperature sensitivity originates from changes in the specific volume with temperature when the polymer goes through a melting transition. As such, its sensing temperature range is limited only to the transition region ($< 5°C$).

Many other temperature sensitive inorganic-polymer composites have been studied, but they suffer from problems such as low cycle stability and strain sensitivity, as mentioned above [7]. There are a few reports of pure organic temperature-sensitive materials, but they showed a much lower sensitivity compared to their inorganic counterparts. For example, electron conducting polymer PEDOT:PSS has been suggested for bolometer application and shows only 0.6%/K temperature sensitivity [33]. Poly(acrylic acid)-polyaniline nanofiber hydrogel (PANI NF) shows a higher response of 1.64%/K, but its temperature resolution (2.7 °C) is still too low for temperature mapping or infrared sensing applications [17].
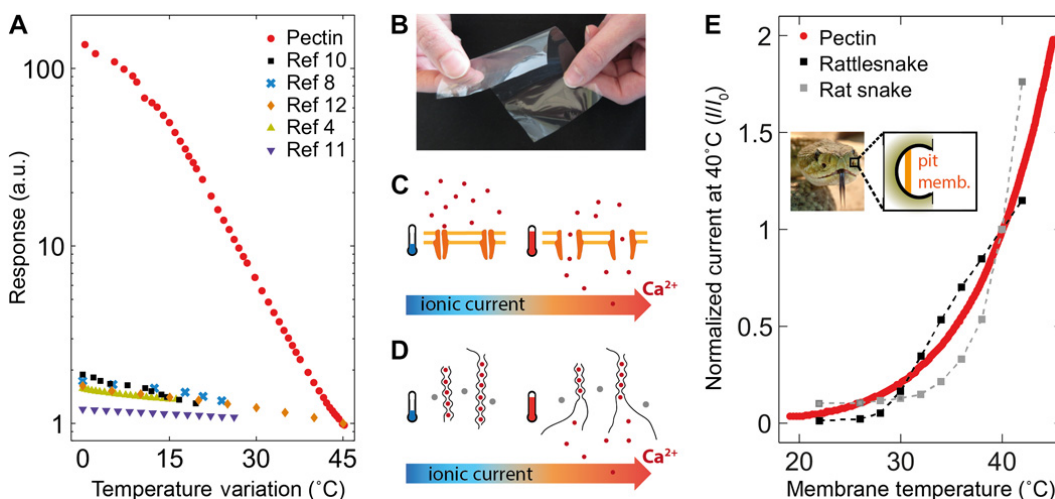
Figure 1.1: Response of pectin films compared to other flexible temperature sensing materials and snakes' pit membrane. (A) Comparison between pectin and other flexible temperature sensing materials. Here, response is defined as the normalized signal variation. Red dot, resistance of crosslinked pectin film; black squares, resistance replotted from Park et al. [34]; blue crosses, resistance replotted from Segev-Bar et al. [35]; orange diamonds, resistance replotted from Trung et al. [36]; green triangles, voltage replotted from Kim et al. [37]; violet triangles, resistance replotted from Webb et al. [38]. (B) A crosslinked pectin film showing good flexibility. (C) Temperature sensing mechanism of snake pit membrane. (D) Proposed temperature sensing mechanism of crosslinked pectin films. (D) Comparison between crosslinked pectin and snake pit membranes. This figure is reprinted with permission from [16]

.

Recently pectin, a biopolymer usually extracted from fruit peels, has been found to have record-breaking temperature response when crosslinked with $CaCl_2$ [16]. Pectin is a structural polysaccharide in the plant cell wall. Although its exact structure is still under debate, its main backbone is composed of a linear chain of α-(1,4)-linked galacturonic acid residues, which are partially esterified. Pectin with a low degree of esterification can be crosslinked by divalent ions such as calcium

ions and form a gel. Due to its gelation properties, pectin has been widely used as a gelling agent in the food and pharmaceutical industries. Previous research focused on the binding of divalent cations to pectin and its rheological properties in the hydrated state. The recent research discover for the first time that when crosslinked pectin is dehydrated, its ionic conductivity increases by more than two orders of magnitude when temperature increases from 10 °C to 55 °C. 10 millikelvin sensitivity was demonstrated between 10°C and 55°C, which is more than an order of magnitude higher than previously reported flexible sensors with this temperature range [16]. A similar temperature response to the crosslinked pectin can only be found in nature: snakes' pit membrane, which is a sensory organ in pit vipers used to detect thermal emission from prey [16]. Furthermore, pectin is a suitable material for skin temperature mapping as it can be solution-processed and forms conformal coatings. Additionally, large-scale production of thin pectin films can be achieved through printing and spin coating, and it has moderate absorption in the far infrared region, making it useful for infrared sensing.

While polymer electrolyte as temperature-sensing material is gaining increasing attention, the underlying mechanism of their temperature response has not been investigated in detail. As for crosslinked pectin, the high temperature response was observed only when $CaCl_2$ was added. This suggests that the interaction between pectin and $CaCl_2$ is responsible for the high temperature response. However, the specific mechanism for increasing conductivity at high temperatures is unknown. The increasing ionic conductivity with rising temperature could be a result of either increase in the ion mobility or the mobile ion number density. A systematic understanding of the origin of their temperature sensitivity is imperative to advance the development of temperature sensitive polymers. To gain a deeper insight into the ion transport process, we will start by reviewing some basics of ion transport mechanisms that are relevant to the research presented in this thesis.

1.4   Ion transport in polymer electrolyte

Polymer electrolytes are a type of polymer that could solvate ionizable species and support ion transport. Compared to small-molecule electrolytes, polymer electrolytes possess better mechanical flexibility, strength, and processibility. It also has higher flaming points and better electrochemical stability, making it a safer material than many conventional organic solvents [39].

In the dilute limit, the ion transport is governed by the Nernst-Planck equation [39]:

$$J = \sum_i (-D_i \nabla n_i + \mu_i n_i \nabla \phi) \tag{1.2}$$

where J is the current density, ϕ is the electric potential, D_i, n_i and μ_i are the diffusion coefficient, the concentration, and the mobility of ion type i. The contribution from the convection in the polymer electrolyte is usually negligible and is not included in equation 1.2. By Ohm's law, the ionic conductivities can be written as Kohlrausch summation:

$$\sigma = \sum_i \sigma_i = \sum_i \mu_i q_i n_i. \tag{1.3}$$

The relationship between the mobility and the diffusion constant follows the Einstein relation:

$$\mu_i = \frac{D_i q}{k_B T}. \tag{1.4}$$

Assuming an ideal electrolyte, i.e. no interaction between ions, the ionic conductivity follows the Nernst-Einstein relation:

$$\sigma_{NE} = \frac{1}{k_B T} \sum_i N_i q_i^2 D_i \tag{1.5}$$

Consider the diffusion process as a random walk with average jumping distance a and the average time between jump τ, $D = \frac{a^2}{6\tau} = \frac{a^2 \nu^*}{6}$ [40]. Then, we have

$$\sigma_i = \frac{n_i q_i^2 a_i^2}{6 k_B T} \nu_i^*. \tag{1.6}$$

The ion mobility can be written as :

$$\mu_i = \frac{q_i D_i}{k_B T} = \frac{a_i^2 q_i}{6 k_B T} \nu^*, \quad t^* = 1/\nu^*. \tag{1.7}$$

In the non-ideal electrolyte, ion motions can be correlated due to the formation of ion pairs, ion clusters, or collective motions. The nonideality is usually quantified using Haven's ratio defined as:

$$H = \frac{\sigma_{NE}}{\sigma}. \tag{1.8}$$

H being much larger than unity indicates strongly correlated ion motions[41].

Ion transport in amorphous polymer above glass transition usually happens through the following two mechanisms: i) vehicular transport, where ions diffuse together with an entire polymer chain, ii) fluctuation-driven diffusion [39], where the ion hopping is assisted by the segmental motion of polymer chains. For polymer

electrolytes with high molecular weight, only the second mechanism would be present. For ion transport coupled with polymer motion, the temperature dependence of ionic conductivity usually follows an empirical model called Vogel-Fulcher-Tammann(VFT) model [42]:

$$\sigma(T) = A \exp\left(-\frac{B}{k_B(T - T_0)}\right) \tag{1.9}$$

where A is the pre-exponential factor depending on the concentration of ions and corresponds to the intrinsic conductivity at infinitely high temperature, B is the pseudo-activation energy, k_B is the Boltzmann constant and T_0 is called the Vogel temperature or equilibrium glass transition temperature. T_0 has been empirically found to be 50 °C below the glass transition temperature of polymer electrolyte [42].

For polymer electrolytes below the glass transition temperature, since the segmental motion is essentially frozen, ionic conduction happens mainly through ion hopping among its solvation sites in the frozen matrix. This process involves the exchange of solvating particles of ions and the hopping dynamics is strongly influenced by the ion solvation environments. Its temperature dependence usually follows the Arrhenius equation:

$$\sigma(T) = A \exp\left(-\frac{E_A}{k_B T}\right) \tag{1.10}$$

where A is the pre-exponential factor and E_A is the activation energy.

Polymer electrolytes could be divided into three categories. i) salt-doped polymer electrolyte, ii) dry polyelectrolyte, also called single-ion conductors, and iii) solvated polyelectrolyte [39]. Salt-doped polymer electrolytes are polymeric solvents with salt dissolved in it. One famous example of this is the LiTFSI doped poly(ethylene oxide) (PEO), a solid electrolyte for lithium-ion battery applications. In the 1970s, PEO was found to dissolve lithium salt without a small-molecule solvent and show a surprisingly good ionic conductivity (10^{-3} S/cm). Through simulation, it was observed that multiple oxygen atoms in the PEO polymer chain could coordinate with lithium ions and provide solvation. Above the melting temperature, lithium ions conduct mainly through hopping and co-diffusion with the polymer chain in the amorphous phase of the polymer [43].

Polyelectrolytes are polymers that contain charged monomers. Because charged monomers were tethered on polymer chains and immobile, counterions are the main conducting species. Hence, the transference number of the counter ion is usually close to one [44]. However, due to the electrostatic attraction between counterions

and oppositely charged polymer chains, the mobility of counter ions is low. Besides, glass transition temperatures of dry polyelectrolytes with no plasticizer are high, and sometimes there is a formation of crystalline region, resulting in low polymer chain segmental motions. These factors all lead to low ionic conductivities in dry polyelectrolytes.

Solvated polyelectrolytes are polyelectrolytes containing small-molecule solvents. As such, the ion conductivities are greatly improved. Small-molecule solvents can act as a plasticizer and enhance the segmental motion of the polymer chain. Some polar solvents can also increase the dielectric constant and solvate counter ions, reducing the interaction between polymer and counter ion. Nafion, a perfluorosulfonic acid polymer developed for fuel cell applications, is a well-studied example of a solvated polyelectrolyte. When hydrated, it consists of two phases: water-filled channels and the hydrophobic polymer surrounding it [45]. Three proton transport mechanisms have been proposed and generally agreed on [46]. Close to the walls of water channels, protons could be transported via the surface water. However, its electrostatic interaction with SO_3^- groups on the water channel wall slows down this process considerably. The faster transport of protons happens through the bulk water in the middle area of the channel. In bulk water, besides the usual mass translational diffusion of hydronium, protons can also jump through a hydrogen bond network of water molecules by breaking and reforming hydrogen bonds. This mechanism called the Grotthuss transport, dominates when Nafion is hydrated.

The crosslinked pectin and its synthetic counterpart studied in this thesis are examples of solvated polyelectrolytes, characterized by the presence of hydrophilic functional groups and calcium ions that retain water. Similar to Nafion, the presence of water has a significant impact on the segmental motion and ion transport dynamics of the polymer, making it a complex system to study. This thesis delves into the various factors that contribute to ion transport in pectin and the HEA-AA polymer, offering a comprehensive analysis of the intricacies of this process. By exploring the interplay between the various factors, this research aims to shed light on the mechanism behind temperature sensitive polymer and how they can be optimized for future applications.

1.5 Chapters outline

This thesis explores the ion transport mechanism and the origin of thermal response in temperature-sensitive polyelectrolytes. The first part of the research (Chapters 3

and 4) focuses on crosslinked pectin as an example of thermally responsive polymer electrolytes. While crosslinked pectin has demonstrated potential as a temperature-sensing material, however, consistency remains an issue. As pectin is derived from plants, its chemical composition and properties can vary depending on the origin of the plant, the types of plant, and environmental conditions, making it challenging to fabricate consistent devices. Also, its flexibility degrades when dehydrated. To overcome these limitations, we developed a synthetic polymer HEAAA, mimicking the key structure and properties of pectin. The second part of the research (Chapters 5 and 6) focuses on the characterization and the ion transport mechanisms of HEAAA.

Chapter 2 gives a detailed description of sample fabrication methods and main experimental setups. Important characterization tools and corresponding analyzing methods, such as infrared spectroscopy, impedance spectroscopy, and density functional theory, are also explained.

Chapter 3 investigates the origin of temperature response in crosslinked pectin. We first show that the change in conductivity with temperature originates from the change in the ion mobility rather than the ion number density. Then, we present the positive correlation between the temperature response and the ion-pectin binding energy. Specifically, we identified that the binding of cations to the carboxyl and hydroxyl groups on pectin is the key to its high temperature sensitivity.

Chapter 4 studies the effect of humidity on ion transport in crosslinked pectin. By examining the relationship between ion conductivity and ion mobility, we show how ionic conductivity is affected by water content. Furthermore, we present the trade-off between the temperature sensitivity and ion conductivity in crosslinked pectin with varying water content.

Chapter 5 presents the development and characterization of the pectin-mimic ABA block copolymer based on 2-hydroxyethyl acrylate–acrylic acid (HEA-AA). We first show the optimization of the temperature response and flexibility of the synthetic polyelectrolyte by tailoring its molecular structure. Then, the temperature sensitivity and stability has been demonstrated. We also show that its ionic conductivity is barely affected by mechanical deformations. However, similar to pectin, its electrical property is also found to be sensitive to humidity.

Chapter 6 systematically investigates the effect of humidity and temperature on the ion transport of the synthetic polyelectrolyte HEA-AA. We discuss how water content modifies polymer-ion interaction and polymer segmental motions. This helps

explain why an increase in water content improves ion conductivity but negatively impacts temperature sensitivity. By examining dielectric spectra under various humidity and temperature conditions, we demonstrate that water and temperature affect ion transport and dielectric relaxation through similar mechanisms.

References

[1] Anil Kumar Chauhan, Purushottam Jha, Dinesh K Aswal, and Jatinder Yakhmi. Organic devices: fabrication, applications, and challenges. *Journal of Electronic Materials*, pages 1–39, 2022.

[2] Jane M. Shaw and Paul F. Seidler. Organic electronics: Introduction. *IBM Journal of Research and Development*, 45(1):3–9, 2001.

[3] Robert Abbel, Yulia Galagan, and Pim Groen. Roll-to-roll fabrication of solution processed electronics. *Advanced Engineering Materials*, 20(8):1701190, 2018.

[4] Muhammad Hilal and Jeong In Han. Development of a highly flexible and durable fiber-shaped temperature sensor based on graphene/ni double-decked layer for wearable devices. *IEEE Sensors Journal*, 20(10):5146–5154, 2020.

[5] Guanyu Liu, Qiulin Tan, Hairong Kou, Lei Zhang, Jinqi Wang, Wen Lv, Helei Dong, and Jijun Xiong. A flexible temperature sensor based on reduced graphene oxide for robot skin used in internet of things. *Sensors*, 18(5):1400, 2018.

[6] Jin Jeon, Han-Bo-Ram Lee, and Zhenan Bao. Flexible wireless temperature sensors based on ni microparticle-filled binary polymer composites. *Advanced materials*, 25(6):850–855, 2013.

[7] Burcu Arman Kuzubasoglu and Senem Kursun Bahadir. Flexible temperature sensors: A review. *Sensors and Actuators A: Physical*, 315:112282, 2020.

[8] Alastair Buckley. *Organic light-emitting diodes (OLEDs): Materials, devices and applications*. Elsevier, 2013.

[9] Hyuck Sik Wang, Jaehyun Cho, Dae Seok Song, Jong Hyun Jang, Jae Young Jho, and Jong Hyuk Park. High-performance electroactive polymer actuators based on ultrathick ionic polymer–metal composites with nanodispersed metal electrodes. *ACS Applied Materials & Interfaces*, 9(26):21998–22005, 2017.

[10] Karl Kruusamäe, Andres Punning, Alvo Aabloo, and Kinji Asaka. Self-sensing ionic polymer actuators: A review. In *Actuators*, volume 4, pages 17–38. MDPI, 2015.

[11] Petr Kuberskỳ, Jakub Altšmíd, Aleš Hamáček, Stanislav Nešprek, and Oldřich Zmeškal. An electrochemical no2 sensor based on ionic liquid: influence of the morphology of the polymer electrolyte on sensor sensitivity. *Sensors*, 15 (11):28421–28434, 2015.

[12] Xianbo Lu, Shouguo Wu, Li Wang, and Zhenxi Su. Solid-state amperometric hydrogen sensor based on polymer electrolyte membrane fuel cell. *Sensors and Actuators B: Chemical*, 107(2):812–817, 2005.

[13] Mirza Saquib Sarwar, Yuta Dobashi, Claire Preston, Justin KM Wyss, Shahriar Mirabbasi, and John David Wyndham Madden. Bend, stretch, and touch: Locating a finger on an actively deformed transparent sensor array. *Science Advances*, 3(3):e1602200, 2017.

[14] Hyosung An, Touseef Habib, Smit Shah, Huili Gao, Anish Patel, Ian Echols, Xiaofei Zhao, Miladin Radovic, Micah J Green, and Jodie L Lutkenhaus. Water sorption in mxene/polyelectrolyte multilayers for ultrafast humidity sensing. *ACS Applied Nano Materials*, 2(2):948–955, 2019.

[15] Hamid Farahani, Rahman Wagiran, and Mohd Nizar Hamidon. Humidity sensors principle, mechanism, and fabrication technologies: A comprehensive review. *Sensors*, 14(5):7881–7939, 2014.

[16] Raffaele Di Giacomo, Luca Bonanomi, Vincenzo Costanza, Bruno Maresca, and Chiara Daraio. Biomimetic temperature-sensing layer for artificial skins. *Science Robotics*, 2(3):eaai9251, 2017.

[17] Gang Ge, Yao Lu, Xinyu Qu, Wen Zhao, Yanfang Ren, Wenjun Wang, Qian Wang, Wei Huang, and Xiaochen Dong. Muscle-inspired self-healing hydrogels for strain and temperature sensor. *ACS Nano*, 14(1):218–228, 2019.

[18] Ran An, Xiaoyu Zhang, Linglin Han, Xiangdong Wang, Yulin Zhang, Lingying Shi, and Rong Ran. Healing, flexible, high thermal sensitive dual-network ionic conductive hydrogels for 3d linear temperature sensor. *Materials Science and Engineering: C*, 107:110310, 2020.

[19] Jianxun Dai, Hongran Zhao, Xiuzhu Lin, Sen Liu, Yunshi Liu, Xiupeng Liu, Teng Fei, and Tong Zhang. Ultrafast response polyelectrolyte humidity sensor for respiration monitoring. *ACS Applied Materials & Interfaces*, 11(6):6483–6490, 2019.

[20] Peter Hevesi, Sebastian Wille, Gerald Pirkl, Norbert Wehn, and Paul Lukowicz. Monitoring household activities and user location with a cheap, unobtrusive thermal sensor array. In *Proceedings of the 2014 ACM International Joint Conference on Pervasive and Ubiquitous Computing*, pages 141–145, 2014.

[21] Adam L. Isaac, Timothy D. Swartz, Mark L. Miller, Daniel J. Short, Eleanor A. Wilson, Jamie L. Chaffo, Eric S. Watson, Haihong Hu, Brian J. Petersen,

Jonathan D. Bloom, et al. Lower resource utilization for patients with healed diabetic foot ulcers during participation in a prevention program with foot temperature monitoring. *BMJ Open Diabetes Research and Care*, 8(1):e001440, 2020.

[22] William J. Fleming. Overview of automotive sensors. *IEEE Sensors Journal*, 1(4):296–308, 2001.

[23] John L. Riddle, George T. Furukawa, and Harmon H. Plumb. *Platinum Resistance Thermometry*, volume 126. National Bureau of Standards, 1973.

[24] Peter RN Childs, JR Greenwood, and CA Long. Review of temperature measurement. *Review of scientific instruments*, 71(8):2959–2978, 2000.

[25] Deepak Prasad and Vijay Nath. An overview of temperature sensors. In *Proceeding of the Second International Conference on Microelectronics, Computing & Communication Systems (MCCS 2017)*, pages 777–784. Springer, 2019.

[26] Suranga Seneviratne, Yining Hu, Tham Nguyen, Guohao Lan, Sara Khalifa, Kanchana Thilakarathna, Mahbub Hassan, and Aruna Seneviratne. A survey of wearable devices and challenges. *IEEE Communications Surveys & Tutorials*, 19(4):2573–2620, 2017.

[27] RK Bhan, Raghvendra Sahai Saxena, CR Jalwania, and SK Lomash. Uncooled infrared microbolometer arrays and their characterisation techniques. *Defence Science Journal*, 59(6):580–589, 2009.

[28] M Abdel-Rahman, N Al-Khalli, MF Zia, M Alduraibi, B Ilahi, E Awad, and N Debbar. Fabrication and design of vanadium oxide microbolometer. In *AIP Conference Proceedings*, volume 1809, page 020001. AIP Publishing LLC, 2017.

[29] Yao Jin, Hitesh A Basantani, Adem Ozcelik, Tom N. Jackson, and Mark W. Horn. High-resistivity and high-tcr vanadium oxide thin films for infrared imaging prepared by bias target ion-beam deposition. In *Infrared Technology and Applications XXXIX*, volume 8704, pages 959–964. SPIE, 2013.

[30] Jingwen Li, Zhenhua Li, and Xuekang Chen. Infrared and thz thermal detection based on an all polymer device. *Sensors and Actuators A: Physical*, 309: 112021, 2020.

[31] Anna Håkansson, Maryam Shahi, Joseph W Brill, Simone Fabiano, and Xavier Crispin. Conducting-polymer bolometers for low-cost ir-detection systems. *Advanced Electronic Materials*, 5(6):1800975, 2019.

[32] Tomoyuki Yokota, Yusuke Inoue, Yuki Terakawa, Jonathan Reeder, Martin Kaltenbrunner, Taylor Ware, Kejia Yang, Kunihiko Mabuchi, Tomohiro Murakawa, Masaki Sekino, et al. Ultraflexible, large-area, physiological temperature sensors for multipoint measurements. *Proceedings of the National Academy of Sciences*, 112(47):14533–14538, 2015.

[33] Jingwen Li, Zhenhua Li, Jicheng Wang, and Xuekang Chen. Study of conductive polymer pedot: Pss for infrared thermal detection. *Optical Materials Express*, 9(11):4474–4482, 2019.

[34] Jonghwa Park, Marie Kim, Youngoh Lee, Heon Sang Lee, and Hyunhyub Ko. Fingertip skin–inspired microstructured ferroelectric skins discriminate static/dynamic pressure and temperature stimuli. *Science Advances*, 1(9): e1500661, 2015.

[35] Meital Segev-Bar, Avigail Landman, Maayan Nir-Shapira, Gregory Shuster, and Hossam Haick. Tunable touch sensor and combined sensing platform: toward nanoparticle-based electronic skin. *ACS Applied Materials & Interfaces*, 5(12):5531–5541, 2013.

[36] Tran Quang Trung, Subramaniyan Ramasundaram, Byeong-Ung Hwang, and Nae-Eung Lee. An all-elastomeric transparent and stretchable temperature sensor for body-attachable wearable electronics. *Advanced Materials*, 28(3): 502–509, 2016.

[37] Jaemin Kim, Mincheol Lee, Hyung Joon Shim, Roozbeh Ghaffari, Hye Rim Cho, Donghee Son, Yei Hwan Jung, Min Soh, Changsoon Choi, Sungmook Jung, et al. Stretchable silicon nanoribbon electronics for skin prosthesis. *Nature Communications*, 5(1):5747, 2014.

[38] R. Chad Webb, Andrew P Bonifas, Alex Behnaz, Yihui Zhang, Ki Jun Yu, Huanyu Cheng, Mingxing Shi, Zuguang Bian, Zhuangjian Liu, Yun-Soung Kim, et al. Ultrathin conformal devices for precise and continuous thermal characterization of human skin. *Nature Materials*, 12(10):938–944, 2013.

[39] Daniel T Hallinan Jr and Nitash P Balsara. Polymer electrolytes. *Annual Review of Materials Research*, 43:503–525, 2013.

[40] Vera Bocharova and Alexei P. Sokolov. Perspectives for polymer electrolytes: A view from fundamentals of ionic conductivity. *Macromolecules*, 53(11): 4141–4157, 2020.

[41] H Kahnt. Ionic transport in oxide glasses and frequency dependence of conductivity. *Berichte der Bunsengesellschaft für physikalische Chemie*, 95(9): 1021–1025, 1991.

[42] Kyle M. Diederichsen, Hilda G. Buss, and Bryan D. McCloskey. The compensation effect in the vogel–tammann–fulcher (vtf) equation for polymer-based electrolytes. *Macromolecules*, 50(10):3831–3840, 2017.

[43] Oleg Borodin and Grant D. Smith. Mechanism of ion transport in amorphous poly (ethylene oxide)/litfsi from molecular dynamics simulations. *Macromolecules*, 39(4):1620–1629, 2006.

[44] Chang Yun Son and Zhen-Gang Wang. Ion transport in small-molecule and polymer electrolytes. *The Journal of Chemical Physics*, 153(10):100903, 2020.

[45] EJ Roche, M Pineri, R Duplessix, and AM Levelut. Small-angle scattering studies of nafion membranes. *Journal of Polymer Science: Polymer Physics Edition*, 19(1):1–11, 1981.

[46] Pyoungho Choi, Nikhil H. Jalani, and Ravindra Datta. Thermodynamics and proton transport in nafion: II. Proton diffusion mechanisms and conductivity. *Journal of the Electrochemical Society*, 152(3):E123, 2005.

C h a p t e r   2

METHODS

This chapter focuses on the sample fabrication and characterization methods used in this thesis. To produce consistent, uniform polymer film, various experimental conditions have been tested and optimized, such as the drying conditions, degassing methods, and crosslinking methods. Here, we present the optimized fabrication protocols for both pectin and HEAAA. Furthermore, the characterization methods and corresponding analysis techniques that are recurrently utilized throughout this thesis are explained in this chapter, including temperature response measurements, infrared spectroscopy, impedance spectroscopy, and density functional theory. These experimental and computational tools provided vital information for understanding thermal sensing mechanisms.

Some content of this chapter has been adapted from:

- Linghui Wang, Tae Hyun Kim, Vincenzo Costanza, Nick Higdon, and Chiara Daraio. Ion transport in thermal responsive pectin film. *Submitted*, 2023

- Linghui Wang, Vincenzo Costanza, and Chiara Daraio. Effect of water content on the ion transport in pectin films. *Under preparation*, 2023.

- Linghui Wang, Vincenzo Costanza, Nick Higdon, Tae Hyun Kim and Chiara Daraio. Ion transport phenomena in thermally responsive polyelectrolytes. *Under preparation*, 2023.

2.1   Polymer film fabrication

Crosslinked pectin

Citrus pectin with 34% methylation and 84% galacturonic acid (Herbstreith & Fox) was used. The average molecular weight measured by a viscosimeter is 59000 Dalton. First, the pectin powder (1% w/v) was dissolved in deionized (DI) water at 80°C with stirring for more than an hour. To remove bubbles, the pectin solution was degassed in a vacuum pump. 30 mM crosslinking salt solution was prepared by dissolving the corresponding salt powder (Sigma Aldrich) into DI water.

To make a free-standing pectin film, we first poured the pectin solution into a mold and then added crosslinking salt solutions. After 24 hours of gelation, when the

pectin was fully cross-linked, we dehydrate the gel at room temperature for another 24 hours. We made sure that the gelation time is sufficient, verifying that its infrared spectrum does not change for longer crosslinking time.
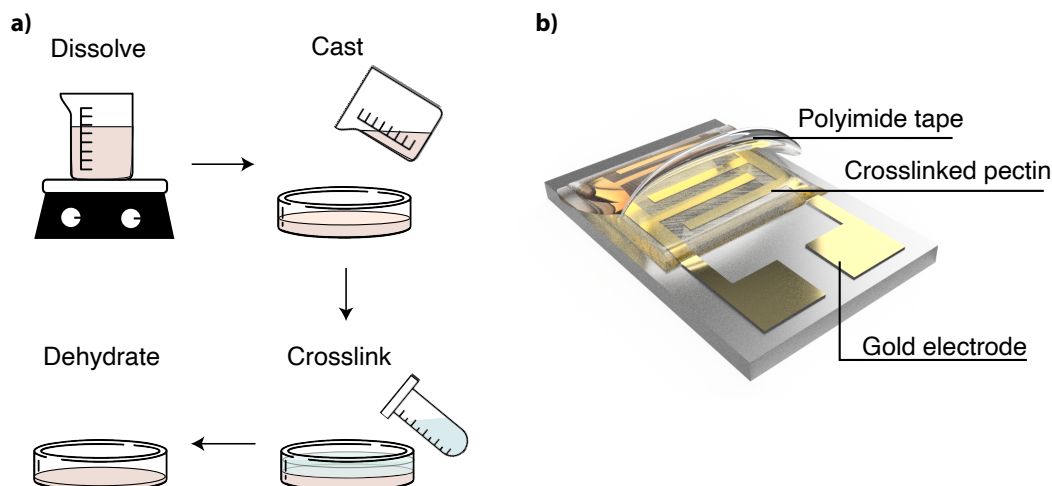
Figure 2.1: Pectin film fabrication (a) Self-standing pectin film fabrication process. (Some icons in the diagram are from thenounproject.com). (b) Pectin deposited on electrodes for electrical measurements.

For electrical measurements, we deposit 20 μl of 1% pectin directly onto the electrodes to ensure good electrical contact between pectin samples and electrodes. The detailed steps are described as follows: to improve the consistency in sample sizes and thicknesses, we made stencils by cutting out a square hole in a Poly(methyl methacrylate) substrate with a Silhouette Cameo cutter. We attached the stencil to the electrode surface and then dropped the pectin solution in the opening of the stencil. We then let it dry overnight at room temperature. Afterward, 20 μl 30 mM crosslinking solution was added. After crosslinking for 24 hours, samples were rinsed in the DI water to get rid of the extra free chloride ions. This process was performed to prevent electrode corrosion due to high chloride ion concentration during the electrical measurement. After rinsing with water and removing the stencil, samples were then dried and sealed using polyimide tape.

Biomimetic thermally-sensitive polymer: HEAAA

The HEAA polymer were employing reversible addition-fragmentation chain transfer (RAFT) polymerization as shown in figure 2.2. Nitrogen-purged tert-butyl acrylate 2 (1.28 g, 10 mM) and 2-hydroxyethyl acrylate 1 (1.16 g, 10 mM) is dissolved in 2 mL DMF, followed by S,S-Dibenzyl trithiocarbonate 3 (29 mg, 0.1 mM).

The mixture is further purged under nitrogen for 3 minutes, added with AIBN (0.8 mg, 5 µM), and then stirred at 75 °C under the protection of N_2, and the progress in polymerization was monitored using H-NMR. The reaction was cooled down and vented to air at approximately 80% conversion rate. Residual tert-butyl acrylate and 2-hydroxyethyl acrylate was removed first by vacuum, followed by precipitation in 100 mL cold Diethyl Ether to yield a yellow oil as the macro-CTA (2.02 g, 80%). For deprotection, the polymer (1 g) was dissolved in 3 mL dichloromethane (DCM), followed by the addition of 3 mL trifluoroacetic acid (TFA). The reaction was stirred at room temperature overnight. DCM and TFA were removed by vacuum, followed by precipitation in cold diethyl ether, to result in a highly sticky yellow oil as HEAAA (100%). We then mixed the deprotected HEAAA with a calcium chloride solution in ethanol 1:2 (300 mM) to obtain the final solution. For electrical measurements,
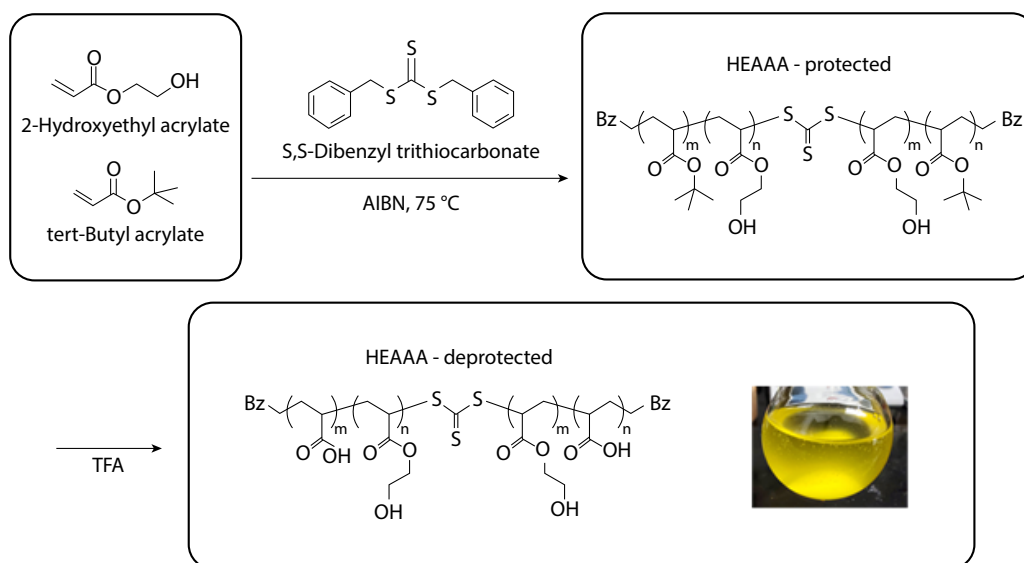
Figure 2.2: HEAAA synthesis.

5 μL of HEAAA -CaCl2(1g/mL) were drop casted on the gold electrodes and dried under vacuum for half an hour. The so prepared samples were kept overnight in a glove box flushed with nitrogen to eliminate ethanol/water excess from the polymer matrix.

2.2 Setups for temperature response measurements

Two setups have been built to characterize the temperature responses of polymers. For studies presented in Chapters 3, 4, and 5, the first setup was used. For the study in Chapter 6, the second setup was used. In both setups, temperature cycling was

actuated by a Peltier-Element (model Qc-31). The temperature was independently measured with a Pt100 platinum resistance thermometer placed near samples. The Pt100 sensors were previously calibrated with a FLIR thermal camera (A655SC). A PID controller was implemented to generate a sinusoidal temperature wave.

In the first setup, measurements were performed inside a customized sealed nitrogen box with hermetically sealed electrical connections. A humidity sensor (SHT4x Sensirion) inside the box reads the relative humidity (RH) level. The RH inside could be adjusted manually by flushing the box with nitrogen gas. The lowest RH that could be reached inside the box is at around 10%. To ensure good electrical contact between samples and substrates, they are sandwiched between two acrylic plates as shown in figure 2.3 (a). Electrical measurements were done with two probes in contact with the substrates.

In the second setup, a custom humidity-controlled box was built to control humidity between 0% and 60% (Fig. 2.3(b)). Airflow passing through desiccant beads was mixed with airflow coming from a water tank. By adjusting the air speed and the mix between the two flows the correct humidity can be achieved in the chamber. The humidity was then measured by a humidity sensor (Sensoria SHT16) placed in close proximity to the sample and used to keep the humidity constant in the chamber. A breakout board was placed into the humidity box in order to send signals from the substrate to the impedance analyzer. The substrates and the reference Pt100 were electrically connected through an interface board that could be connected with the impedance analyzer and the temperature control board. The current was measured with the impedance analyzer with an average sampling rate of 10 S/s.

2.3 Impedance spectroscopy

Impedance spectroscopy (IS) is a powerful technique to investigate electrical phenomena in materials. It probes the system at a frequency range between 10^{-3} Hz and 10^9 Hz. It has been widely applied to study charge transfer at an interface, charge diffusion, dielectric relaxation, surface corrosion, and so on. Specifically, for ion conducting polymers, IS is especially helpful for studying the double-layer formation, ion diffusion, polymer chain segmental motion, and sub-segmental relaxations. However, to obtain accurate and undistorted data, good electrical contact between samples and electrodes is required [3].

During an IS experiment, AC voltage $V^*(\omega)$ is applied to a sample at a range of frequencies ω and the current response $I^*(\omega)$ is recorded. The impedance $Z^*(\omega)$ is
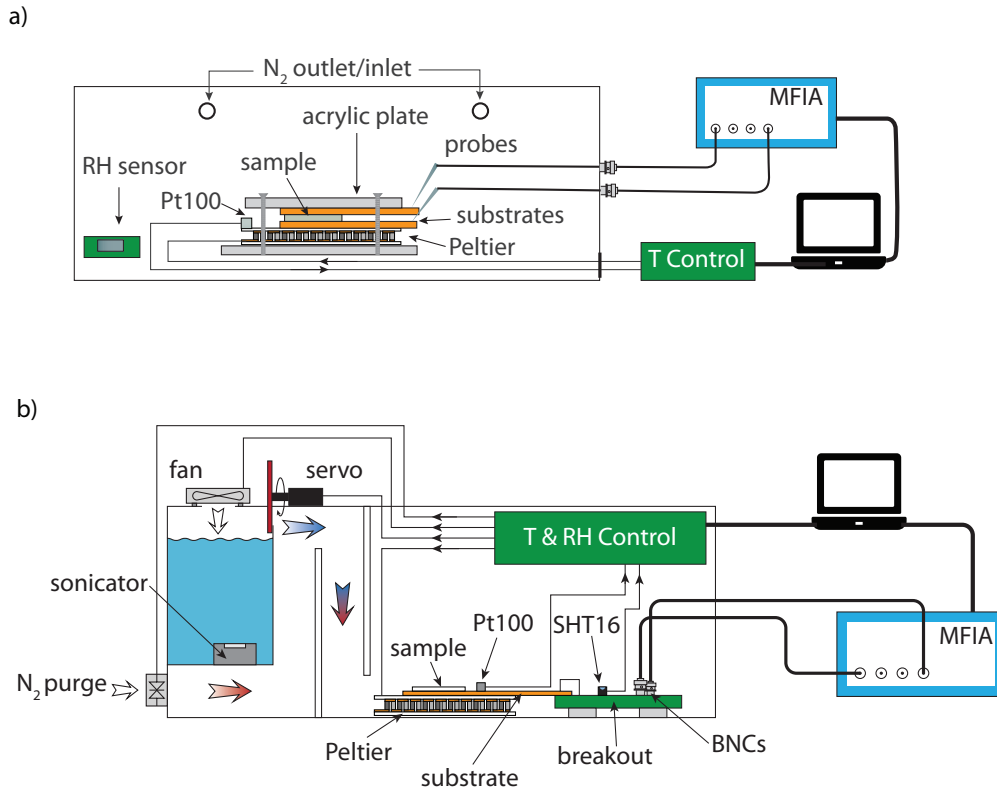
Figure 2.3: Measurement setup (a) Nitrogen box. (b) Humidity controlled box.

calculated as

$$Z^* = \frac{V^*(\omega)}{I^*(\omega)} = R(\omega) + iX(\omega) \tag{2.1}$$

where R, the real part of the complex impedance, is the resistance, and X, the imaginary part, is the reactance.

Impedance data can be analyzed in different representations: dielectric ϵ^*, conductivity σ^* and modulus representation M^*. Although those representations contain the same information, some processes are more visible in one representation than the other. For example, dielectric relaxations, such as segmental relaxation, result in peaks in the dielectric representation, where the shape of peaks provides information on the relaxation time distribution. The relationship between these representations is described as follows:

$$\epsilon^*(\omega) = \frac{\sigma^*(\omega)}{i\omega\epsilon_0} = \epsilon'(\omega) - i\epsilon''(\omega) \tag{2.2}$$

$$M^*(\omega) = \frac{1}{\epsilon^*(\omega)} = M'(\omega) - iM''(\omega). \tag{2.3}$$

One commonly used method to interpret an impedance spectrum is equivalent circuit analysis. In this method, a circuit, including resistors, capacitors, constant-phase elements, and other circuit elements, is constructed and the impedance of the circuit is fitted to the impedance of the material [4]. Each element in the circuit represents a physical process. For example, a resistor corresponds to charge transfer or ion migration, and a capacitor is associated with space-charge formation at the electrode-electrolyte interface. However, this analysis is flawed due to several reasons. First, for complex impedance behavior, usually more than one equivalent circuit can be constructed to mimic the response of a material. The choice of one circuit over the other can be arbitrary. Second, without proper modeling of the underlying physical processes, there is ambiguity in the interpretation of an equivalent circuit [4]. Due to these ambiguities, the equivalent circuit method was not used in this thesis. Instead, we analyze the impedance spectrum using physical models to describe underlying processes.

Three processes are commonly observed in dielectric spectrums: 1) dipolar fluctuations, 2) transport of mobile charge carriers, and 3) electrode polarization [5]. The electrode polarization effect dominates in the relatively low-frequency region. It originates from the double-layer formation at the blocking electrode. Simple models have been developed, and in the dilute solution limit, ion transport parameters such as mobilities and charge carrier number densities could be extracted. However, in practice, electrode polarization is sensitive to electrode roughness and porosity and deviates from the model [5]. Therefore, in this thesis, we focus on the higher frequency behavior in the impedance spectrum where the transport of the mobile charge carriers and dipolar fluctuation dominate.

Dipolar relaxations

Dipolar relaxation is a relaxation process resulting from the rotational fluctuation of permanent dipoles. This dipole could be a polar side group or polar monomer on the chain [5]. Depending on the length scale of molecular motion, dipolar relaxations in polymers can be divided into the following three categories: a) chain relaxations, b) segmental relaxations (α relaxation), and c) secondary relaxations. Chain relaxations, originating from the normal modes of polymer chains, are observable via IS only when there is a nonzero dipole along the chain [3]. Unlike chain relaxation, the origin of segmental motions in polymer remains elusive. Some ascribe segmental motions to a damped diffusion process of conformational states along the polymer chain [6]. In general, it is attributed to the micro-Brownian motion of local chain

segments and is related to the viscosity, diffusion, and rotation of monomers. In addition, segmental dynamics disappear in the glassy state and are considered to be responsible for the glass transition. Secondary relaxations of polymers refer to molecular motions happening at a sub-segmental length scale, such as side chain motion. Compared to segmental dynamics, secondary relaxations usually have lower activation energy and remain active in the glassy state.

Debye relaxation is the simplest model describing dipolar relaxations [5]. In this model, a dipolar molecule is modeled as a sphere in a viscous fluid under the influence of thermal fluctuations. The polarization response after a step electric field was found to have the following time dependence:

$$\frac{dP(t)}{dt} = -\frac{1}{\tau_D}P(t) \tag{2.4}$$

where τ_D is a characteristic time for the relaxation. Therefore, the polarization follows an exponential relation:

$$P(t) = P_0 e^{-t/\tau_D}. \tag{2.5}$$

The complex permittivity of dielectric material is given by:

$$\frac{\epsilon^*(\omega) - \epsilon_\infty}{\epsilon_s - \epsilon_\infty} = -\int_0^\infty \frac{d\Phi(t)}{dt} e^{-i\omega t} dt \tag{2.6}$$

where ϵ_∞ and ϵ_s are the high-frequency limit and low-frequency limit permittivity, and $\Phi(t)$ is the normalized correlation function of the polarization given by

$$\Phi(t) = \frac{\langle \Delta P(0)\Delta P(t)\rangle}{\langle \Delta P(0)^2\rangle}. \tag{2.7}$$

Pluging in relation 2.5 to equation 2.6, we then obtain the complex permittivity as a function of frequency Debye relaxation relation:

$$\epsilon^*(\omega) = \frac{\Delta\epsilon}{1 + i\omega\tau_D} + \epsilon_\infty, \quad \Delta\epsilon = \epsilon_s - \epsilon_\infty \tag{2.8}$$

where ϵ_s and ϵ_∞ are the dielectric values at the static and high-frequency limit respectively. ϵ_∞ takes into account the atomic and electronic polarization, of which the response to the external electric field can be considered to be instantaneous relative to the dipolar relaxations. Although the Debye relaxation model qualitatively captures the frequency dependence of a dipolar relaxation, experimental results show deviation from its prediction [5]. The measured $\epsilon''(\omega)$ usually shows a broader and asymmetric peak. This departure, called non-Debye relaxation, could be a result of
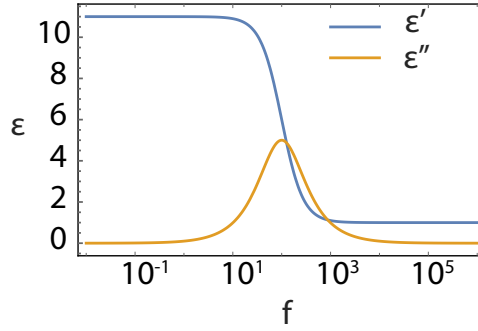
Figure 2.4: Debye relaxation. Frequency dependence of the real and imaginary part of the dielectric function from Debye relaxation.

dipole-dipole interactions, which are not accounted for in the model. In addition, rather than a single relaxation time, there could be a distribution of relaxation time in a material. To describe the non-Debye behavior, an empirical model was developed by Havriliak and Negami [5]:

$$\epsilon^*(\omega) = \frac{\Delta\epsilon}{(1 + (i\omega\tau_D)^\beta)^\gamma} + \epsilon_\infty, \quad \beta > 0, \quad \beta\gamma \leq 1 \tag{2.9}$$

where β and γ are shape parameters accounting for the symmetric and asymmetric broadening.

Fluctuation of mobile ions

For electronic conduction in conductors, its conductivity $\sigma^*(\omega) = \sigma_0$ is independent of frequency at the frequency range 10^{-2} Hz to 10^8 Hz. Therefore, according to equation 2.2, electron transport only contributes to the imaginary part of the dielectric function: $\epsilon''(\omega) = \frac{\sigma_0}{\epsilon_0\omega}$. For ion conduction in an amorphous polymer electrolyte, the dielectric response is not constant with respect to frequency. In most disordered materials including polymer electrolytes, the real part of ion conductivity has empirically been found to have a power law dependence on frequency ν, which has been referred to as the Jonscher's power law [7]:

$$\sigma'(\nu) = \sigma_{dc}(1 + (\frac{\nu}{\nu^*})^n), \quad 0 < n < 1 \tag{2.10}$$

where σ_{dc} is the DC ion conductivity, and ν^* is the AC onset frequency, marking the transition from DC to AC conduction. ν^* can be obtained via identifying the frequency where the real conductivity is $2\sigma_{dc}$. This power law dependence has also been proposed by Almond and West to describe charge transport in defective crystals and therefore is also called the Almond-West formula. It was suggested that this power law dependence originates from a sub-diffusive ionic relaxation process,

where ions hop back and forth in the oppositely charged solvation sites, and the v^* is interpreted as the hopping rate. However, this explanation lacks rigorous theoretical derivation [7].

To model the AC response in a random medium, including amorphous semiconductors, glasses, and polymers, Dyre developed the random free energy barrier model [8]. In this model, ions are hopping among an array of sites where the hopping distance is assumed to be constant. The hopping activation energy or hopping barrier varies randomly and has a wide distribution. Then the hopping process can be described by the following stochastic master equation:

$$\frac{\partial P(s,t)}{\partial t} = -\gamma_s P(s,t) + \sum_{s'} \Gamma(s' \to s) P(s',t), \quad \gamma_s = \sum_{s'} \Gamma(s \to s') \quad (2.11)$$

where $P(s,t)$ is the probability of finding the ion at site s, $\Gamma(s \to s')$ is the hopping probability from the site s to site s' and for a thermally activated hopping, it can be written as:

$$\Gamma = \Gamma_0 \exp\left(-\frac{\Delta F}{k_B T}\right) \quad (2.12)$$

where ΔF is the hopping free energy barrier and Γ_0 is the attempt frequency. For simplicity, it is assumed to follow a uniform distribution with cutoff frequencies γ_{max} and γ_{min}. Thus, the probability distribution of the hopping frequency is proportional to Γ^{-1}. To relate the probability with conductivity, we first rewrite the equation 2.11 using Bra-ket notation:

$$\frac{\partial}{\partial t}|\psi\rangle = H|\psi\rangle \quad (2.13)$$

$$H = -\sum \gamma_s |s\rangle\langle s| + \sum_{s,s'} \Gamma(s' \to s)|s\rangle\langle s'|. \quad (2.14)$$

Therefore, we have:

$$\sigma(\omega) = -\frac{nq^2\omega^2}{6k_B T} \int_0^\infty \langle\Delta R^2(t)\rangle e^{-i\omega t} dt = -\frac{nq^2\omega^2}{6Nk_B T} \sum_{s,s'} (s-s')^2 \langle s|G(i\omega)|s'\rangle \quad (2.15)$$

where G is Green's function operator for H and $G = 1/(i\omega - H)$. After applying the Continuous-time random walk (CTRW) approximation and some mathematical manipulation, the complex conductivity can be derived:

$$\sigma(\omega) = \frac{1}{6}(-i\omega + \frac{i\omega ln(\gamma_{max}/\gamma_{min})}{ln[(1+i\omega/\gamma_{min})(1+i\omega/\gamma_{max})]}). \quad (2.16)$$

If we assume $\gamma_{max} \to \infty$, that is the $\Delta F_{min} \to 0$, we could write:

$$\sigma(\omega) = \sigma_{dc} \frac{i\omega\tau}{ln(1+i\omega\tau)}, \tau = \gamma_{min}^{-1}. \quad (2.17)$$

Here, $1/\tau$ signals the transition from DC to AC conduction, and it corresponds to the hopping frequency over the largest barrier in the ion hopping percolation.

2.4 Infrared spectroscopy

Infrared (IR) spectroscopy measures the absorption of material at a wavelength between 0.8 and 1000 μm [9]. Absorption bands in this region usually correspond to modes of vibration or rotation of molecules. Therefore, it can be used to identify the existence of certain functional groups or chemical bonds in an unknown material [10]. Also, the frequency and strength of vibration are influenced by both intramolecular and intermolecular interactions. It can probe changes in the solvation and coordination of functional groups. In addition, since the absorbance is proportional to the concentration of the attenuating species according to Beer-lambert law, IR spectroscopy is also an effective and non-destructive tool to estimate quantities of components in a material. Infrared spectra could be measured in either the transmission mode or the reflection mode, which is called attenuated total reflectance (ATR). In the ATR mode, samples would be pressured to form good contact with a crystal (e.g. zinc selenide or diamond) that has a high refractive index [9]. The infrared light travels through the crystal and forms a total internal reflection at the interface between the crystal and the sample. Part of the light energy is absorbed by the material via the evanescent wave. The amplitude of the attenuated reflected light is then measured. ATR-IR measurements are popular because it requires little sample preparation and is independent of sample thickness. Unlike the transmission mode, ATR also works well for strongly absorbing material. For our study
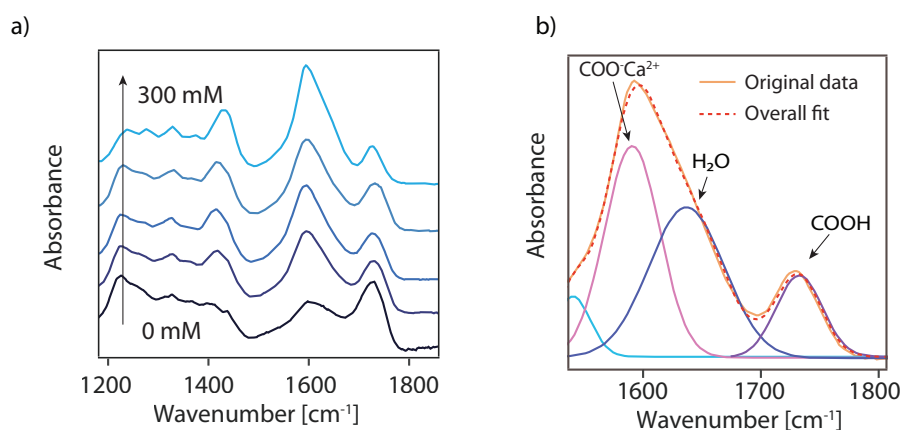
Figure 2.5: IR spectrum of crosslinked pectin. (a) Infrared spectrum of pectin crosslinked with different concentrations of $CaCl_2$. (b) Fitting of IR spectra with Gaussian peaks.

on temperature sensitive polymers, IR spectroscopy provides critical information

on the metal-polymer binding, which is the key to temperature sensitivity. Pectin and HEAAA have a few distinctive IR absorption peaks between 1500 cm^{-1} and 1800 cm^{-1}, corresponding to the asymmetrical vibration of carboxyl groups, the asymmetrical vibration of metal-ion-bound carboxylate groups and the scissoring bend of the water molecules [11]. The peak area ratio between carboxyl groups and metal-ion-bound carboxylate groups is indicative of the percentage of metal ion that coordinates with the polymer. Shifts in peak frequencies suggest changes in the binding mode [12]. Because of the non-destructive nature of IR spectroscopy, we could monitor how the binding interaction changes with increasing temperature, RH, and voltage. Infrared spectra of pectin were acquired using the diamond at-
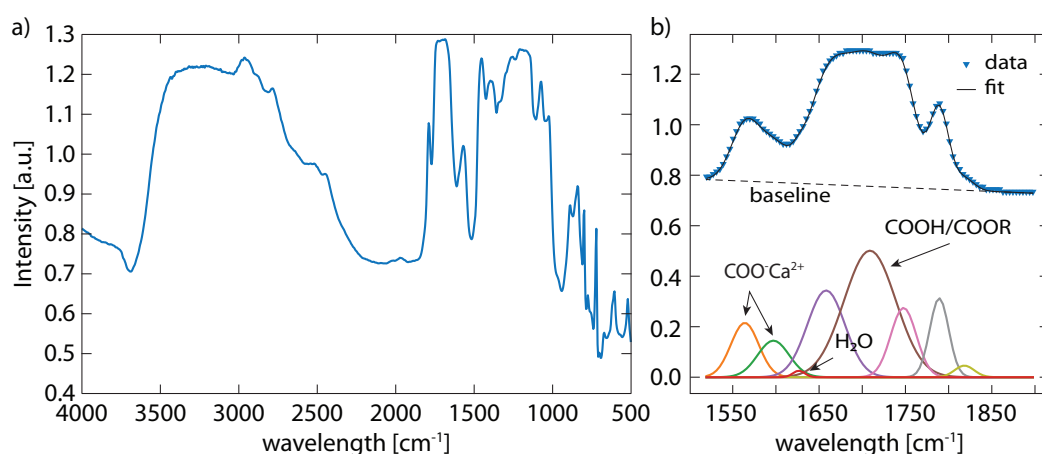
Figure 2.6: IR spectrum of CaCl$_2$-HEAAA (a) A typical infrared spectra of CaCl$_2$-HEAAA (b) Fitting of IR spectra with Gaussian peaks. Peaks at 1563 cm^{-1} and 1597 cm^{-1} correspond to the vibration of calcium bound carboxylic acid. The peak at 1620-1630 cm^{-1} correspond to vibration of water.

tenuated total reflectance (ATR) module of Nicolet 6700 FT-IR spectrometer. ATR is used because the crosslinked pectin film has a relatively low transmission in the infrared region, rendering the transmission mode noisy and indecipherable. Before each sample spectrum collection, a background spectrum is collected. For each spectrum collection, at least 64 scans were performed and averaged. For the FTIR measurements at different temperatures and voltage, a customized *in-situ* heating device was fabricated using a small Peltier heater and a temperature controller. Voltage was applied through copper tape electrodes attached to the pectin film. To process absorbance spectra, a quadratic baseline was used and Gaussian peaks were fitted.

2.5 Density functional theory (DFT)

DFT is a quantum mechanical method based on the Hohenberg–Kohn theorem to calculate the electronic structure of molecules and solids. Formally, it is an exact theory with the total energy expressed as a functional of the electron density. However, in practice, the exchange-correlation functional is usually unknown and chosen heuristically [13]. Nevertheless, DFT is accurate enough to solve many problems in chemistry, condensed matter physics, and material science [14, 15]. In chemistry, it is widely used to calculate the ground-state structure of molecules, reaction energies, binding energies, and spectroscopic properties. In this thesis, DFT has been applied to calculate the binding energy between metal ions and polymers. One major source of error in the DFT calculation is the self-interaction error (SIE)[15, 16]. This error arises from the imperfect cancellation between self-Coulomb interaction and exchange-correlation energy for approximated density functionals. Hybrid functionals, containing a small fraction of Fock exchange, are generally recommended to mitigate the error[15]. While it may not entirely eradicate this error, it proves satisfactory for our research purposes when employing DFT to compare the relative binding energies of various ions to polymers. In this thesis, DFT studies were conducted through ORCA (version 4.2.0) with the hybrid B3LYP functional. A def2-TZVP basis set with a def2/J auxiliary basis set was applied. The usual RIJCOSX approximation for Coulomb and HF exchange was made. The structures were first optimized and then frequency calculations were carried out. From these structures, single point energy calculations were carried out utilizing ORCA's atom-pairwise dispersion correction and/or ORCA's conductor-like polarizable continuum model for a water solvent. The introduction of dispersion was found to only slightly affect the calculated binding energy. Simulated infrared spectra were obtained from the frequency calculation by assuming a Gaussian-shape peak for each vibration frequency, with a full-width-half-maximum of 30 cm^{-1}.

References

[1] Linghui Wang, Tae Hyun Kim, Vincenzo Costanza, Nick Higdon, and Chiara Daraio. Ion transport in thermal responsive pectin film. *in submission*, 2023.

[2] Linghui Wang, Vincenzo Costanza, Nick Higdon, and Chiara Daraio. Ion transport phenomena in thermally responsive polyelectrolytes. *in submission*, 2023.

[3] Ivan Popov, Shiwang Cheng, and Alexei P Sokolov. Broadband dielectric spectroscopy and its application in polymeric materials. *Macromolecular Engi-*

neering: From Precise Synthesis to Macroscopic Materials and Applications, pages 1–39, 2022.

[4] J. Ross Macdonald and Evgenij Barsoukov. *Impedance spectroscopy: theory, experiment, and applications*. John Wiley & Sons, 2018.

[5] Friedrich Kremer and Andreas Schönhals. *Broadband dielectric spectroscopy*. Springer Science & Business Media, 2002.

[6] Bernard Valeur, Jean-Pierre Jarry, François Geny, and Lucien Monnerie. Dynamics of macromolecular chains. I. Theory of motions on a tetrahedral lattice. *Journal of Polymer Science: Polymer Physics Edition*, 13(4):667–674, 1975.

[7] Jeppe C. Dyre, Philipp Maass, Bernhard Roling, and David L Sidebottom. Fundamental questions relating to ion conduction in disordered solids. *Reports on Progress in Physics*, 72(4):046501, 2009.

[8] Jeppe C. Dyre. The random free-energy barrier model for ac conduction in disordered solids. *Journal of Applied Physics*, 64(5):2456–2468, 1988.

[9] C-P. Sherman Hsu et al. Infrared spectroscopy. *Handbook of instrumental techniques for analytical chemistry*, 249, 1997.

[10] Lily M. Ng and Reiko Simmons. Infrared spectroscopy. *Analytical Chemistry*, 71(12):343–350, 1999.

[11] Ali Assifaoui, Camille Loupiac, Odile Chambin, and Philippe Cayot. Structure of calcium and zinc pectinate films investigated by ftir spectroscopy. *Carbohydrate Research*, 345(7):929–933, 2010.

[12] Masayuki Nara, Hajime Torii, and Mitsuo Tasumi. Correlation between the vibrational frequencies of the carboxylate group and the types of its coordination to a metal ion: An ab initio molecular orbital study. *The Journal of Physical Chemistry*, 100(51):19812–19817, 1996.

[13] Richard A. Friesner. Ab initio quantum chemistry: Methodology and applications. *Proceedings of the National Academy of Sciences*, 102(19):6648–6653, 2005.

[14] V. P. Gupta. *Principles and Applications of Quantum Chemistry*. Academic Press, 2015.

[15] Markus Bursch, Jan-Michael Mewes, Andreas Hansen, and Stefan Grimme. Best-practice dft protocols for basic molecular computational chemistry. *Angewandte Chemie International Edition*, 61(42):e202205735, 2022.

[16] Junwei Lucas Bao, Laura Gagliardi, and Donald G Truhlar. Self-interaction error in density functional theory: An appraisal. *The Journal of Physical Chemistry Letters*, 9(9):2353–2358, 2018.

Chapter 3

ION TRANSPORT IN THERMAL RESPONSIVE PECTIN FILM

The work presented in this chapter has been adapted from:

- Linghui Wang, Tae Hyun Kim, Vincenzo Costanza, Nick Higdon, and Chiara Daraio. Ion transport in thermal responsive pectin film. *Submitted to Applied Physics Letters*, 2023

3.1 Abstract

The ionic conductivity of $CaCl_2$-crosslinked pectin was found to exhibit a record-high temperature response, suggesting its potential applications in wearable devices and infrared sensors. However, little was known about its ion conduction mechanisms and the origin of its high-temperature sensitivity. In this study, we perform controlled experiments and identify calcium ions as the dominant current carriers. By analyzing infrared spectra at different temperatures, we find that the temperature response is due to changes in ion mobility, rather than variations in ion number density. We compare measurements and modeling results of 9 different multivalent ions and find a positive correlation between their temperature responses and their binding energy to pectin. While these findings are fundamental in nature, they provide relevant guidance for the future design of temperature-sensitive polymers and other materials for organic electronics.

3.2 Introduction

Thermal sensing technologies have been developed for a wide range of applications including wearable devices, robotics, infrared sensing, and internet of things [1–3]. Recent reports discovered a new type of thermal sensing material [4]: $CaCl_2$-crosslinked pectin. Its electrical conductivity is highly sensitive to temperature changes, over a wide range of temperatures. Compared to the state-of-art temperature sensing materials, like vanadium oxide, pectin has been found to be at least an order of magnitude higher in its response [4]. Furthermore, pectin is transparent, solution-processable, biodegradable, inexpensive, and lightweight, making it a great candidate for large-scale temperature mapping applications, such as electronic skins.
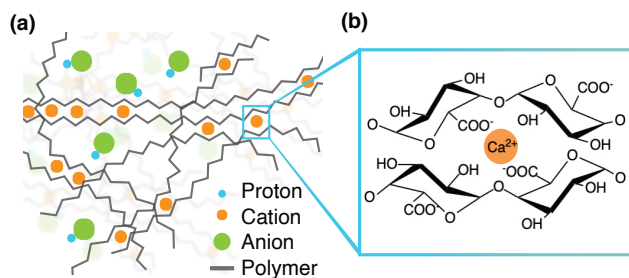
Figure 3.1: Schematic diagram of divalent-cation crosslinked pectin. (a)The divalent cations (orange) can deprotonate polygalacturonic acid and crosslink multiple polymer chains to form a connected network. The proton (light blue) disassociated from the galacturonic acid can form ion pairs with the anion (green) from the crosslinking salt, when the water content in the network is low. (b) Coordination between calcium ion and galacturonates.

Pectin is a structural polysaccharide that can be extracted from plant cells. It has been frequently used in the food and pharmaceutical industry as a gelling agent. It is polydisperse and has a complex structure [5]. The pectin backbone is mainly composed of homogalacturonan, rhamnogalacturonan I (RG I), and II (RG II). RG I and RG II with complicated side chains, making it difficult to understand the exact molecular structure [6]. However, homogalacturonan, which consists of at least 65% of the pectin molecule, is composed of a relatively simple linear chain of 1,4-linked α-d-galacturonic acids with C-6 carboxyl groups partially esterified [7]. When the degree of esterification is low, calcium ions can bind with carboxyl groups of the pectin chain resulting in the gelation of pectin solutions [8]. This binding interaction has been experimentally observed using Fourier Transform Infrared Spectroscopy (FTIR) [9, 10]. Previous simulation studies also found that calcium ions can bind with carboxyl groups on the pectin chain to form an egg-box-like structure, as shown in figure 3.1. Some studies found that in a similar system, hydroxyl groups also participate in ion coordination. When water molecules are present, calcium ions are partially solvated by water [11, 12]. Other divalent ions, such as copper and zinc ions, have also been shown to bind with pectin to different degrees [13].

In previous studies, it has been shown that the interaction between calcium chloride and pectin is essential to temperature sensitivity [4]. However, little is known about pectin's ion transport mechanisms and the origin of its temperature response. The lack of knowledge about the underlying molecular mechanisms governing petcin's temperature response hinders the optimization of this polyelectrolyte for sensing applications. Nevertheless, probing the ion transport mechanisms in this biopolymer is challenging. First of all, the composition and the structure of the RG section of

pectin are extremely complicated and not well understood. This renders nuclear magnetic resonance spectroscopy and many other spectroscopic results noisy and hard to decipher. Secondly, multiple factors could affect the interaction between cations and pectin. Type of ions, pH, degree of acetylation, and distribution pattern of carboxyl groups all can have a great impact on the ion-pectin coordination geometry and pectin's binding capacity [14]. Thirdly, there are multiple types of mobile ions present in the system: calcium ions, chloride ions, and protons from carboxyl groups. They all could be contributing to the overall ionic current and temperature sensitivity.

This paper focuses on the identification of the dominant current carrier in pectin and elucidates the causes of its high-temperature sensitivity. By comparing the electrical responses of systems with different amounts of chloride ions and protons, we found that calcium ions are the main current carrier in $CaCl_2$-crosslinked pectin. To understand the origin of the temperature sensitivity, we studied the electrical responses of pectin films crosslinked with nine types of multi-valent ions. Binding interactions between these ions and pectin were also investigated via infrared spectroscopy and density functional theory modeling. Combining these results, we conclude that the temperature sensitivity is correlated to the binding energy between the metal ion and pectin.

3.3 Results

First, we identified the main charge carrier responsible for the large temperature response. Three types of mobile ions present in the system were considered : (i) calcium ions, (ii) chloride ions, and (iii) protons from the carboxyl group. Assuming ideal electrolytes, the ion conductivity could be written as the sum of contributions from all mobile ions:

$$\sigma(T) = \sum_i \sigma_i(T) = \sum_i n_i(T)\mu_i(T)q_i \tag{3.1}$$

where n_i, μ_i, and q_i are the number density, the mobility, and the charge of the i-th type of mobile ions. T refers to the temperature. In general, both number densities and mobilities can depend on temperature, and the temperature response in this paper is defined as $\sigma(T_1)/\sigma(T_2)$ where $T_1 > T_2$. If protons are the dominant current carriers, then the temperature response of $CaCl_2$-crosslinked pectin should be similar to the uncrosslinked pectin, where protons are the only possible current carrier. However, previous studies found that the temperature response of uncrosslinked pectin films is less than 1/4th of the temperature response of $CaCl_2$-crosslinked
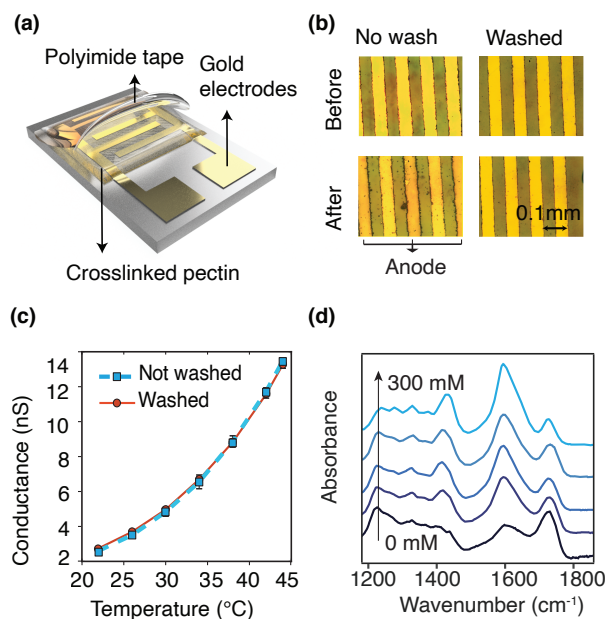
Figure 3.2: Identification of the dominant current carrier. (a) Schematic diagram of samples fabricated for electrical measurements. Pectin was deposited on the gold-interdigitated electrodes and then crosslinked with salt solutions. After dehydration, it was then sealed with polyimide tape. (b) Optical microscopy images of the gold interdigitated electrodes. The first (second) row corresponds to the electrodes before (after) the gold-dissolution electrochemical test. Compared to the first column, the sample measured using the electrodes in the second column was washed in deionized water before measurements. (c) The electrical properties of the washed sample (blue square) compared to the unwashed one (red circle). No significant difference was observed. The error bars are on the order of graph point size. (d) FTIR spectra of pectin cross-linked with 5 concentrations of $CaCl_2$: 0, 30, 80, 100, 300 mM.

pectin [4]. To further separate the contribution of (i) calcium ions from (ii) chloride ions and (iii) protons, we performed controlled experiments comparing the electrical properties of samples containing two different concentrations of chloride ions and protons. Pectin solution was drop casted on the gold electrodes (Fig. 3.2(a)) and then crosslinked with $CaCl_2$ solution (see the supplementary material for more details). One sample was immersed in DI water for a day to remove the chlorides and unbound protons. Calcium ions that deprotonated the carboxylic acid groups formed strong coordination with the negatively charged carboxylate groups that remained during the DI rinse. Both samples were dehydrated and subjected to a gold-dissolution electrochemical test (Fig. 3.2b). By applying 1 V of voltage to the pectin-deposited electrodes for 7 hours at room temperature, the surface of the gold anode was monitored. As expected, the unwashed samples turned red due to the formation of auric chloride from the reaction between gold and chloride ions in the acidic

environment [15], while no color change was observed from the DI rinsed samples. This confirmed that the rinsed pectin film contained significantly fewer chloride ions. Moreover, since this system must be electrically neutral after rinsing, the same number of protons must have been removed. Finally, the electrical responses of both rinsed and unrinsed samples were characterized by procedures described in the supplementary material. Their electrical conductance at varying temperatures is plotted in Fig. 3.2c. No significant difference in the electrical response was observed, suggesting that chloride ions and protons are not the dominant current carriers that cause the high-temperature response in the system.

Although we confirmed that calcium ions play an important role in pectin's high-temperature response, questions remain on what mechanisms gives rise to pectin's high-temperature response. Both the number density and the mobility of the current carriers could be temperature dependent and contribute to the thermal response. We first inspect the possibility of the charge carrier density being responsible for the pectin's temperature response. In this case, the number density of mobile calcium ions is expected to increase with increasing temperature. At an elevated temperature, the binding between calcium ions and the carboxyl groups becomes less stable, releasing the calcium ions to the surrounding. Since these unbound calcium ions are much more mobile than the bound calcium ions, the number density would be expected to increase, leading to higher conductivity. To test such hypothesis, we monitored how the number density of the bound calcium ions changes with respect to the applied voltage and temperature using infrared (IR) spectra. Three major absorption peaks were present from the crosslinked pectin in the range between 1500 cm^{-1} and 1800 cm^{-1}: Each corresponded to the asymmetric stretch of the carboxyl group (1733 cm^{-1}), the asymmetric stretch of the metal-ion-bound carboxylate group (1593 cm^{-1}), and the scissoring bend of the water molecules (1620 cm^{-1}) [9, 10]. As shown in Fig. 3.2(d), with increasing concentration of crosslinking $CaCl_2$, the peak corresponding to the metal-ion-bound carboxylate group rises while the peak corresponding to the carboxyl group diminishes. Therefore, the concentration of bound calcium ions could be measured using IR spectra. Interestingly, all four IR spectra of the $CaCl_2$ crosslinked pectin that were measured under different temperatures and conditions overlapped (Fig. 3.3a), suggesting that no significant change in the number density of bound/free calcium ions had occurred. Therefore, we can conclude that pectin's thermal response originates from the change in ion mobility.
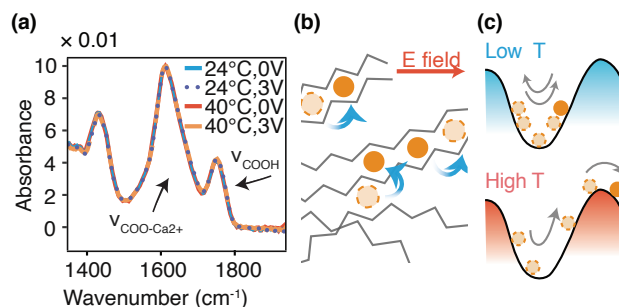
Figure 3.3: Temperature dependence of ion number density . (a) Infrared spectra of CaCl$_2$ crosslinked pectin film taken at 24 °C, with no voltage (light blue), 24 °C with 3 volts applied across the sample (dotted dark blue), 40°C with no voltage (red) and 40 °C with 3 volts applied across the sample (orange)the red line. (b) Schematic illustration showing how calcium ions hop from one solvation site to another in pectin chains. (c) Schematic showing the free energy surface for a calcium ion at a solvation site and its hopping activation energy E$_A$.

We postulate that the steep dependence of ion mobility on temperature arises from the strong binding strength between the calcium ions and pectin. With an applied electric field (Fig. 3.3b), bound calcium ions can hop to another site by crossing energy barriers (Fig. 3.3c). At elevated temperatures, this hopping frequency increases due to an increase in thermal energy resulting in a higher ion mobility and ion conductivity. Such phenomenon can be explained using the Arrhenius theory. To verify our claim, the electrical properties and binding strengths of pectin samples crosslinked with different multivalent salts were evaluated.

For electrical characterizations, we prepared samples crosslinked with 9 multivalent salts: CaCl$_2$, CuCl$_2$, FeCl$_2$, FeCl$_3$, BaCl$_2$, CoCl$_2$, ZnCl$_2$, AlCl$_3$ and MgCl$_2$. Each sample was deposited on an electrode surface and the current was measured by applying 100 mV across the electrodes. The temperature was cycled from 18 °C to 47 °C. The temperature response is defined as $\sigma_{45°C}/\sigma_{20°C} = I_{45°C}/I_{20°C}$, where $\sigma_{45°C}$, $\sigma_{20°C}$, $I_{45°C}$, and $I_{20°C}$ are the electrical conductivity and current amplitude at 45°C and 20°C, respectively. From the temperature responses measured over different cross-linking salts (Fig. 3.4a), we observed that the temperature response is highly dependent on the type of crosslinking metal ion, providing additional evidence to our previous conclusion that metal ions are the dominating current carriers. Also, copper shows the highest response value compared to other ions. However, no apparent trend was recognized between the temperature response and the size of ions or their valency. Nevertheless, all samples followed the Arrhenius relation: $I = I_o exp(-E_A/k_BT)$, where E_A is the activation energy for hopping, k_B
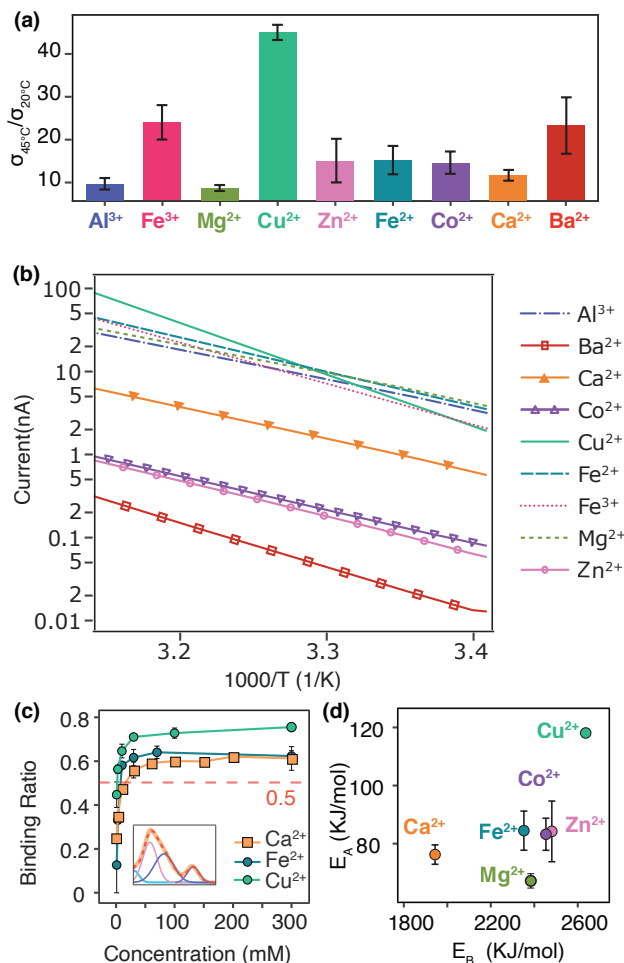
Figure 3.4: Activation energies and binding energies. (a) Temperature responses of pectin samples crosslinked by 9 different multivalent ions. Error bars are the standard deviations of at least 3 independent samples. The salts are ordered such that the ion size increases from left to right. (b) Arrhenius plots of pectin films crosslinked by the 9 different multivalent cations. (c) Binding curves for Ca^{2+}, Fe^{2+} and Cu^{2+}. The inset shows a typical fitting of a FTIR with 4 Gaussian peaks (shown as cyan, pink, blue and purple curves). The red dashed line corresponds to the overall fitting, and the yellow curve is the experimentally measured absorption data. (d) Activation energy E_A is compared with the binding energy E_B obtained from DFT simulation. The error bar for the copper ion is smaller than the graph point size.

is the Boltzmann constant, and T is the temperature, and I_0 is the pre-exponential factor, respectively (Fig. 3.4b). Such ion transport behavior in polymeric systems indicates independent ion hopping, without coupling with the polymer chains' segmental motion [16, 17]. Finally, the activation energy from each ion was extracted (Fig. 3.4d). Since the response is defined as a current ratio, temperature responses are exponentially dependent on activation energies.

To characterize and compare the affinity of ions to pectin, binding curves of $CuCl_2$, $CaCl_2$, $FeCl_2$, and $MgCl_2$ crosslinked pectin were measured using infrared spectroscopy (Fig. 3.4c). Binding curves explain how the percentage of bound metal ions (i.e., the binding ratio) change with the concentration of the crosslinking solution. To obtain the binding ratios, Gaussian peaks were fitted to each FTIR spectrum between 1500 cm^{-1} and 1850 cm^{-1} (Fig. 3.4c). For simple reactions,i.e. $M + L \rightleftharpoons ML$, and independent binding events, the dissociation constant K_d equals to the corresponding [L] when f_{ratio}=0.5 [18]. In these cases, the binding constant $K_a = 1/K_d$ and binding free energy $\Delta G = -k_B T ln K_a$ can be calculated easily. In the metal crosslinked pectin system, the binding process could be more complicated, including multiple binding steps and correlations between adjacent binding sites. However, to qualitatively compare the binding affinity between different ions, we use $[L]_{f=0.5}$ as an estimate of K_d[19]. We found that the binding affinity decreases as follows: $Cu^{2+} > Fe^{2+} \geq Ca^{2+} \gg Mg^{2+}$ (Fig. 3.4(c)). This order matches their corresponding order in temperature responses.

For further evaluation, binding energies between divalent ions and galacturonate were calculated using density functional theory (DFT) with ORCA package [20](see the supplementary material for more details). For each calculation, a negatively-charged galacturonate molecule, a metal ion, and 6 water molecules were included in the simulation. Finally, the binding energy was estimated using the following equation:

$$\Delta E = E_{Gal^-M^{2+}\cdot 6H_2O} - E_{Gal^-\cdot 6H_2O} - E_{M^{2+}}, \qquad (3.2)$$

where $E_{Gal^-M^{2+}\cdot 6H_2O}$ corresponds to the energy of the optimized galacturonate-metal-ion-water complex. $E_{Gal^-\cdot 6H_2O}$ is the single point energy of $Gal^- \cdot 6H_2O$ calculated at the optimized geometry of $Gal^-M^{2+} \cdot 6H_2O$. To confirm whether our model can properly represent the binding interaction between the metal ions and pectin in the metal-ion-crosslinked pectin system, frequency calculations were performed to generate the corresponding infrared spectra. The calculated spectra were then compared to the experimental results, which showed good agreement in the major peak locations (Fig. A.2). Due to the relativistic quantum effect that was not implemented in our calculation, the binding energy calculated from barium ions was inaccurate and excluded from the comparison [21]. Figure 3.4d shows the binding energies between metal ions and galacturonate E_A obtained from the DFT simulations, plotted against the activation energies E_B extracted from the Arrhenius plots in Fig. 3.4b. Overall, a positive correlation was observed. However, compared

to Ca^{2+}, Mg^{2+} showed surprisingly high binding energy with galacturonate, a result not observed in our experiments. This incongruity between experiments and numerical results is due to the high affinity of Mg^{2+} to water molecules. Earlier studies also found that Mg^{2+} has a much higher binding affinity to polygalacturonate than Ca^{2+} [13]. However, Mg^{2+} only polycondensates on polygalacturonic acid instead of crosslinking, because it is energetically unfavorable for Mg^{2+} to release water molecules from its solvation shell to bind with galactronate [13]. In our simulations, no ions bind with the hydroxyl group on the galacturonate molecule. This is because only one galacturonate molecule was included in the model, and it was sterically hindered for an ion to bind to both the carboxylate and hydroxyl groups. However, metal ions do coordinate with the hydroxyl groups in water molecules. With more galaturonate molecules present in the simulations, metal ions would also likely bind to the hydroxyl groups from other galacturonate molecules, as observed in other similar systems [12]. Considering the positive correlation observed between the activation and binding energies, from both experimental and simulation results, we conclude that the highly temperature dependent ion conductivity originates from the tight binding between calcium ion and pectin. Similar results were also demonstrated in a recent report, describing a polyelectrolyte similar to pectin, composed of 2-hydroxyethyl acrylate (HEA) and acrylic acid (AA) [22]. These findings further confirmed that the binding of calcium ions to carboxyl groups and hydroxyl groups is key to achieving high responsivity.

3.4 Conclusion

In this study, we elucidate the ion transport mechanism in dehydrated calcium pectinate. We identify calcium ions as the main current carrier of the system, and determine that conductivity is dominated by ion hopping, which is independent from the polymer segmental relaxation. We also demonstrate that the temperature dependency originates from changes in charge carrier mobility, rather than its number density. In addition, we show that the high activation energy is related to the strong binding between cation and galacturonate, specifically the carboxyl and hydroxyl groups. Finally, we highlight that Cu^{2+} cross-linked pectin is three-times more temperature responsive than Ca^{2+} cross-linked pectin, and therefore, the use of copper pectinate can significantly improve the thermal sensing performance for future developments and applications.

References

[1] Yecheng Wang, Kun Jia, Shuwen Zhang, Hyeong Jun Kim, Yang Bai, Ryan C Hayward, and Zhigang Suo. Temperature sensing using junctions between mobile ions and mobile electrons. *Proceedings of the National Academy of Sciences*, 119(4):e2117962119, 2022.

[2] Nguyen Thanh Tien, Sanghun Jeon, Do-Il Kim, Tran Quang Trung, Mi Jang, Byeong-Ung Hwang, Kyung-Eun Byun, Jihyun Bae, Eunha Lee, Jeffrey B-H Tok, et al. A flexible bimodal sensor array for simultaneous sensing of pressure and temperature. *Advanced Materials*, 26(5):796–804, 2014.

[3] Insang You, David G Mackanic, Naoji Matsuhisa, Jiheong Kang, Jimin Kwon, Levent Beker, Jaewan Mun, Wonjeong Suh, Tae Yeong Kim, Jeffrey B. H. Tok, et al. Artificial multimodal receptors based on ion relaxation dynamics. *Science*, 370(6519):961–965, 2020.

[4] Raffaele Di Giacomo, Luca Bonanomi, Vincenzo Costanza, Bruno Maresca, and Chiara Daraio. Biomimetic temperature-sensing layer for artificial skins. *Science Robotics*, 2(3):eaai9251, 2017.

[5] Beli R. Thakur, Rakesh K. Singh, Avtar K. Handa, and MA Rao. Chemistry and uses of pectin—a review. *Critical Reviews in Food Science & Nutrition*, 37(1):47–73, 1997.

[6] William G. T. Willats, Lesley McCartney, William Mackie, and J. Paul Knox. Pectin: Cell biology and prospects for functional analysis. *Plant Molecular Biology*, 47(1):9–27, 2001.

[7] Sebastian Wolf, Grégory Mouille, and Jérome Pelloux. Homogalacturonan methyl-esterification and plant development. *Molecular Plant*, 2(5):851–860, 2009.

[8] Ali Assifaoui, Adrien Lerbret, Huynh T. D. Uyen, Fabrice Neiers, Odile Chambin, Camille Loupiac, and Fabrice Cousin. Structural behaviour differences in low methoxy pectin solutions in the presence of divalent cations (ca 2+ and zn 2+): A process driven by the binding mechanism of the cation with the galacturonate unit. *Soft Matter*, 11(3):551–560, 2015.

[9] Ali Assifaoui, Camille Loupiac, Odile Chambin, and Philippe Cayot. Structure of calcium and zinc pectinate films investigated by ftir spectroscopy. *Carbohydrate Research*, 345(7):929–933, 2010.

[10] Eri Yamakita and Satoru Nakashima. Water retention of calcium-containing pectin studied by quartz crystal microbalance and infrared spectroscopy with a humidity control system. *Journal of Agricultural and Food Chemistry*, 66 (35):9344–9352, 2018.

[11] Isabelle Braccini and Serge Pérez. Molecular basis of Ca^{2+}-induced gelation in alginates and pectins: the egg-box model revisited. *Biomacromolecules*, 2 (4):1089–1096, 2001.

[12] Wojciech Plazinski. Molecular basis of calcium binding by polyguluronate chains. Revising the egg-box model. *Journal of Computational Chemistry*, 32 (14):2988–2995, 2011.

[13] Uyen T. D. Huynh, Adrien Lerbret, Fabrice Neiers, Odile Chambin, and Ali Assifaoui. Binding of divalent cations to polygalacturonate: A mechanism driven by the hydration water. *The Journal of Physical Chemistry B*, 120(5): 1021–1032, 2016. doi: 10.1021/acs.jpcb.5b11010. URL https://doi.org/10.1021/acs.jpcb.5b11010. PMID: 26771109.

[14] Miete Celus, Clare Kyomugasho, Ann M. Van Loey, Tara Grauwet, and Marc E. Hendrickx. Influence of pectin structural properties on interactions with divalent cations and its associated functionalities. *Comprehensive Reviews in Food Science and Food Safety*, 17(6):1576–1594, 2018.

[15] R. P. Frankenthal and D. J. Siconolfi. The anodic corrosion of gold in concentrated chloride solutions. *Journal of the Electrochemical Society*, 129(6): 1192, 1982.

[16] Chang Yun Son and Zhen-Gang Wang. Ion transport in small-molecule and polymer electrolytes. *The Journal of Chemical Physics*, 153(10):100903, 2020.

[17] Shujahadeen .B Aziz, Thompson J. Woo, M. F. Z. Kadir, and Hameed M. Ahmed. A conceptual review on polymer electrolytes and ion transport models. *Journal of Science: Advanced Materials and Devices*, 3(1):1–17, 2018.

[18] Donald Voet, Judith G. Voet, and Charlotte W. Pratt. *Fundamentals of biochemistry: Life at the molecular level*. Number 577.1 VOE. 2013.

[19] Rudolf Kohn. Ion binding on polyuronates-alginate and pectin. *Pure and Applied Chemistry*, 42(3):371–397, 1975.

[20] Frank Neese. The orca program system. *Wiley Interdisciplinary Reviews: Computational Molecular Science*, 2(1):73–78, 2012.

[21] Pekka Pyykkö. Relativistic effects in chemistry: *m*ore common than you thought. *Annual Review of Physical Chemistry*, 63:45–64, 2012.

[22] Tae Hyun Kim, Zhun Zhou, Yeong Suk Choi, Vincenzo Costanza, Linghui Wang, Joong Hwan Bahng, Nicholas J Higdon, Youngjun Yun, Hyunbum Kang, Sunghan Kim, et al. Flexible biomimetic block copolymer composite for temperature and long-wave infrared sensing. *Science Advances*, 9(6): eade0423, 2023.

Chapter 4

EFFECT OF WATER CONTENT ON THE ION TRANSPORT IN PECTIN FILMS

The work presented in this chapter has been adapted from:

- Linghui Wang, and Chiara Daraio. Effect of water content on the ion transport in pectin films. *In preparation*, 2023.

4.1 Abstract

Hydration plays an important role in determining the mechanical and electrical properties of biopolymers. However, the specific role of water on the conductive and dielectric processes in biopolymers is still not completely understood. Here, we study the effects of water content on the electrical response of crosslinked pectin, a biopolymer that shows record-high temperature sensitivity in its dehydrated state, and has potential in thermal sensing applications. We analyze impedance spectra taken at different hydration levels and study the relationship between DC conductivity and onset frequency. Two types of hydration's effect were identified: (i)with low water content, hydration improves ion conductivity through boosting the frequency of ion hopping; (ii) with high water content, hydration has a further effect on either the hopping distance or the concentration of charge carriers. Overall an increase in water content enhances pectin's ion mobility, by lowering the ion hopping activation energy, and decreases the temperature response. This finding presents a trade-off between conductivity and temperature sensitivity, suggesting an optimal water content needs to be determined for temperature sensing applications.

4.2 Introduction

Biopolymers have many potential industrial applications thanks to their biodegradability, biocompatibility, processability, and low cost [1–3]. In addition to their traditional role in the packaging and food industry, biopolymers' application in energy storage, photonics, sensing, and actuation have been widely investigated [4–7]. Commonly used biopolymers include cellulose, pectin, gelatin, chitosan and silk [8]. Many of these materials are hydrophilic, and their properties are highly dependent on their water content. Previous research has investigated moisture's effect on their

mechanical properties [9, 10]. For many applications, it is also vital to understand hydration's effects on their dielectric and electrically conductive properties.

In this work, we focus on the study of crosslinked pectin, a biopolymer with potential in thermal sensing applications [11–13]. Pectin has been reported to exhibit an order of magnitude higher response than other state-of-art temperature sensing materials [11]. Pectin is a complex polysaccharide and makes up about 30% of the dried substance of plant cell walls. Although its precise structure is complicated and still under debate, its backbone is mostly composed of 1-4 linked α-D-galacturonic acid with a certain degree of esterification [14]. For pectin with a low degree of esterification, gelation could be induced by adding calcium ions or other multivalent metal ions. In the gelation process, metal ions coordinate with carboxyl groups on multiple pectin chains and form crosslinks. Because of this property, pectin has been traditionally used as a gelling agent, and most previous studies focused on its gelation and mechanical properties in the hydrated state [15]. However, it was recently discovered that when metal-ion-crosslinked pectin is dehydrated, its electrical conductivity, originating from metal-ion hopping among the coordination sites [13], becomes highly dependent on temperature over a wide range of temperatures (10°C - 55°C) [11]. This record high temperature response is attributed to the strong binding between metal cations and pectin chains [13]. Similar to other biopolymers, the electrical properties of metal-ion-crosslinked pectin are sensitive to hydration, which poses a major challenge for device fabrication and calibration. When the water content is extremely low, its electrical conductivity vanishes. When it is too hydrated, its temperature response diminishes [12]. Additionally, temperature variations also affect pectin's equilibrium moisture content. To gain a full picture of pectin's ion transport and temperature response mechanism, it is necessary to understand how water content affects its dielectric and conductive properties.

Water could potentially affect the cross-linked pectin system in multiple ways (Fig. 4.1 (a)-(b)): First, water could act as a plasticizer for the pectin polymer matrix: solvating the polymer chain, weakening the interaction between polymer chains, and increasing the free volume of the polymer matrix. Second, because carboxylic acid is a weak acid, hydration could promote proton disassociation. Although it has been shown that calcium ions are the dominating current carriers at a dehydrated state [13], dissociated protons or hydroniums could contribute to the ionic current at a hydrated state. Third, due to the high dielectric constant of water, an increase in water content would lead to a decrease in the Bjerrum length, weakening the
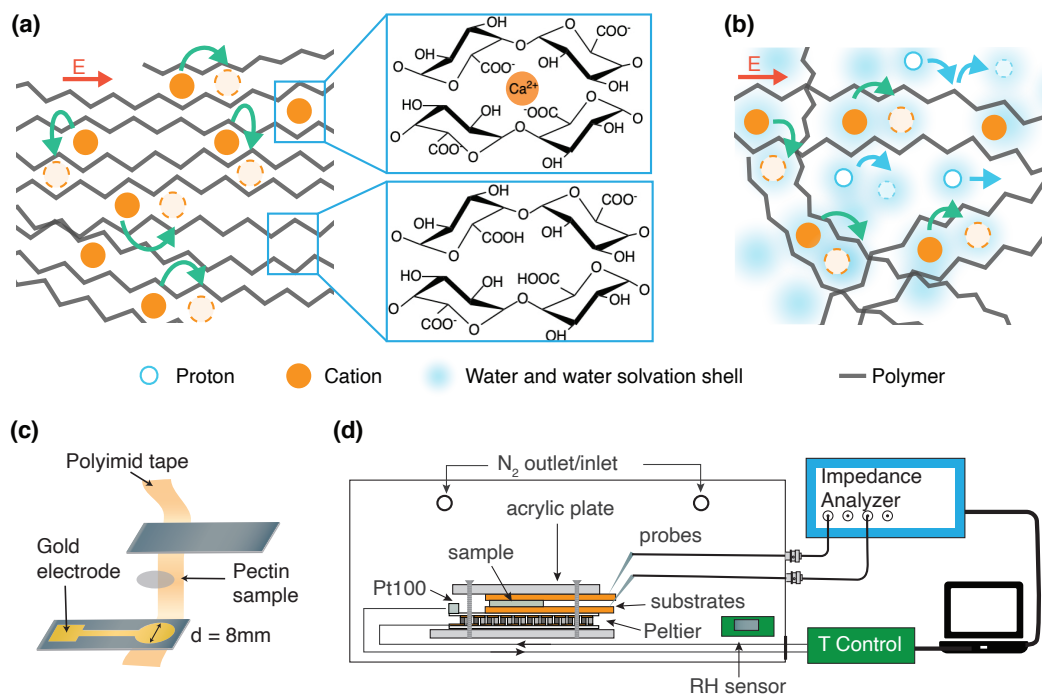
Figure 4.1: Schematics of Ion Transport and Measurement Setups (a) Schematic of calcium-ion transport in the crosslinked pectin at dehydrated states. (b) Calcium-ion transport in the hydrated states. (c) The schematics of the electrode configuration. A crosslinked pectin film is sandwiched by two gold electrodes with a diameter of 8mm. (d) The schematics of the measurement station.

electrostatic interaction between calcium ions and carboxylate groups. This effect would further enhance the mobility of calcium ions and lower their activation energy.

In this report, we use impedance spectroscopy (dielectric spectroscopy) to investigate the effect of water content on Ca^{2+} transport in $CaCl_2$-crosslinked pectin. Dielectric spectra have been broadly applied to study ion transport and other dielectric relaxation behaviors in polymeric systems at a different temperature, humidity, and pH[16–18]. Impedance spectroscopy probes the system at frequencies lower than optical spectroscopy, and it is used to decouple dielectric and conduction processes with different characteristic time constants.

4.3 Materials and methods

For sample fabrication, we use citrus pectin containing 34% methylation and 84% of galacturonic acid (Herbstreith & Fox) with a 59000 Dalton average molecular weight [12]. We prepare a pectin solution by dissolving pectin powder (1% w/v) in the deionized (DI) water at 80°C with stirring. A 30 mM $CaCl_2$ solution is

prepared by dissolving $CaCl_2$ powder (Sigma Aldrich) into DI water. To make a freestanding pectin film, we first pour pectin solution into a mold and then crosslink it using a 30 mM $CaCl_2$ solution. After 24 hours of gelation, we dehydrate the gel at room temperature for another 24 hours. We confirm that the gelation time is adequate by monitoring its infrared spectrum, which does not change for longer crosslinking times. After dehydration, we cut the pectin film using a biopsy punch. For impedance measurements (Fig.4.1 (c),(d)), we sandwich the pectin film between two gold electrodes. We then insulate the samples using polyimide tape, to slow down the moisture exchange between pectin and the environment. The temperature is controlled and set to 23°C during the impedance scans, using a Peltier element and a platinum thermometer. A voltage of 100 mV is applied to the electrodes and the current is measured using an MFLI Lock-in Amplifier (Zurich Instruments). To ensure consistency in water content during the scan, successive impedance spectra are collected and compared in pairs, with data only being recorded when the difference between the two spectra is less than 5%. To dehydrate the sample, we increase the temperature to 50°C for 10 min. Afterward, the temperature is reset to 23°C for another round of impedance data collection. To reach a very low water content and an environment's relative humidity (RH) of 10%, we also purge the measurement chamber with nitrogen.

4.4 Results and discussions

The spectra of the real part of the complex conductivity, measured at different hydration levels, are shown in Fig. 4.2(a), while the spectra of the imaginary part of the dielectric spectra are shown in Fig. 4.2(b). With increasing moisture content, the conductivity spectra shift towards higher conductivity values and higher frequency, suggesting that hydration not only enhances but also accelerates the underlying ion transport or dielectric processes. Three typical regions can be observed in the real part of the conductivity spectrum (Fig. 4.2(c)). They correspond to electrode polarization (region I), long-range ion transport (region II), and dielectric dispersion (region III). At low frequencies, where electrode polarization dominates, ions build up at oppositely charged electrodes and form electrical double layers. The exact impedance behavior in this region cannot be directly modeled. The impedance depends on the properties of the electrolyte, but can also be affected by the electrodes' roughness and electrodes' configuration[19]. In the long-range ion transport region, the electrode polarization effect diminishes and ions drift as in an infinite medium. The real part of conductivity plateaus, and this value is the DC ionic conductivity.
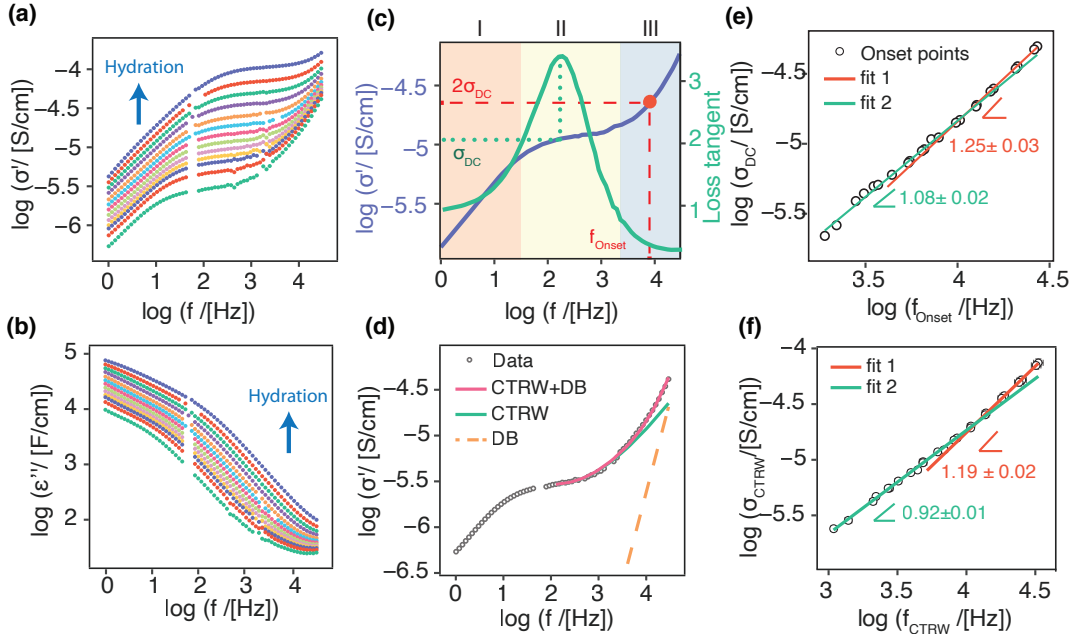
Figure 4.2: Impedance Spectra. (a) Real parts of the conductivity spectra taken at different water contents. (b) Imaginary parts of the dielectric spectra taken at different water contents (c) Schematic diagram showing the three regions of the conductivity spectrum and the model-free method used to extract σ_{DC} and f_{Onset}. (d) Schematic diagram showing the fitting of CTRW and DB model to a conductivity spectrum. (e) The DC conductivities and onset frequencies were extracted using the model-free method. (f) The DC conductivities and onset frequencies were extracted by fitting the CTRW+DB model. For (e) and (f), the error bars representing standard errors of fittings are on the order of graph point size.

When the frequency increases further, the conductivity crosses over to another region, known as the dielectric dispersion region. Here, the real part of the conductivity follows an apparent power law with respect to the frequency, i.e., $\sigma'(f) \propto f^n$. Multiple local dynamics can contribute to this power law behavior, such as hopping in disordered energy landscapes and segmental relaxations [20]. In disordered materials, such as ionic conducting glasses and amorphous semiconductors, the power law dependence stems from the wide probability distribution of the activation energy for ion hopping [21]. For polymeric materials, other dielectric processes could also occur, such as segmental relaxation (α relaxation) and β relaxations [22]. Segmental relaxations come from the micro-Brownian motion of chain segments, and β relaxations usually stem from the rotation of polar groups or conformational flips of a cyclic unit. However, because the measurements for our polymer were performed well below its glass transition temperature, only β relaxations are expected, which is commonly described using the Debye model.

In this system, the ionic conductivity can be written in general as:

$$\sigma(T) = n(c_w)\mu(c_w)q, \tag{4.1}$$

where n represents the number density, μ the mobility, q the number of charges of current carriers, and c_w denotes the water content. Both the number density and the ion mobility can depend on water content. In order to decouple water's effect on these two terms, we examined the relationship between DC ion conductivity and AC onset frequency [16]. AC onset frequency $f_{onset}(c_w)$ is the characteristic frequency at which the system transitions from long-range transport to local dynamics. It is interpreted as the ion hopping frequency. As a result, mobility can be expressed as $\mu \propto a^2 f_{onset}$, where a is the hopping distance. If water content only enhances the ion mobility and has no effect on the ion number density and the hopping distance, then with varying water content, we would have the following relation:

$$\log \sigma_{DC}(c_w) = \log f_{onset}(c_w) + C. \tag{4.2}$$

Here, C is a constant, and the slope of a plot of $\log \sigma_{DC}(c_w)$ versus $\log f_{onset}(c_w)$ is 1. However, if the number density changes or the hopping distance changes with water content, the relation would not necessarily be linear, and even when linear, its slope would be greater than 1.

To extract the DC conductivity and onset frequency, we applied both the model-free method (Fig. 4.2(c)) and the model-fitting method (Fig. 4.2(d)). In the model-free approach, the DC conductivity is taken as the real conductivity at the peak of a loss tangent spectrum [23]. The AC onset frequency is extracted by identifying the frequency satisfying $\sigma'(f_{Onset}) = 2\sigma_{DC}$ as it is defined in the Almond-West formalism [16, 24]. In the model fitting approach, the random barrier model with the continuous-time random walk approximation, which is referred to as CTRW model, is used to model ion transport in amorphous polymers. It assumes that ion hops in a spatially varying energy landscape, where the hopping activation energy follows a uniform distribution [25]. This model was frequently used to describe the dielectric dispersion region in glassy materials [25]. The region II and III of complex conductivity spectra were fitted to the following equation,

$$\sigma_{fit}(\omega) = \sigma_{CTRW} \frac{i\omega\tau_{CTRW}}{ln(1 + i\omega\tau_{CTRW})} + \frac{i\omega\epsilon_0\epsilon_{DB}}{1 + i\omega\tau_{DB}} + i\epsilon_\infty\omega, \tag{4.3}$$

where $\omega = 2\pi f$, while σ_{CTRW} and ϵ_{DB} are the strength parameters for the CTRW model and the Debye model respectively, and τ_{CTRW} and τ_{DB} are the corresponding time constants. Here, ϵ_∞ is the dielectric constant at the high-frequency limit.

The first term of the fitting function is derived from the CTRW model, accounting for the ion hopping behavior in disordered media. The time constant, τ_{CTRW}, corresponds to ions hopping over the largest barrier, E_{max}, in the percolation path, and it is proportional to $\exp(-E_{max}/k_B T)$. The inverse of this $f_{CTRW} = 1/\tau_{CTRW}$ corresponds to the AC onset frequency, where long-range ion transport is not possible at higher frequencies. Since we neglect electrode polarization processes, $\sigma_{DC} = \sigma_{fit}(\omega = 0) = \sigma_{CTRW}$. The second term comes from the Debye model accounting for the segmental relaxation of the side chain. Although the characteristic frequency of the segmental relaxation is above our measurement range, this phenomenon is still discernible, especially in the dehydrated samples. As shown in figure 4.2(b), above 10 kHz, the ϵ'' starts to increase with frequency, indicating the emergence of dielectric relaxation. In the hydrated sample, this increase is masked by the long-range transport. Considering the frequency range and the polymeric nature of our system, this dielectric relaxation is probably a type of polymer segmental relaxation. Since there is at least a 1.5 order of magnitude difference between the characteristic timescales of these two processes, we assume there is no coupling between them, and their contributions to the overall conductivity are simply added. Finally, the third term takes into account the bound charge polarization [21]. An example of the fitting to the original data is shown in figure 4.2(d). Fitting to spectra at all water content levels, both real and imaginary parts are plotted in figure B.1 (a)-(d).

The relationship between DC conductivities and onset frequencies extracted using the model-free method and model-fitting method are plotted in figure 4.2 (e) and (f). Compared with the model fitting method, the model-free method is less robust against noise in the measurement, especially at around onset frequency. Although the absolute value of the slopes extracted using the two methods differs slightly, in both plots we observed an increase in the slope with hydration. At low hydration levels, the slope is closer to 1, suggesting that the increase in the ion conductivity mainly comes from the enhancement in the calcium ion mobility. At high water content, the slope increases, indicating either a rise in the density of charge carriers or an increase in hopping distance. The rise in hopping distance with hydration may stem from a rise in free volume due to reduced electrostatic interaction between polymer chains. The increase in the number density of current carriers, although has not been reported with hydration, has been observed in other ionic conductive materials with increasing temperature, where the number density of current carriers are thermally activated [26]. Besides calcium ions, this increase in number density can also be a
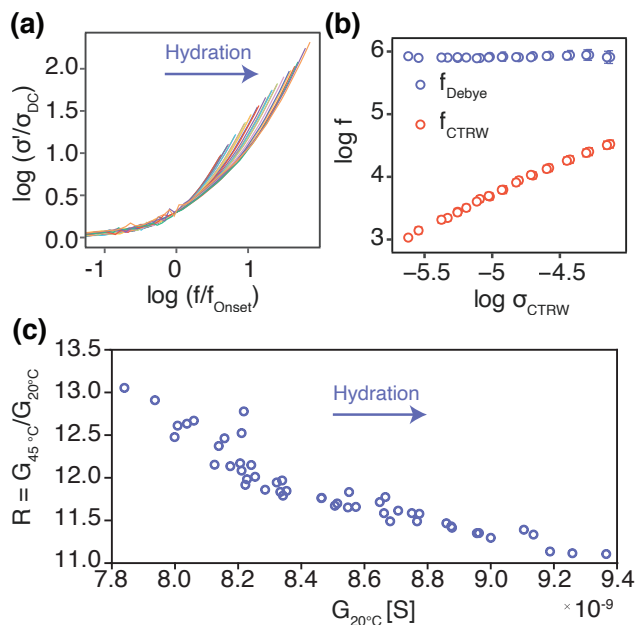
Figure 4.3: Deviation from the Principle of Time-Humidity Superposition and the Temperature Response. (a) Impedance spectra taken at different hydration levels, superimposed by scaling parameters σ_{DC} and f_{Onset}. (b) $f_{Debye} = 1/\tau_{DB}$ and $f_{CTRW} = 1/\tau_{CTRW}$ are plotted against σ_{CTRW}, as an indicator of the hydration level. The standard errors for the fittings are on the order of the graph point sizes. (c) Relation between temperature response and conductance, at 20°C. The temperature response is defined as the ratio of the conductance at 45 °C and the conductance at 20 °C. With hydration, the conductance increases and the temperature response decreases. Temperature measurements were conducted in accordance with the methodology outlined in the previous chapter [13].

result of proton transport: at elevated water content, protons could dissociate from carboxyl groups and start to contribute to the overall ion conductivity. Overall, when the sample is hydrated, further hydration would not only enhance the mobility of current carriers but also increase their number density. We also examine whether the time-hydration superposition principle (THSP) holds in the crosslinked pectin, by superimposing the impedance spectra at different hydration levels (Fig. 4.3 (a)). THSP is an analogy to the well-known time-temperature superposition principle [16]. It implies that hydration does not cause fundamental changes to the ion conduction and dielectric processes, only speeding up all the processes by the same ratio. Previous studies found that polyelectrolyte complexes follow THSP [16, 26]. However, when we try to superimpose our spectra at different water contents, we find disagreement at high frequencies (Fig. 4.3(a)). As shown in figure 4.3(b), this discrepancy can be understood by analyzing how the time constants of the CTRW model and segmental relaxation vary with hydration. Compared to the ion

hopping process, the characteristic frequency of the dielectric relaxation is much less sensitive to hydration. This difference leads to shape changes in the overall conductivity spectrum with hydration.

The rise in f_{CTRW} with hydration has another significant implication. As mentioned previously, f_{CTRW} is exponentially dependent on $-E_{max}$. This indicates that with increasing water content, the maximum activation energy barrier in the material decreases. This is consistent with our observation that the temperature response $R = \sigma(T_2)/\sigma(T_1) \propto \exp\left(-\frac{E_{max}}{k_B}\right)$ decreases with hydration (Fig. 4.3(c)). Additionally, a previous study has shown that the activation energy is correlated with the binding energy between the crosslinking metal ion and pectin [13]. Consequently, this reduction in activation energy can be attributed to the weakened binding due to the water's screening effect on the electrostatic attraction between calcium ions and carboxylate groups in pectin.

4.5 Conclusion

In summary, we examined the effect of hydration on the ion transport and dielectric processes in crosslinked pectin. We discovered that, in the dehydrated state, the rise in ion conductivity with hydration is mostly linked to the increase in ion mobility. However, in the more hydrated states, not only does the mobility increase but there is either a rising number of current carriers or an increase in the hopping distance. Additionally, the THSP is not valid in crosslinked pectin, indicating that different conduction processes were affected differently by hydration. Finally, higher hydration lowers the activation energy landscape, which explains the reduced temperature response observed in the previous studies. The trade-off between temperature response and ion conductivity with varying water content presented in this paper highlights the need for determining the optimal water content in crosslinked pectin to ensure its successful application in temperature sensing.

References

[1] Chunya Wang, Tomoyuki Yokota, and Takao Someya. Natural biopolymer-based biocompatible conductors for stretchable bioelectronics. *Chemical Reviews*, 121(4):2109–2146, 2021.

[2] Shimelis Admassie, F. N. Ajjan, Anders Elfwing, and Olle Inganäs. Biopolymer hybrid electrodes for scalable electricity storage. *Materials Horizons*, 3 (3):174–185, 2016.

[3] Xiaoqian Li, Changshuai Ding, Xiaomeng Li, Huige Yang, Shuiren Liu, Xianghong Wang, Linlin Zhang, Qingqing Sun, Xuying Liu, and Jinzhou Chen. Electronic biopolymers: From molecular engineering to functional devices. *Chemical Engineering Journal*, 397:125499, 2020.

[4] Mein Jin Tan, Shu Zhong, Rui Wang, Zhongxing Zhang, Vijila Chellappan, and Wei Chen. Biopolymer as an electron selective layer for inverted polymer solar cells. *Applied Physics Letters*, 103(6):147_1, 2013.

[5] Saeed Mardi, Pietro Cataldi, Athanassia Athanassiou, and Andrea Reale. 3d cellulose fiber networks modified by pedot: Pss/graphene nanoplatelets for thermoelectric applications. *Applied Physics Letters*, 120(3):033102, 2022.

[6] Yushu Wang, Wenwen Huang, Yu Wang, Xuan Mu, Shengjie Ling, Haipeng Yu, Wenshuai Chen, Chengchen Guo, Matthew C. Watson, Yingjie Yu, et al. Stimuli-responsive composite biopolymer actuators with selective spatial deformation behavior. *Proceedings of the National Academy of Sciences*, 117 (25):14602–14608, 2020.

[7] Emily M. Heckman, Joshua A. Hagen, Perry P. Yaney, James G. Grote, and F. Kenneth Hopkins. Processing techniques for deoxyribonucleic acid: Biopolymer for photonics applications. *Applied Physics Letters*, 87(21): 211115, 2005.

[8] Chen Cui, Qingjin Fu, Lei Meng, Sanwei Hao, Rengang Dai, and Jun Yang. Recent progress in natural biopolymers conductive hydrogels for flexible wearable sensors and energy devices: Materials, structures, and performance. *ACS Applied Bio Materials*, 4(1):85–121, 2020.

[9] Chi Zhang, Ali Shomali, Robert Guyer, Sinan Keten, Benoit Coasne, Dominique Derome, and Jan Carmeliet. Disentangling heat and moisture effects on biopolymer mechanics. *Macromolecules*, 53(5):1527–1535, 2020.

[10] Iryna Yakimets, Sabrina S. Paes, Nikolaus Wellner, Andrew C. Smith, Reginald H. Wilson, and John R. Mitchell. Effect of water content on the structural reorganization and elastic properties of biopolymer films: A comparative study. *Biomacromolecules*, 8(5):1710–1722, 2007.

[11] Raffaele Di Giacomo, Luca Bonanomi, Vincenzo Costanza, Bruno Maresca, and Chiara Daraio. Biomimetic temperature-sensing layer for artificial skins. *Science Robotics*, 2(3):eaai9251, 2017.

[12] Vincenzo Costanza, Luca Bonanomi, Giovanni Moscato, Linghui Wang, Yeong Suk Choi, and Chiara Daraio. Effect of glycerol on the mechanical and temperature-sensing properties of pectin films. *Applied Physics Letters*, 115(19):193702, 2019.

[13] Linghui Wang, Tae Hyun Kim, Vincenzo Costanza, Nick Higdon, and Chiara Daraio. Ion transport in thermal responsive pectin film. *Under preparation*.

[14] William G. T. Willats, Lesley McCartney, William Mackie, and J. Paul Knox. Pectin: cell biology and prospects for functional analysis. *Plant Molecular Biology*, 47(1):9–27, 2001.

[15] Beli R. Thakur, Rakesh K. Singh, Avtar K. Handa, and M. A. Rao. Chemistry and uses of pectin—a review. *Critical Reviews in Food Science & Nutrition*, 37(1):47–73, 1997.

[16] C Cramer, S De, and M Schönhoff. Time-humidity-superposition principle in electrical conductivity spectra of ion-conducting polymers. *Physical Review Letters*, 107(2):028301, 2011.

[17] Daniel Fragiadakis, Shichen Dou, Ralph H. Colby, and James Runt. Molecular mobility and li$^+$ conduction in polyester copolymer ionomers based on poly (ethylene oxide). *The Journal of Chemical Physics*, 130(6):064907, 2009.

[18] Yangyang Wang, Alexander L. Agapov, Fei Fan, Kunlun Hong, Xiang Yu, Jimmy Mays, and Alexei P. Sokolov. Decoupling of ionic transport from segmental relaxation in polymer electrolytes. *Physical Review Letters*, 108(8): 088303, 2012.

[19] Paul Ben Ishai, Mark S. Talary, Andreas Caduff, Evgeniya Levy, and Yuri Feldman. Electrode polarization in dielectric measurements: A review. *Measurement Science and Technology*, 24(10):102001, 2013.

[20] Ivan Popov, Shiwang Cheng, and Alexei P. Sokolov. Broadband dielectric spectroscopy and its application in polymeric materials. *Macromolecular Engineering: From Precise Synthesis to Macroscopic Materials and Applications*, pages 1–39, 2022.

[21] Jeppe C. Dyre and Thomas B. Schrøder. Universality of ac conduction in disordered solids. *Reviews of Modern Physics*, 72(3):873, 2000.

[22] Anthony R Blythe, Tony Blythe, David Bloor, et al. *Electrical properties of polymers*. Cambridge university press, 2005.

[23] Robert J Klein, Shihai Zhang, Shichen Dou, Brad H Jones, Ralph H Colby, and James Runt. Modeling electrode polarization in dielectric spectroscopy: Ion mobility and mobile ion concentration of single-ion polymer electrolytes. *The Journal of chemical physics*, 124(14):144903, 2006.

[24] Jeppe C Dyre, Philipp Maass, Bernhard Roling, and David L Sidebottom. Fundamental questions relating to ion conduction in disordered solids. *Reports on Progress in Physics*, 72(4):046501, 2009.

[25] Jeppe C Dyre. The random free-energy barrier model for ac conduction in disordered solids. *Journal of Applied Physics*, 64(5):2456–2468, 1988.

[26] AW Imre, M Schönhoff, and C Cramer. Unconventional scaling of electrical conductivity spectra for pss-pdadmac polyelectrolyte complexes. *Physical review letters*, 102(25):255901, 2009.

Chapter 5

FLEXIBLE BIOMIMETIC BLOCK COPOLYMER COMPOSITE FOR TEMPERATURE AND LONG-WAVE INFRARED SENSING

The work presented in this chapter has been adapted from:

- Tae Hyun Kim , Zhou Zhun, Yeong Suk Choi, Vincenzo Costanza, Linghui Wang, Joong Hwan Bahng, Nicholas J. Higdon, Youngjun Yun,Hyunbum Kang, Sunghan Kim and Chiara Daraio. Flexible biomimetic block copolymer composite for temperature and long-wave infrared sensing. *Science Advances*, 9.6, 2023.

5.1 Abstract

Biological compounds often provide clues to advance material designs. Replicating their molecular structure and functional motifs in artificial materials offers a blueprint for unprecedented functionalities. Here, we report a flexible biomimetic thermal sensing (BTS) polymer that is designed to emulate the ion transport dynamics of a plant cell wall component, pectin. Utilizing a simple yet versatile synthetic procedure, we engineer the physicochemical properties of the polymer by inserting elastic fragments in a block copolymer architecture, making it flexible and stretchable. The thermal response of our flexible polymer outperforms current state-of-art temperature sensing materials, including vanadium oxide, by up to two orders of magnitude. Thermal sensors fabricated from these composites exhibit a sensitivity that exceeds 10 mK and operates stably between 15 to 55 °C, even under repeated mechanical deformations. We demonstrate the use of our flexible BTS polymer in two-dimensional arrays for spatio-temporal temperature mapping and broadband infrared photodetection.

5.2 Introduction

Organic electronic materials are emerging as competitive alternatives to conventional silicon-based microelectronics due to their low-cost manufacturing [1, 2] and multi-functionality [3, 4]. The ability to tailor their properties at the molecular level makes them appealing for a range of sensing applications, such as wearable and implantable devices, which require specific characteristics that are difficult to

achieve with inorganic compounds like flexibility and stretchability. The increasing demand for all-organic electronic devices has led to the developments of a growing number of soft and active materials for a variety of physical [5, 6] and biochemical sensors [7, 8], paralleled by the advancements in elastic substrates and conductors [9, 10], as well as in their fabrication and integration strategies [11, 12].

Organic thermal sensors have also been proposed for remote healthcare, robotics, as well as environmental and industrial monitoring applications [10, 13]. However, thermal sensing devices relying on organic materials are often limited by their response performance, which is not yet comparable to their inorganic counterparts. Several approaches have been suggested to improve materials' response to temperature, for example, by using inorganic fillers, nano-composites, volume expansion, or the use of transistor-type devices for signal amplification [14–17]. However, these strategies generally involve complex fabrication steps and device architectures, function in narrow temperature ranges, or provide limited response.

To overcome these limitations, it is necessary to develop organic materials that intrinsically present high thermal response and flexibility in a relatively simple scaffold that can be fabricated to scale with reproducible performance. However, the ability to design new materials depends on understanding the fundamental transport mechanism and structural dynamics in organic molecules [18, 19], and on linking these properties to their functional characteristics. Although promising advances have been made, for example, with first principle simulations and data driven approaches [20, 21], the field is still lacking predictive models for the design and synthesis of such materials. One approach to design new materials is to gain insights from building blocks found in biological matters and to emulate their structures in synthetic materials.

Recent investigations of plant cell wall components reported that pectin, a structurally and functionally complex acid-rich polysaccharide [22], has a remarkable response to temperature [23–25]. Pectin consists mostly of repeating units of D-galacturonic acid (Fig. 5.1 A). At neutral pH, the D-galacturonic acid units of low-ester pectin form ionic bridges with Ca^{2+}, creating an "egg-box" complex in which cations are encapsulated [26, 27]. Increasing the temperature of a Ca^{2+}-crosslinked pectin results in an exponential increase of ionic conduction [23, 24]. However, pectin is most abundantly found in agricultural products, e.g., fruit peels, and its chemical composition is directly influenced by climate, plant origins, and extraction methods [28]. As such, devices fabricated with pectin, as a sensing

element, present inconsistent electronic properties and demonstrate poor structural stability.

Here, we introduce a new flexible biomimetic thermal sensing (BTS) polymer that emulates the structure and functional motifs of pectin. The synthetic BTS polymer composite exhibits superior thermal sensitivity while also being mechanically robust and flexible (Fig. 5.1B). The basic architecture consists of an ABA-type triblock copolymer, synthesized through reversible addition-fragmentation chain transfer (RAFT) polymerization (Fig. C.1A), which is a versatile living radical polymerization method used to engineer structures with intrinsic mechanical flexibility (thermoplastic elastomers), suitable for organic electronic materials [29–31].

5.3   Materials and methods

Materials

2-hydroxyethyl acrylate (HEA), tert-butyl acrylate (t-BA), n-butyl acrylate monomers (n-BA), and a dual-functional chain transfer agent (CTA) S,S-dibenzyl trithiocarbonate (DBTTC) were purchased from Sigma-Aldrich. DBTTC was used to expedite the synthesis of the ABA polymer for multi-step processing (43). Azobis (isobutyronitrile) (AIBN), a radical initiator, was purchased from Sigma Aldrich and recrystallized from methanol prior to use.

Synthetic procedure of the ABA block copolymer

ABA type block copolymers were prepared via a reversible addition-fragmentation chain transfer (RAFT) polymerization (Fig. 2.2A). During the entire polymer synthesis process, the resulting material was characterized using gel permeation chromatography (GPC) and nuclear magnetic resonance (1H NMR) (Fig. C.2) (44). First, N_2 purged 2-hydroxyethyl acrylate **1** (1.16 g, 10 mmol) and tert-butyl acrylate **2** (1.28 g, 10 mmol) were dissolved in 2 mL of dimethylformamide (DMF), followed by DBTTC **3** (29 mg, 0.1 mmol). The mixture was further purged with N_2 for 3 minutes. Next, AIBN (0.81 mg, 5 μmol) was added into the reactor and finally stirred at 75 °C under inert N_2 atmosphere. The reactor was cooled down and vented to air. The residual monomers (tert-butyl acrylate and 2-hydroxyethyl acrylate) were removed by vacuum, following precipitation in 100 mL of cold diethyl ether which resulted in a yellow oil of bis[p(t-BA10-r-HEA10)] trithiocarbonate (macro-CTA). The yield of polymerization monitored using 1H NMR was 80 % (2.02 g). Next, the macro-CTA was mixed with N_2 purged n-butyl acrylate 4 (12.8 g, 100 mmol) and
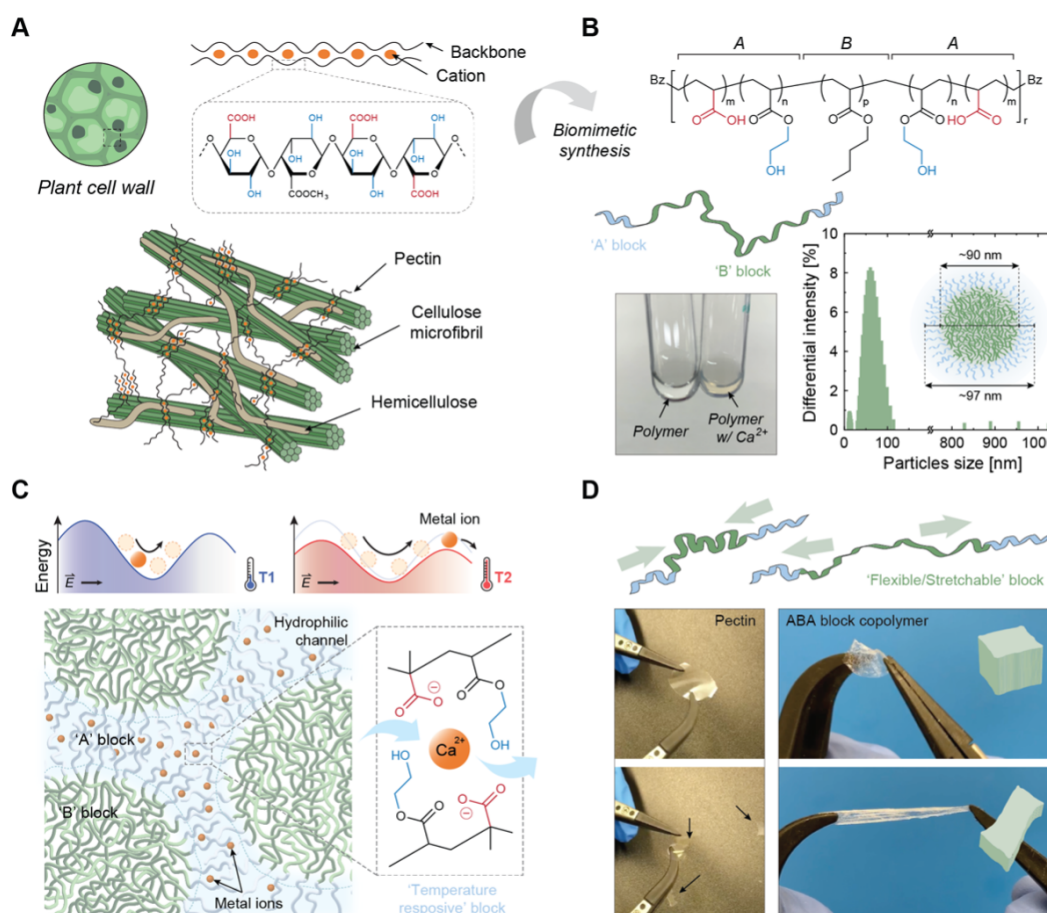
Figure 5.1: Biomimetic design of the flexible BTS polymer. (A) Schematic illustration of the plant cell wall structure and of pectin. (B) Design of the ABA type block copolymer, with m = 5; n = 5; p = 100; r = 85.7. The hydrophilic 'A' block, rich in carboxyl (red) and hydroxyl (blue) groups, is designed to electrostatically interact with metallic cations. The hydrophobic 'B' block, composed of poly (n-butyl acrylate), is designed to provide mechanical flexibility and stretchability to the network. As shown in the particle size measurement (bottom right), the synthesized polymer exists in a colloidal state in ethanol due to phase separation. (C) Mechanism governing the temperature response of the synthetic block copolymer. Rearrangement of the potential wells at low and high temperature in which the cations are confined (top). When an external electric field is applied, temperature rises cause an increase of ion migration through the hydrophilic channels formed between the colloidal particles in the polymer matrix (bottom). (D) Mechanical flexibility and stretchability of the synthetic block copolymer. The dried pectin film is prone to tear after a slight bending deformation (left), whereas the composite polymer is robust to repeated stretching motions due to the soft 'B' block (right).

AIBN (0.81 mg, 5 μmol), along with 15 mL of DMF. The mixture was purged again under N_2 for 3 minutes, followed by stirring at 75 °C under N_2 atmosphere. The reactor was cooled down and vented to air. Residual n-butyl acrylate was removed by vacuum to yield a protected form of ABA block copolymer, p[(t-BA5-r-HEA5)-b-(n-BA)100-b-(t-BA5-r-HEA5)]r. Here, a conversion rate of 81 % was achieved (11.24 g). Finally, 1 g of the protected polymer was dissolved in 3 mL of dichloromethane (DCM) and combined with 3 mL of trifluoroacetic acid (TFA). The deprotection reaction was carried out at room temperature (RT) and stirred overnight. DCM and TFA were removed by vacuum, after precipitating the polymer in cold diethyl ether. As a result, a highly sticky yellow oil as the final form of the deprotected ABA block copolymer, p[(AA5-r-HEA5)-b-(n-BA)100-b-(AA5-r-HEA5)]r, was produced. The conversion of tert-butyl groups into acrylic acid was confirmed using 1H NMR from the deprotected block copolymer (100 % conversion to AA form).

Polymer characterization

The size of the colloidal particle formed in ethanol was measured using a Zeta-potential & Particle size Analyzer (Otsuka Electronics ELSZ-2000) at room temperature (Fig. 5.2B and Fig. 2.2B). After dissolving the samples in deuterated dichloromethane (CD_2Cl_2), nuclear magnetic resonance (NMR) spectra were obtained using Bruker Ascend 500 (500MHz). Spectral analysis was performed using Topspin 3.2 software. Gel permeation chromatography (GPC) was carried out in tetrahydrofuran (THF) on two MZ-Gel (10 μm) columns composed of styrene-divinylbenzene copolymer (Analysentechnik) connected in series with a miniDAWN TREOS multiangle laser light scattering (MALLS) detector. The film formation of the block copolymer was monitored in-situ from the composite mixtures using attenuated total reflectance fourier transform infrared spectroscopy (ATR-FTIR) using a Nicolet iS50 FTIR spectrometer. The synthesized block copolymer was dissolved in ethanol (1 mg/1 mL) with metal ions (0.3 M), mixed, and placed on top of the ATR module and continuously dried in air at 22 °C under 23 % relative humidity. The ATR-FTIR spectra were obtained as a function of time. Table C.5 summarizes the composition of the tested mixtures.

Thermal gravimetric analysis (TGA) was carried out on dried composite films (20 mg) using a Discovery TGA (Thermo Fisher Scientific) with the following settings: 10 °C/min ramp rate, 30 °C – 650 °C temperature range, and 10 mL/min N_2 flow rate. For material identification, TGA-FTIR measurements were performed in parallel to TGA, to analyze the gas phase FTIR spectra using a Nicolet iS50 FTIR
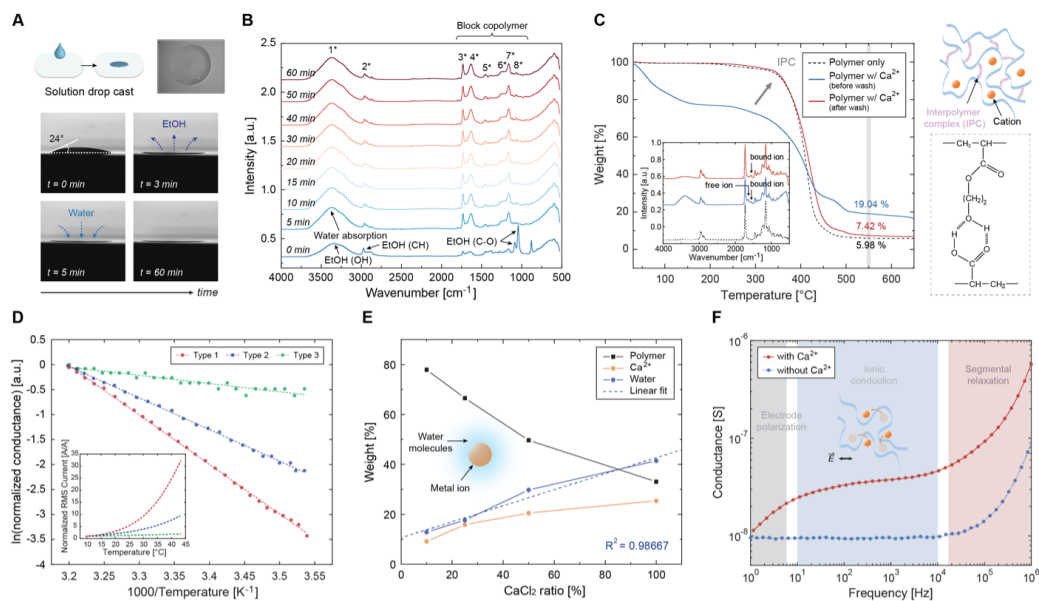
Figure 5.2: Film formation behavior and component analysis of the block copolymer.
(A) Digital images of the crosslinked block copolymer solution drop-casted on a flexible plastic substrate. The amount of crosslinking metal ions used for all tests is fixed to 100 % unless otherwise stated. (B) Time series of ATR-FTIR spectra after polymer deposition. During 1-hour air dry, ethanol starts to evaporate and subsequently water is absorbed and saturated by the hygroscopic regions in the polymer matrix. *Peak assignments of the ATR-FTIR spectra (Table C.4). (C) TGA profile of the polymer film before and after washing in deionized water. Titration analysis is performed to determine the percent of IPC formed in composite film based on the amount of bounded metal ions after wash. Inset: Corresponding FITR spectra of the films. (D) Arrhenius plot of different block copolymers. Activation energy compared between different polymer films with varying ratio of carboxyl to hydroxyl functional groups (type 1: m = 5, n = 5, p = 100, type 2: m = 4, n = 7, p = 100, type 3: m = 10, n = 0, p = 100). Inset: Corresponding thermal response of each type of polymer compared. Measurements are performed using the electrode design fabricated in Fig. C.6B with an AC voltage bias of 300 mV, at 200 Hz. (E) Relation between the concentration of metal ions in the composite film and amount of water adsorbed. Weight percentage of the polymer, Ca^{2+}, and water is calculated based on the TGA profile and the coupled gas-phase FTIR spectra of the dried polymer films (Fig. C.5) with varying amount of $CaCl_2$ (Table C.5). A linear relationship is observed between the $CaCl_2$ concentration and water absorbed by the composite film. (F) Impedance spectra of the polymer film with and without Ca^{2+}.

spectrometer. The spectrometer was equipped with an auxiliary experiment module (AEM), composed of an optional mercury cadmium telluride (MCT) detector, a 10 cm path-length nickel-plated aluminum flow cell, and an integrated digital temperature controller. After the integrated digital controller reached a constant 130 °C temperature, FTIR spectra were collected every 5 minutes between 0 and 65 minutes. For each measurement, a total of 32 scans were averaged with 4 cm^{-1} resolution. Impedance spectroscopy analysis was performed using an impedance analyzer (Zurich Instruments MFIA). AC frequency was swept between 1 to 100 MHz (100 points) with a voltage biased at 1 V.

Percentage of IPC formed in the polymer film was calculated using AA-Ca^{2+} titration method with the assumption that two AA functional groups are involved to form coordination bond with a single Ca^{2+}. To begin with, the total amount of AA and metal ions (100 % CaCl$_2$) in the polymer solution mixture was calculated (Table C.6). Next, the TGA and FTIR spectrum of the composite film was measured before and after washing with DI water. (Fig. 5.2 C). To completely rinse out the unbound metal ions from the polymer matrix, the film was soaked in 200 cc of DI water excessively with continuous stirring (120 rpm) at room temperature for 72 hours and dried. The proportion of Ca^{2+} bound to the polymer was calculated by subtracting the weight percentage between the two TGA profile at 550 °C which corresponds to the residual content of metal ions (chelated Ca^{2+} with AA = 11.62 %, free Ca^{2+} = 88.38 %). The free and bound Ca^{2+} ions were recognized from the FTIR spectra (inset of Fig. 5.2 C) at 1640 cm^{-1} and 1560 $^{-1}$, respectively. Based on the number of Ca^{2+} ions bound to the polymer film, percentage of AA used to from IPCs was estimated as 86.13 % (Table C.6).

Device fabrication

The block copolymer was dissolved in anhydrous ethanol at a concentration of 0.15 g/mL. Simultaneously, metal ion salt (CaCl$_2$) was dissolved in anhydrous ethanol at a concentration of 0.3 M. The ionically crosslinked polymer solution was obtained by mixing the two solutions at a volume ratio of 1:2. To fabricate the flexible temperature sensors, a thin sheet of polyester terephthalate (PET, 20 μm) was washed and attached to a 4-inch silicon wafer. On top, a layer of photoresist was spin coated and patterned using standard lithography process. The surface was then treated with O2 plasma (Plasma-Therm SLR 720) followed by Ti/Au evaporation (CHA Mark 40 electron beam evaporator) with thickness of 200/1000 Å. The entire sheet was immersed in acetone for metal lift-off, exposing the circular shaped interdigitated

electrodes (D = 4 mm, 30 μm wide with 20 μm spacing). Finally, the PET sheet with the patterned electrodes was released, rinsed and dried for use. Next, a total of 5 μL of crosslinked polymer solution was drop cast on top of each sensing pixels and dried at RT for 1 hour. To test different hydration status for optimal temperature response, the composite polymer was further dehydrated using dry air and sealed using a permeable PI tape. For cyclic studies, a thin layer of parylene-C (2 μm, ParaTech LabTop 3000 Parylene coater) was conformally coated around the devices to prevent water absorption or evaporation. External electrical connection was made using an anisotropic conductive film or an electrical probe set. The cross-sectional view of the fabrication process is shown in Fig. C.6A.

5.4 Results

Design of the flexible BTS polymer

To mimic pectin's temperature response, we conceptualize the polymer architecture by reducing the complex pectin structure to a simpler backbone, bearing only the minimally required cues for the desired functions. We hypothesize that the carboxyl groups, hydroxyl groups, and the conformation of sugar pockets are all essential components within the D-galacturonic acid that chelate divalent cations forming the "egg-box" complex [26, 32]. In the ABA architecture, the 'A' blocks represent two flanking hydrophilic regions, displaying motifs that can bind with divalent cations, composed of random placement of 2-hydroxyethyl acrylate (HEA) and acrylic acid (AA). Upon chelating with divalent cations, the 'A' blocks present a temperature response mechanism similar to that of pectin (Fig. 5.1 C). However, the cationic interactions result in a 'pseudo-crosslink' forming a hard segment with high glass transition temperature (Tg) [33]. To add mechanical flexibility, the polymer is further modified by introducing low Tg polymer molecules as soft segments. Poly (n-butyl acrylate) (BA), with low glass transition temperature (Tg < -50 °C) [34], is inserted in the middle block 'B' to serve as an elastic strand in the network and to make the polymer membrane stretchable (Fig. 5.1 D). In ethanol, the synthesized polymer exists in colloidal states with an average particle diameter of 96.9 nm (Fig. 5.1 B and Fig. 2.2B). The hydrophilic–lipophilic balance (HLB) value of the hydrophilic 'A' block, calculated based on Davies' method, is 13.03, corresponding to the oil-in-water (O/W) emulsifier range (Table C.1).

To verify the functional roles of the polymer moiety relating to the temperature dependent ion transport, we first characterize the structural components of the as-synthesized block copolymer, using gel permeation chromatography (GPC) and

nuclear magnetic resonance (NMR) measurements (Fig. C.2). The synthesized polymer shows a weight average molecular weight (Mw) of 113,600 g/mole with a dispersity of 1.08. This is similar to the molecular weight of natural pectin, but with a much narrower weight distribution [35]. The monomer feed ratio of the hydrophilic (hard) and hydrophobic (soft) segments is 1:5 (Table C.2 and C.3).

Adding divalent calcium ions into the flexible BTS polymer solution results in a cloudy appearance, revealing a network formation through ionic crosslinks. The crosslinked solution is cast on a plastic sheet and dried to remove the remaining solvent (Fig. 5.2A). During this process, the mixture is monitored in-situ using attenuated total reflectance-fourier transform infrared (ATR-FTIR) spectroscopy, to examine the film formation behavior. The characteristic peaks clearly elucidate structures of the designed polymer (Fig. 5.2 B and Table C.4) and the presence of water contained inside (Fig. C.3). While the solvent evaporates, the neighboring chains of the block copolymer form interpolymer complexes (IPCs) between the AA-HEA functional groups. This interaction between the carbonyl oxygen and hydrogen of the hydroxyl group (hydrogen bonding) is suggested by the thermogravimetric analysis (TGA) profile (Fig. 5.2C) [36]. Here, the IPCs may play a role in aggregating the colloidal particles to form ion transport channels between the interacting 'A' blocks (Fig. 5.1C). At elevated temperatures, the number of ions overcoming the energy barrier increases, which leads to a higher diffusion constant and hopping rate between the coordination sites through the absorption of thermal energy and polymer's segmental motion. Under an applied electric field, the probability of ions moving forward becomes favorable, generating a net current flow through the polymer network.

To interrogate the importance of chemical composition within the 'A' block, series of copolymers with varying ratio of AA to HEA are synthesized (Fig. 5.2D and Table C.6). The polymer film with even proportion of carboxyl-to-hydroxyl groups demonstrates the highest activation energy and temperature response. Modifying this ratio to approximately 1:2, results in a >7-fold decrease in response while films consisting only the carboxyl groups lead to a response depletion. The result reveals that both hydroxyl and carboxyl groups collectively play important roles in chelation of Ca^{2+} and the subsequent formation of the "egg-box" type interactions analogous to the coordination environment in pectin. Moreover, the high temperature response can be explained by the high energy barrier created by strong binding forces between these side chains and calcium ions.
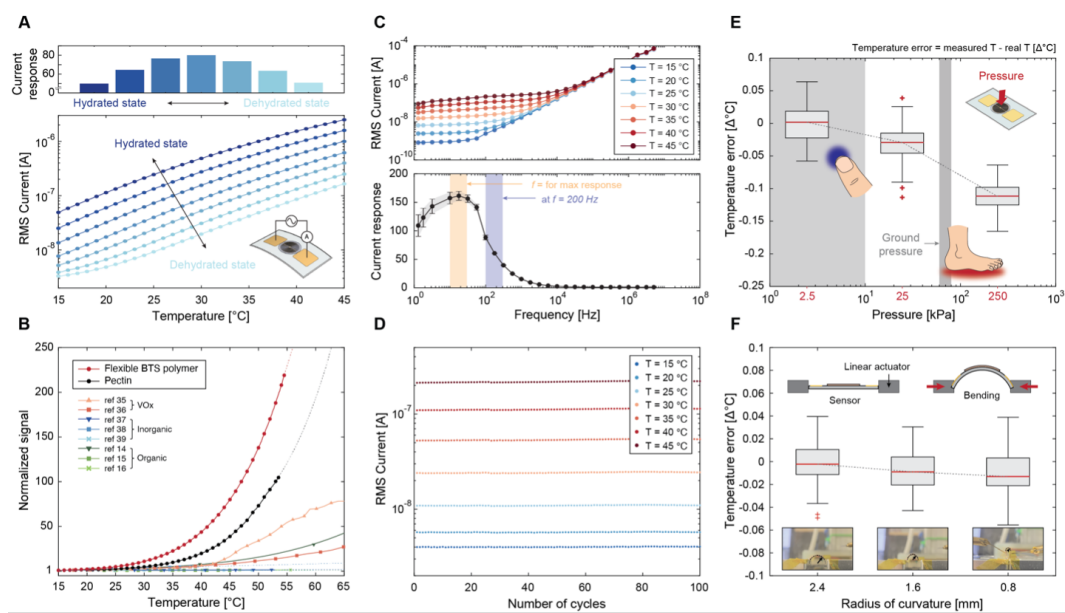
Figure 5.3: Characterization of the flexible BTS polymer sensor. (A) Current variation as a function of temperature, measured between 15 °C and 45 °C with an applied voltage of 300 mV at 200 Hz (bottom) and the corresponding current response calculated at different hydration levels (top). Darker blue lines represent higher hydration, lighter blue lines lower hydration. Inset: Device schematic and configuration for electrical measurement. (B) Response comparison between state-of-art temperature sensing materials and devices, normalized with signals at 15 °C. (C) Frequency dependent current measured between 1 Hz and 5 MHz at varying temperatures (top) and the corresponding current response calculated when 300 mV applied (bottom). Maximum response of 161.3 is obtained at 17.8 Hz. (D) Cyclic stability test over 100 cycles of continuous temperature oscillation between 15 °C and 45 °C. (E) Temperature error extracted from the thermal sensor as a function of normal pressure and (F) bending strain (curvature). All plots represent data from polymer solution crosslinked with 100% concentration of $CaCl_2$.

By varying the concentration of ions, the films are further profiled using TGA-FTIR to verify components from gas-phase diffusion (Figs. C.4 and C.5). The linear relationship ($R^2 = 0.987$) between Ca^{2+} concentration and water in the film indicates that water absorption is mainly caused by metal ions (Fig. 5.2E). Finally, to investigate the conducting species within the polymer matrix, electrochemical impedance spectroscopy analysis is performed. Polymer films with and without Ca^{2+} are prepared and the system's conductivity as a function of AC frequency is measured (Fig. 5.2F). The conductance profile of the film with no metal ions is flat until 10 kHz, whereas the one with Ca^{2+} shows an increase below 100 Hz due to electrode polarization followed by a plateau. This reveals that calcium cations are the major transporting charge carrier of the system.

Characterization of the flexible BTS polymer

To characterize the temperature response, we fabricate an array of circular-shape interdigitated electrodes on a flexible plastic substrate, and drop cast and dry 5 μL of crosslinked BTS polymer solution on the electrodes' surface (Fig. C.6A, B). After mounting the samples on a custom-built thermal cycler, the output current is measured while applying an AC voltage of 300 mV, at 200 Hz. The alternating signals enable stable measurements over time, reducing the possibility of ionic charge depletion caused by DC bias. Here, the 300 mV is chosen based on the minimum level of current (to avoid self-joule heating) that could be stably read from the sensor considering the signal noise floor in room temperature.

The hydration state of organic materials closely correlates to the ionic transport and the material's mechanical properties [37]. To monitor the effect of water in the polymer's performance, we dried the films under various conditions and repeat the measurements (Fig. 5.3 A). When the polymer film is fully hydrated, a relatively low temperature response is observed. In these conditions, conduction through water channels dominates the transport, suppressing the effect of ions, which is mainly responsible for the large temperature dependent impedance changes. As the film is dried, removing unbound water from the chain, the response increases dramatically, indicating growing portion of Ca^{2+} mediated transport [25]. However, further dehydration results in a decreased response, due to loss of conduction paths. A maximum root mean square (RMS) current response ($I_{45°C}/I_{15°C}$) of 80.04 A/A is exhibited over the defined temperature range. Such normalization approach has been adopted to compare between state-of-art thermal sensing materials, characterized under different measurement conditions. By measuring the output current at constant temperature in air, a sensing resolution of less than 8.68 mK is obtained with negligible hysteresis (Fig. C.6 C, D). Compared to the state-of-art thermal sensing materials, including vanadium oxide [38, 39], inorganic devices [40–42], and to natural pectin products [23, 24], the overall temperature response of the resulting flexible BTS polymer composite is orders of magnitude higher. (Fig. 5.3 B).

To evaluate the materials' response as a function of excitation frequency, we measure the samples' impedance spectrum between 1 Hz to 5 MHz, using 300 mV (Fig. 5.3 C). At lower frequencies, in which the transport is mainly induced by ion migration, change of temperature results in a large variation of current. A maximum current response of over 160 A/A is evident around 20 Hz. At frequencies above the charge relaxation, transporting ions within the polymer are not able to follow the alternating

electric field (polarization dominated) and no longer contribute to the temperature dependent conduction behavior.

After conditioning the polymer film to its optimal hydration status, cyclic stability is evaluated by heating the sensor from 15 °C to 45 °C for 6 hours, while monitoring current. Before measurements, a thin layer of parylene-C is conformally coated around the device, to serve as a moisture barrier and electrical insulation. The device shows high stability (Fig. 5.3D, Fig. C.7) with minimum variation in current response, lying within the ±2.39 % fluctuation boundary over 100 cycles of continuous use.

To characterize the effect of mechanical solicitations, the sensors are compressed or bent at different pressures and curvatures. Although a slight decrease in conduction is observed during compression (Fig. C.8), the average temperature error converted from the difference in current read-out, with and without loading, is less than 0.11 °C up to a pressure of 250 kPa (Fig. 5.3 E). This demonstrates that the sensor response is relatively insensitive to strain. Under bending deformations, an even lower temperature error is detected (Fig. 5.3). To test whether the strain insensitivity persists after repetitive mechanical loading, we subject the samples to 100 cycles of bending (bending radius = 1.6 mm) or compression (to a maximum pressure of 25 kPa). The current remains similar to that of the as-fabricated samples, indicating high mechanical stability and elastic recovery. In contrast, dehydrated pectin films are brittle and prone to tear (Fig. 5.1 D).

5.5 Conclusion

The results presented here demonstrate a biomimetic approach to design a thermally responsive polymer for organic electronics. Inspired by the functional motifs in the pectin-Ca^{2+} complex, we create a block copolymer that demonstrates an extremely high thermal response with a sensing resolution of below 10 mK. By utilizing a versatile synthetic procedure, we also show the ability to tailor physicochemical properties that enables optimization of the material's temperature sensitivity and endows mechanical flexibility and stretchability. Additional functionalities can be introduced tailoring the polymer architecture and its side chains, for example, increasing its electrical conductivity, response time, or IR absorption spectrum for diverse thermal sensing platforms. The resulting material is stable under cyclic loading and insensitive to mechanical solicitations, extending its capability and potential use for wearable sensors and consumer electronics. In particular, these

aspects have promise to impact technological advances in the medical or health-care field that can allow continuous and non-invasive personalized monitoring of minute pathophysiological thermal stresses caused by the disruption in homeostasis, infection, inflammatory responses as well as mental stresses or sleep deprivation.

Although our BTS polymer has shown promising results, several challenges and room for improvements remain. Due to its non-linear, exponential response to temperature and hydration dependent sensitivity, a pre-calibration curve needs to be acquired prior to initial measurements and care must be taken during sensor packaging. In addition, an alternative synthesis procedure such as the continuous polymerization method will allow us to reduce batch-to-batch variation and enable mass production. Finally, it will be of interest to further investigate the transport mechanism supplemented by molecular dynamic simulations to further delineate the thermal sensing behavior of the system to potentially improve the material sensitivity, dynamic range, or even the mechanical features by modifying the polymer composition and coordinating metal ions.

Interests on realizing all organic electronic devices with functionalities that its inorganic counterparts cannot provide is on the rise. While many organic electronic components such as substrates, electrodes, and transistors have been developed, advancement and mechanistic understanding of the organic sensory elements have not progressed in parallel. To bridge this gap and to fully optimize the specific features of our flexible BTS polymer, further mechanistic studies accompanied by molecular dynamic simulations to delineate the exact origin of the high thermal response should be followed. We anticipate that our material and design concept can be used for fundamental studies of ion transport mechanisms in the form of such simplified polyelectrolytes, which can be generalized to different ionic conducting polymeric systems.

References

[1] Stephen R. Forrest. The path to ubiquitous and low-cost organic electronic appliances on plastic. *nature*, 428(6986):911–918, 2004.

[2] Anatoliy N. Sokolov, Mark E. Roberts, and Zhenan Bao. Fabrication of low-cost electronic biosensors. *Materials today*, 12(9):12–20, 2009.

[3] Haifeng Ling, Shenghua Liu, Zijian Zheng, and Feng Yan. Organic flexible electronics. *Small Methods*, 2(10):1800070, 2018.

[4] Jiheong Kang, Jeffrey B. H. Tok, and Zhenan Bao. Self-healing soft electronics. *Nature Electronics*, 2(4):144–150, 2019.

[5] Benjamin C. K. Tee, Alex Chortos, Andre Berndt, Amanda Kim Nguyen, Ariane Tom, Allister McGuire, Ziliang Carter Lin, Kevin Tien, Won-Gyu Bae, Huiliang Wang, et al. A skin-inspired organic digital mechanoreceptor. *Science*, 350(6258):313–316, 2015.

[6] Insang You, David G. Mackanic, Naoji Matsuhisa, Jiheong Kang, Jimin Kwon, Levent Beker, Jaewan Mun, Wonjeong Suh, Tae Yeong Kim, Jeffrey B. H. Tok, et al. Artificial multimodal receptors based on ion relaxation dynamics. *Science*, 370(6519):961–965, 2020.

[7] Naixiang Wang, Anneng Yang, Ying Fu, Yuanzhe Li, and Feng Yan. Functionalized organic thin film transistors for biosensing. *Accounts of Chemical Research*, 52(2):277–287, 2019.

[8] Moo Yeol Lee, Hae Rang Lee, Cheol Hee Park, Seul Gi Han, and Joon Hak Oh. Organic transistor-based chemical sensors for wearable bioelectronics. *Accounts of chemical research*, 51(11):2829–2838, 2018.

[9] Tsuyoshi Sekitani and Takao Someya. Stretchable, large-area organic electronics. *Advanced Materials*, 22(20):2228–2246, 2010.

[10] Jiangxin Wang, Meng-Fang Lin, Sangbaek Park, and Pooi See Lee. Deformable conductors for human–machine interface. *Materials Today*, 21(5): 508–526, 2018.

[11] Sihong Wang, Jie Xu, Weichen Wang, Ging-Ji Nathan Wang, Reza Rastak, Francisco Molina-Lopez, Jong Won Chung, Simiao Niu, Vivian R Feig, Jeffery Lopez, et al. Skin electronics from scalable fabrication of an intrinsically stretchable transistor array. *Nature*, 555(7694):83–88, 2018.

[12] Hyo-Ryoung Lim, Hee Seok Kim, Raza Qazi, Young-Tae Kwon, Jae-Woong Jeong, and Woon-Hong Yeo. Advanced soft materials, sensor integrations, and applications of wearable flexible hybrid electronics in healthcare, energy, and environment. *Advanced Materials*, 32(15):1901924, 2020.

[13] Yoon Ho Lee, O Young Kweon, Hongki Kim, Jong Heun Yoo, Seul Gi Han, and Joon Hak Oh. Recent advances in organic sensors for health self-monitoring systems. *Journal of Materials Chemistry C*, 6(32):8569–8612, 2018.

[14] Xiaochen Ren, Ke Pei, Boyu Peng, Zhichao Zhang, Zongrong Wang, Xinyu Wang, and Paddy K. L. Chan. A low-operating-power and flexible active-matrix organic-transistor temperature-sensor array. *Advanced materials*, 28 (24):4832–4838, 2016.

[15] Tran Quang Trung, Subramaniyan Ramasundaram, Byeong-Ung Hwang, and Nae-Eung Lee. An all-elastomeric transparent and stretchable temperature sensor for body-attachable wearable electronics. *Advanced Materials*, 28(3): 502–509, 2016.

[16] Yuki Yamamoto, Shingo Harada, Daisuke Yamamoto, Wataru Honda, Takayuki Arie, Seiji Akita, and Kuniharu Takei. Printed multifunctional flexible device with an integrated motion sensor for health care monitoring. *Science Advances*, 2(11):e1601473, 2016.

[17] Tomoyuki Yokota, Yusuke Inoue, Yuki Terakawa, Jonathan Reeder, Martin Kaltenbrunner, Taylor Ware, Kejia Yang, Kunihiko Mabuchi, Tomohiro Murakawa, Masaki Sekino, et al. Ultraflexible, large-area, physiological temperature sensors for multipoint measurements. *Proceedings of the National Academy of Sciences*, 112(47):14533–14538, 2015.

[18] Hugo Bronstein, Christian B. Nielsen, Bob C. Schroeder, and Iain McCulloch. The role of chemical design in the performance of organic semiconductors. *Nature Reviews Chemistry*, 4(2):66–77, 2020.

[19] Mats Fahlman, Simone Fabiano, Viktor Gueskine, Daniel Simon, Magnus Berggren, and Xavier Crispin. Interfaces in organic electronics. *Nature Reviews Materials*, 4(10):627–650, 2019.

[20] Santosh Mogurampelly, Oleg Borodin, and Venkat Ganesan. Computer simulations of ion transport in polymer electrolyte membranes. *Annual Review of Chemical and Biomolecular Engineering*, 7:349–371, 2016.

[21] Pascal Friederich, Artem Fediai, Simon Kaiser, Manuel Konrad, Nicole Jung, and Wolfgang Wenzel. Toward design of novel materials for organic electronics. *Advanced Materials*, 31(26):1808256, 2019.

[22] Alexis Peaucelle, Siobhan Braybrook, and Herman Höfte. Cell wall mechanics and growth control in plants: the role of pectins revisited. *Frontiers in Plant Science*, 3:121, 2012.

[23] Raffaele Di Giacomo, Chiara Daraio, and Bruno Maresca. Plant nanobionic materials with a giant temperature response mediated by pectin-ca2+. *Proceedings of the National Academy of Sciences*, 112(15):4541–4545, 2015.

[24] Raffaele Di Giacomo, Luca Bonanomi, Vincenzo Costanza, Bruno Maresca, and Chiara Daraio. Biomimetic temperature-sensing layer for artificial skins. *Science Robotics*, 2(3):eaai9251, 2017.

[25] Vincenzo Costanza, Luca Bonanomi, Giovanni Moscato, Linghui Wang, Yeong Suk Choi, and Chiara Daraio. Effect of glycerol on the mechanical and temperature-sensing properties of pectin films. *Applied Physics Letters*, 115(19):193702, 2019.

[26] Gregor T. Grant, Edwin R. Morris, David A. Rees, Peter J. C. Smith, and David Thom. Biological interactions between polysaccharides and divalent cations: the egg-box model. *FEBS letters*, 32(1):195–198, 1973.

[27] David A. Powell, Edwin R. Morris, Michael J. Gidley, and David A. Rees. Conformations and interactions of pectins: Ii. influence of residue sequence on chain association in calcium pectate gels. *Journal of Molecular Biology*, 155(4):517–531, 1982.

[28] Beli R. Thakur, Rakesh K. Singh, Avtar K. Handa, and M. A. Rao. Chemistry and uses of pectin°™a review. *Critical Reviews in Food Science & Nutrition*, 37(1):47–73, 1997.

[29] Krzysztof Matyjaszewski and Jianhui Xia. Atom transfer radical polymerization. *Chemical Reviews*, 101(9):2921–2990, 2001.

[30] Shigeru Yamago. Precision polymer synthesis by degenerative transfer controlled/living radical polymerization using organotellurium, organostibine, and organobismuthine chain-transfer agents. *Chemical Reviews*, 109(11):5051–5068, 2009.

[31] Graeme Moad, Ezio Rizzardo, and San H. Thang. Toward living radical polymerization. *Accounts of Chemical Research*, 41(9):1133–1142, 2008.

[32] Lianqi Cao, Wei Lu, Analucia Mata, Katsuyoshi Nishinari, and Yapeng Fang. Egg-box model-based gelation of alginate and pectin: A review. *Carbohydrate Polymers*, 242:116389, 2020.

[33] Junji Furukawa. A theory of pseudo cross-link: 1. viscosity of polymers in molten states and in concentrated solution. *Polymer Bulletin*, 7:23–30, 1982.

[34] Edmund A. DiMarzio and Julian H. Gibbs. Glass temperature of copolymers. *Journal of Polymer Science*, 40(136):121–131, 1959.

[35] Mohamed Yassine Sayah, Rachida Chabir, Hamid Benyahia, Youssef Rodi Kandri, Fouad Ouazzani Chahdi, Hanan Touzani, and Faouzi Errachidi. Yield, esterification degree and molecular weight evaluation of pectins isolated from orange and grapefruit peels under different conditions. *PloS One*, 11(9): e0161751, 2016.

[36] Grigoriy A. Mun, Vitaliy V. Khutoryanskiy, Gulnara T. Akhmetkalieva, Sergey N. Shmakov, Artem V. Dubolazov, Zauresh S. Nurkeeva, and Kinam Park. Interpolymer complexes of poly (acrylic acid) with poly (2-hydroxyethyl acrylate) in aqueous solutions. *Colloid and Polymer Science*, 283:174–181, 2004.

[37] Joost W. H. Schymkowitz, Frederic Rousseau, Ivo C. Martins, Jesper Ferkinghoff-Borg, Francois Stricher, and Luis Serrano. Prediction of water and metal binding sites and their affinities by using the fold-x force field. *Proceedings of the National Academy of Sciences*, 102(29):10147–10152, 2005.

[38] Bin Wang, Jianjun Lai, Hui Li, Haoming Hu, and Sihai Chen. Nanostructured vanadium oxide thin film with high tcr at room temperature for microbolometer. *Infrared Physics & Technology*, 57:8–13, 2013.

[39] Jun Dai, Xingzhi Wang, Shaowei He, Ying Huang, and Xinjian Yi. Low temperature fabrication of vox thin films for uncooled ir detectors by direct current reactive magnetron sputtering method. *Infrared Physics & Technology*, 51(4):287–291, 2008.

[40] Jaemin Kim, Mincheol Lee, Hyung Joon Shim, Roozbeh Ghaffari, Hye Rim Cho, Donghee Son, Yei Hwan Jung, Min Soh, Changsoon Choi, Sungmook Jung, et al. Stretchable silicon nanoribbon electronics for skin prosthesis. *Nature Communications*, 5(1):5747, 2014.

[41] Jonghwa Park, Marie Kim, Youngoh Lee, Heon Sang Lee, and Hyunhyub Ko. Fingertip skin–inspired microstructured ferroelectric skins discriminate static/dynamic pressure and temperature stimuli. *Science Advances*, 1(9): e1500661, 2015.

[42] R. Chad Webb, Andrew P. Bonifas, Alex Behnaz, Yihui Zhang, Ki Jun Yu, Huanyu Cheng, Mingxing Shi, Zuguang Bian, Zhuangjian Liu, Yun-Soung Kim, et al. Ultrathin conformal devices for precise and continuous thermal characterization of human skin. *Nature Materials*, 12(10):938–944, 2013.

C h a p t e r   6

ION TRANSPORT PHENOMENA IN THERMALLY RESPONSIVE POLYELECTROLYTES

The work presented in this chapter has been adapted from:

- Linghui Wang, Vincenzo Costanza, Nick Higdon, Tae Hyun Kim, and Chiara Daraio. Ion transport phenomena in thermally responsive polyelectrolytes. *Under preparation*, 2023

6.1   Abstract

The understanding of transport phenomena in ion-conducting polyelectrolytes is crucial to enable progress in fields such as organic electronics, sensors, and energy storage and conversion. Recently, a new class of bio- and synthetic polyelectrolytes have gained significant attention due to their exceptional response to temperature changes. Earlier work suggested that the mechanisms responsible for these polyelectrolytes' exquisite temperature response arise from the interaction between the coordination complexes and the crosslinking ions, as well as from the presence of water. Here, we analyze the role of water in the conductivity and temperature response of 2-hydroxyethyl acrylate – acrylic acid (HEA-AA) crosslinked by $CaCl_2$. By combining thermogravimetric analysis (TGA), differential scanning calorimetry (DSC), and Fourier-transform infrared spectroscopy (FTIR), we show how the increase in water content changes the ion mobility without affecting the ions' number density. We analyze different transport phenomena, at a wide range of frequencies and water concentrations, using impedance spectroscopy. Our investigation reveals a strong correlation between the segmental motion of polymer chains and ion transport in HEA-AA, as evidenced by the relationship between DC conductivities and segmental relaxation. Furthermore, we observe a decrease in DC temperature response with increasing water concentration. By analyzing the Arrhenius plot at various water concentrations and applying the Vogel-Tamman-Fulcher (VTF) model, we demonstrate that this reduction in the temperature response mainly originates from the decrease in the glass transition temperature, providing further evidence for the link between ion transport and segmental motion. We note that the effect of water content on the dielectric response of HEA-AA is similar to the effect of temperature

over a broad range of frequencies, despite the fact that the concepts of time-humidity superposition and time-temperature superposition do not apply in our system.

6.2 Introduction

Ion transport in polyelectrolyte has been known to be sensitive to temperature and relative humidity level [1, 2]. Recently, researchers have found ways to leverage this sensitivity to create sensors that are highly responsive [3–6]. These polyelectrolyte-based sensors have several advantages over traditional silicon-based sensors, including good flexibility, solution processability, lightweight, low cost, and biocompatibility [7]. These properties make them particularly well-suited for use in wearable technology, robotics, and prosthetic devices, where flexible and conformal sensing materials that can be produced with a large area are required [8, 9]. Previous research on ion conducting polyelectrolytes focuses mostly on their potential applications in energy storage and actuation, such as lithium-ion batteries and fuel cells [10–12]. A comprehensive examination of the underlying factors affecting the sensing properties of polyelectrolytes is necessary for the advancement of sensor technology. Polyelectrolytes are polymers in which the monomeric unit bears an electrolyte group. The presence of these charged moieties allows polyelectrolytes to solvate ions and support ion transport without the need for a liquid solvent. Even though some polyelectrolytes could conduct solvent-free, for highly charged and therefore highly hydrophilic polyelectrolytes, water vapor adsorption is difficult to avoid. The hydration level of the polymer matrix is sensitive to the environment's relative humidity (RH) and could strongly affect and modify the transport properties of the material [13, 14]. The role of hydration has been extensively studied in polyelectrolyte complex and polyelectrolyte multilayer, where oppositely charged polyelectrolytes crosslink with each other and form a complex [13–15]. However, for metal-ion crosslinked polyelectrolytes, the underlying features of the conduction mechanism are still not well understood. In this paper, we performed a comprehensive study on the transport mechanism and its relationship with the relative humidity level in $CaCl_2$ crosslinked 2-hydroxyethyl acrylate – acrylic acid (HEA-AA), a recent class of polyelectrolytes mimicking the functionality of pectin that has been shown to present outstanding temperature sensing properties [3].

HEA-AA is composed of polar 2-hydroxyethyl acrylate (HEA) groups and acrylic acid (AA) groups, randomly distributed. Together, these functional groups have the ability to bind with metal cations, similar to pectin [3, 16] (fig. 6.1(a)). According to the general model of transport in an ion-conducting medium, the DC conductivity,

σ, is given as the sum of the individual contributions from every conducting species, i:

$$\sigma = \sum_i \sigma_i = \sum_i N_i \mu_i q_i. \qquad (6.1)$$

Here, N_i is the number density of the carriers, μ_i the mobility, and q_i the charge of the i-th conducting species. In our case, besides calcium ions, protons could also disassociate from an acrylic acid monomer and contribute to the overall conductivity.

Water content can affect the conductivity of the polyelectrolyte in multiple ways:

(1) The plasticizing effect is another well-known impact that water may have on polyelectrolyte [17]. Water as a plasticizer could solvate the hydrophilic regions of the polymer backbone and screen the electrostatic interaction between the polymer chains. This screening effect results in an increase in the free volume and an enhancement in the segmental motion of polymer backbones and sidechains. An increase in the chain's segmental motion further facilitates ion transport through co-diffusion [16]. As a result, the ion mobility increases leading to a rise in the ion conductivity (fig. 6.1(b)).

(2) Water might also modify the way calcium ions interact with their coordinating environment. The hydration shell that surrounds the calcium ion, could reduce the electrostatic interaction between the calcium ion and the negatively charged groups on the polymer backbone. This effect could lower the activation energy for ion hopping, enhance segmental motion and also could generate free calcium ions that are solvated in water molecules(fig. 6.1(c)).

(3) Similarly, increasing water content could potentially increase the proton mobility [18] and also boost its number density by assisting proton dissociation from carboxyl groups.

Deconvoluting individual contributions is often not trivial, since multiple mechanisms can superimpose resulting in a single measured quantity, the conductance. In this work, conductances measured are proportional to corresponding conductivities with the same constant of proportionality because the electrode configurations remain always unchanged. Therefore, conductivity σ and conductance G are used interchangeably in the following discussions. In this paper, we first identify the dominant carrier responsible for the thermal response at low humidity levels, by performing controlled experiments. Then, combining the results obtained by gravi-
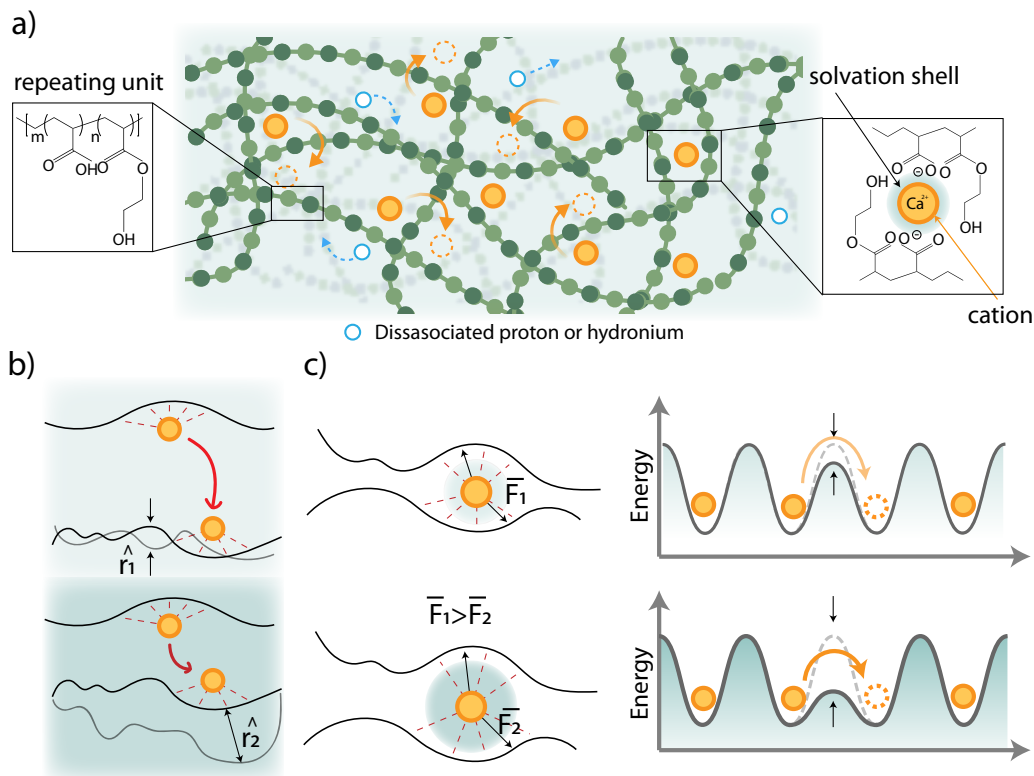
Figure 6.1: Schematic diagrams representing the conduction mechanisms in HEA-AA. (a) Crosslinking mechanism and ion transport in HEA-AA. (b)-(c) Effect of water concentration on the ion environment and the coordination complex.

metric and calorimetric analysis, Fourier-transform infrared spectroscopy (FTIR), impedance spectroscopy, and temperature response as a function of water content, we evaluate the ion transport mechanism and determine the role of water within the polymer matrix.

6.3   Results and discussions

Dominating conducting species at low RH

Before diving into the effect of water on the overall conductivity, we need to first identify the dominant conducting species at low RH. In the $CaCl_2$-HEA-AA system, there are three possible conducting species: (i) chloride ions, (ii) calcium ions, and (iii) protons from the carboxyl groups. It is difficult to separate their contributions to the overall conductivity. However, the dominant conducting species is expected to play the most influential role in the temperature response, at low RH. Therefore, to identify the main charge carrier, we identify the ion species responsible for the temperature sensitivity (as defined in eq. 6.2). To do so, we compared the

temperature response in three different polymer-salt compositions: (a) HEA-AA only, (b) HEA-AA and sodium chloride, and (c) HEA-AA and calcium chloride. In these three systems, the only possible carriers are (a) protons, (b) protons, sodium cations, and chloride anions, and, (c) protons, chloride anions, and calcium cations, respectively. In these three cases, the temperature response (R) will be proportional to the conductivity of the different conducting species:

$$\sum \sigma_a = \sigma_{H^+} \rightarrow R_a = \frac{\sigma_{H^+}(T_2)}{\sigma_{H^+}(T_1)}$$

$$\sum \sigma_b = \sigma_{H^+} + \sigma_{Cl^-} \rightarrow R_b = \frac{\sigma_{H^+}(T_2) + \sigma_{Na^+}(T_2) + \sigma_{Cl^-}(T_2)}{\sigma_{H^+}(T_1) + +\sigma_{Na^+}(T_1) + \sigma_{Cl^-}(T_1)} \quad (6.2)$$

$$\sum \sigma_c = \sigma_{H^+} + \sigma_{Cl^-} + \sigma_{Ca^{2+}} \rightarrow R_c = \frac{\sigma_{H^+}(T_2) + \sigma_{Cl^-}(T_2) + \sigma_{Ca^{2+}(T_2)}}{\sigma_{H^+}(T_1) + \sigma_{Cl^-}(T_1) + \sigma_{Ca^{2+}}(T_1)}$$

with $T_2 > T_1$ being the two temperatures between which the response (R) is calculated. If $R_a \approx R_b \approx R_c$ then $\sigma_{H^+} >> \sigma_{Cl^-}, \sigma_{Ca^{2+}}$. On the other hand, if any R is larger than the others, it follows that the corresponding unique potential carrier is the main contributor to the conductivity. We characterized the temperature responses at RH 5% of (a) HEA-AA, (b) HEA-AA with sodium chloride (NaCl), and (c) HEA-AA with calcium chloride ($CaCl_2$). As shown in Fig. 6.2 (a), by adding NaCl, the temperature response doubled. Nevertheless, adding $CaCl_2$ leads to an almost 9-fold increase in the temperature response. Following our previous reasoning, this result indicates that the calcium ion is the main contributor to the temperature response and the main current carrier. Although the increased response could partly be attributed to the change in glass transition temperature, we assume that the difference in glass transition temperature alone is not large enough to cause this 9-fold increase. To further confirm this result, we performed Density Functional Theory (DFT) calculations, to estimate the binding energy of calcium ions, sodium ions, and protons to the carboxylate group in HEA-AA (Fig. 6.2 (b), Table D.1). A previous study suggested a positive correlation between the binding energy and the thermal response [16]. As expected, a calcium ion shows a larger binding energy to acrylate when compared to a sodium ion or a proton. These results demonstrate that the calcium ions are the dominating contributors to the high-temperature response, and therefore also the main conducting species in the $CaCl_2$-HEA-AA system at low RH.

Effect of water on the macroscopic properties of HEA-AA

Varying the amount of water within the polymer matrix is usually obtained by exposing the sample to a saturated atmosphere at various RH values. In this study,
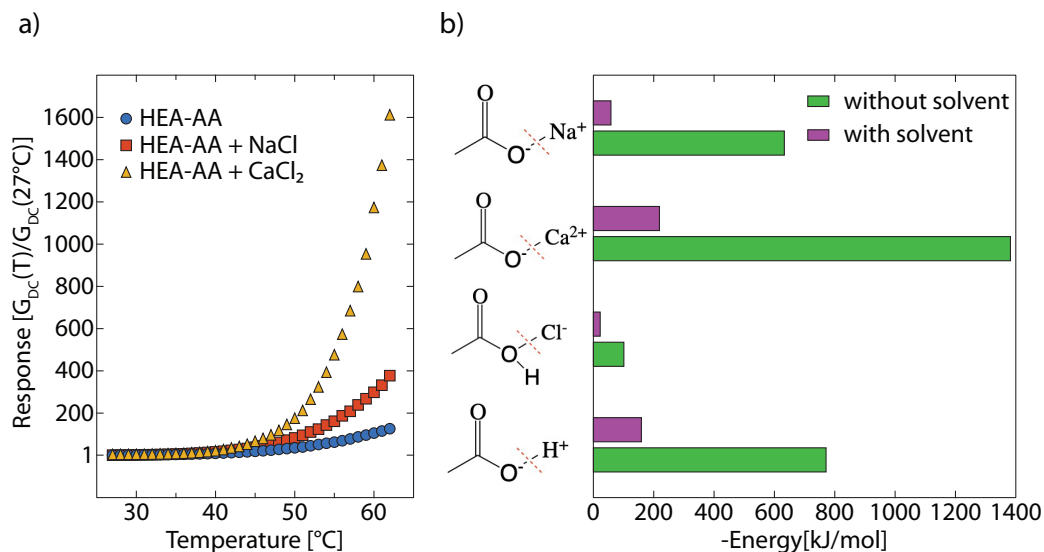
a) b)

Figure 6.2: Dominating conducting species at low RH. (a) Normalized DC conductances of HEA-AA, HEA-AA crosslinked with NaCl, and HEA-AA crosslinked with CaCl$_2$ at a temperature between 27°C and 62°C. Conductivity curves were normalized by the conductivity value at 27°C for temperature response comparison. (b) Binding energies calculated using DFT for proton, calcium ion, and sodium ion. The corresponding chemical equations are as follows from the top of the y-axis: Acetate + Na$^+$ $\rightarrow$ Na$^+$(Acetate), Acetate + Ca^{2+} $\rightarrow$ Ca^{2+}(Acetate), Acetic + Cl$^-$ $\rightarrow$ Cl$^-$(Acetic), Acetate + H$_3$O$^+$ $\rightarrow$ Acetic +H$_2$O. Green bars correspond to the binding energy in a vacuum. The purple bars correspond to the binding energy in solvent water.

we employed a custom-made humidity chamber in order to vary the RH from 5% to 50% in steps of 3%. The water absorption dynamics were evaluated gravimetrically through a precision quartz crystal microbalance. As shown in Figure 6.3(a), an increase in the external RH results in a decrease in the resonance frequency of the quartz, indicating an increase in the resonating mass. In fact, due to the hydrophilic character of the matrix and the presence of hygroscopic calcium cations, the water molecules present in the environment are absorbed both by the polymer backbone and the solvated ions. The dissipation factor of the resonating system similarly increases as a function of RH, suggesting an increase in the viscosity of this visco-elastic polymer. This behavior is further confirmed by the analysis of the glass transition temperature of HEA-AA. Figure 6.3(b) shows the heat flow as a function of temperature as characterized by differential scanning calorimetry (DSC). A hydrated sample was placed in the DSC and cycled between -50 and 100°C under nitrogen purge. Because of the temperature cycling and the dry nitrogen gas, after

every cycle, the remaining free water evaporates (the cycling temperature is not high enough to induce polymer degradation) and the overall water content decreases. As expected, with decreasing water content the glass transition temperature increases (Fig. 6.3(b, inset)). Water acts as a plasticizer in hydrophilic polymers, reducing the electrostatic interchain interactions. Fewer water molecules will favor stronger interchain interactions, less free volume, and weaker polymer segmental motion, leading to a higher glass transition temperature. In addition, lower water concentration will favor stronger coordination interactions between the metal ions and the polymer, which strengthens the crosslinking between polymer chains.

As previously stated, increasing water content could weaken the binding between the calcium ion and the polymer and generate free water-solvated calcium ions. It could also lead to the dissociation of protons from acrylic acid monomers. In order to evaluate these effects on the ions' number density, we performed FTIR at different water contents. Because the protonated carboxyl group and the metal-ion bound (deprotonated) carboxyl group have two distinct absorption peaks at the range between 1500 cm^{-1} and 1850 cm^{-1}, we gauge how the bound calcium ion concentration and proton concentration change with water content, by calculating the corresponding peak areas. Similar to the procedure followed for the DSC experiment, we exposed a dried sample to a saturated humidity environment, then performed FTIR at regular intervals under nitrogen purging, to observe how the spectrum was modified (Fig. 2.6). As time evolves, the area of the peak corresponding to water decreases, confirming the sample is dehydrating. At the same time, the area of the peaks associated with bound Ca^{2+} ions (i.e., the concentration of deprotonated carboxylic acids) and protons (carboxyl group) do not show any significant variation (Fig. 6.3(c)). This implies that the number density of bound calcium ions and protons is not affected by changes in water concentration. The changes induced by water are solely in the ion mobilities. Such effects could be due to the combined role of improved segmental motion and lower binding energy between the ion and the coordination sites. As a result, the bulk conductivity strongly depends on RH (Fig. 6.3(d)): the conductivity increases logarithmically with water content and shows slight saturation for RH above 35%.

Ion Transport

Even though gravimetric, DSC, and FTIR are insightful to probe the dynamic of water absorption in the polymer, and its effect on the polymer matrix, solely they cannot describe water's effect on the electrical conduction and thermal response
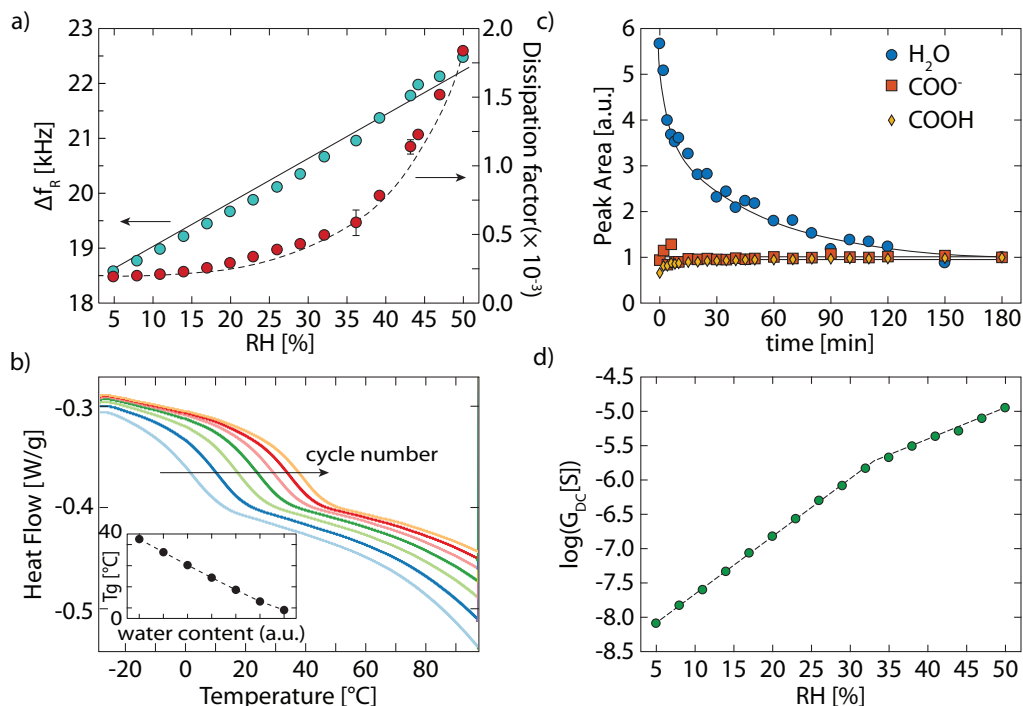
Figure 6.3: Water dependence of the macroscopic properties of HEA-AA. (a) Gravimetric Data as a function of RH. Blue dots shift from the fundamental resonance frequency of the empty cell, red dots dissipation factor of the resonator (for the points at RH 10%, 15%, 20%, 30%, 35%, 40%, 50%, 55% and 60% the error bars are smaller than the data marker). (b) Differential Scanning Calorimetry Data. Light blue, dark blue, light green, dark green, orange, red and yellow correspond respectively to the 1st, 2nd, 3rd, 4th, 5th, 6th and 7th cycle of the DSC run. Inset represents the calculated glass transition temperature as a function of water content (cycle number). (c) FTIR Data. (d) DC Conductance as a function of RH as calculated with the CTRW model.

phenomena of HEA-AA. A very powerful tool to probe different conductivity dynamics in polymer electrolytes is dielectric spectroscopy, in which the samples' conductance and susceptance are measured as a function of the excitation frequency of the applied electric field. Figure 6.4(a) shows a representative spectrum of the real conductance as a function of the excitation frequency. Three different regions can be observed: (i) at low frequencies a dispersive regime caused by the build-up of oppositely charged ions at the interface of the blocking electrode; (ii) a medium frequency region where the conductance is independent of the excitation frequency. This conductance is the DC conductance because in this region ions diffuse as if they are in the infinite medium; (iii) a high-frequency dispersive region where the real part of the conductivity starts to increase again. This phenomenon can be attributed to different relaxations: the α-relaxation, which is attributed to the segmental motion of polymer backbone and the sub-segmental β-relaxation, which occurs at a

shorter time scale than the α-relaxation. The specific origin of the β-relaxation is still unclear, but it is commonly associated with the rotational motion of side groups and the cage-rattling effect [19–21]. Similar conclusions can be drawn by looking at the permittivity loss spectrum derived by the conductance: in region (i) an apparent relaxation peak appears due to the electrode polarization; region (ii) shows a slope of -1 indicating long-range transport of the ions; region (iii) includes multiple relaxation processes with one not fully formed at a higher frequency. In order to measure the influence of water content on the impedance spectrum, we recorded the dielectric loss as a function of RH (Fig. 6.4(b)). For increasing RH, the spectra move up and shift to the right, indicating that the increase in water content increases the absolute conductance and accelerates the conduction processes. Moreover, as frequently reported for temperature, the effect of RH on the high-frequency part of the spectra is limited if not absent. For low RH (below 29%) only the diffusive and dispersive regions are visible. Dehydration decreases the ion mobility, resulting in longer diffusion times for the ions, they therefore do not have time to travel to the electrode and form an ionic interface. Above RH 29%, the lower frequency electrode polarization region starts to appear.

To further quantify the effect of hydration on the DC conductivity and segmental relaxation, we fitted the (ii) and (iii) regions to the complex dielectric function with the following equation (fig. 6.4(c)):

$$\epsilon(\omega) = \frac{G_{DC}}{i\omega\epsilon_0} + \frac{\Delta\epsilon_\alpha}{(1 + (i\omega\tau_\alpha)^{a_\alpha})^{b_\alpha}} + \frac{\Delta\epsilon_\beta}{1 + (i\omega\tau_\beta)^{a_\beta}} + \epsilon_\infty \tag{6.3}$$

where G_{DC} corresponds to the DC conductance, ϵ_∞ denotes the $\epsilon'(\omega)$ at the high-frequency limit. $\Delta\epsilon_i$ and τ_i, describe the dielectric relaxations strengths and time constant of corresponding dielectric relaxation, where i = α, β. a_α , b_α and a_β are the shape parameters. a and b represent the symmetric and unsymmetric broadening of the dielectric relaxation respectively [21]. Since the second dielectric relaxation is not fully captured in the measured frequency range, only one shape parameter is used to avoid redundancy. The peak frequency ν_{max} of the dielectric loss ϵ' of the α-relaxation is usually used to represent the characteristic frequency of the segmental motion and can be obtained from the following relationship [19, 20]:

$$\nu_{max} = \frac{1}{\tau_\alpha} \left(\sin \frac{a\pi}{2 + 2b} \right)^{1/a} \left(\sin \frac{ab\pi}{2 + 2b} \right)^{-1/a} \tag{6.4}$$

Figure 6.4(d) shows the dependence of $\log(G_{DC})$ and $\log(\nu_{max})$ on RH ranging from 5% to 50%. First, we observed that both G_{DC} and ν_{max} increase with hydration

and start to plateau at high RH as expected. Secondly, a high correlation between $\log(G_{DC})$ and $\log(\nu_{max})$ was observed with the Pearson correlation coefficient being 0.99. This suggests that the ion transport mechanism can be strongly coupled with the segmental motion, which has been observed in other ionomers with plasticizers [22].
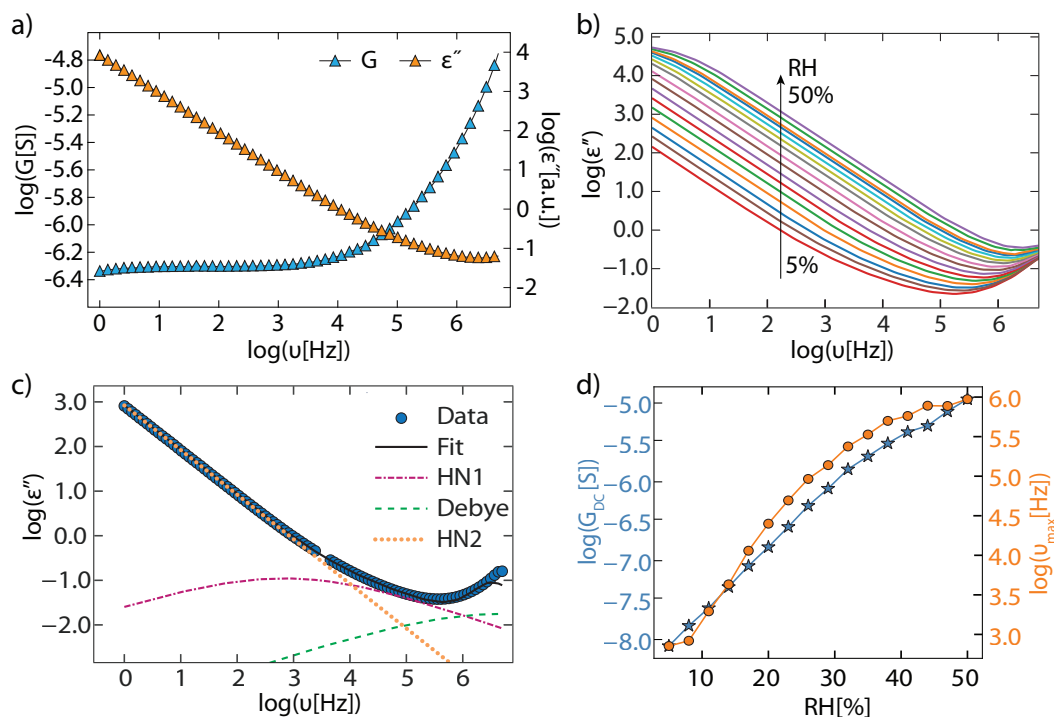

Figure 6.4: Water Dependence of Dielectric Spectra. (a) Typical conductance and dielectric spectrum. Blue triangles represent the conductance, while the yellow triangles represent the dielectric loss for a sample at RH 35%. For clarity, markers are a subgroup of the data points. (b) Dielectric loss spectra as a function of RH. (c) Model fitting. The blue dots represent the dielectric loss spectrum of a sample at RH 14%. The red dotted-dashed line and the green dashed line correspond to the α-relaxation and the β-relaxation, both modeled by the HN equation. The yellow dotted line represents DC conduction, while the black line corresponds to the overall fitting. (d) DC conductance and the characteristic segmental relaxation frequency as a function of different RH (between 5% and 50%).

Relationship between temperature response and glass transition temperature

To further investigate the correlation between ion conductivity and polymer segmental motion, we studied the dependence of its dielectric response on temperature. In addition, the correlation between water content and calcium ion transport in the system has important implications for the temperature response of this material. Previous work on pectin has indicated that an increase in the water content degrades

the temperature response of the polymer [23]. Similar results have been observed for the block copolymer that mimics pectin's structure [3]. In this latter work, however, a response degradation has also been measured for water content below a certain threshold. This is unexpected because a lower water content should increase the activation energy, and thus leads to a higher temperature response. The same behavior is expected in the related copolymer in this paper. As presented in figure 6.4(b), the increase in RH has the effect of shifting up and right the conductance spectra. A similar effect is expected when changing the temperature of the sample. Figure 6.5(a) shows the result of an isochronical impedance spectra taken at constant RH (20%) for different temperatures (42 and 60 °C). Even though the analysis of the conduction mechanism as a function of temperature will be left to a sequent paper, it is important to notice that, depending on the temperature, some spectra will show only the dispersive and diffusive regions, while others will also present the polarization of the electrodes, in the same frequency range. This leads to a dependence of the temperature response on the excitation frequency. Four regions can be observed: (i) one at a lower frequency where the spectrum at lower temperature does not show a fully developed electrode polarization while the one at higher temperature does; (ii) a low medium frequency region where both the spectra are in the diffusive regime; (iii) a high medium frequency region where the spectrum at a lower temperature is already in the dispersive regime while the higher temperature spectrum is still in the diffusive region, and (iv) a high-frequency region where both spectra present dispersive behavior. In region (i), the presence of the electrode polarization affects the effective conductivity, modifying the response. In region (ii) we can describe the temperature effect on the ion conduction since both the curves are in the diffusive regime. We will consider this region to calculate the bulk response R_{DC}. When transitioning to the region (iii) the response drops once more since one of the spectra shows increased conductivity as a result of the dispersive regime. Region (iv) follows a common trend of ion conductors near constant loss behavior with a weak dependence on temperature. The combination of these behaviors in different parts of the spectrum results in a dependence of the temperature response on the external frequency. The frequency at which the transition from regions (i) to (iv) can be observed, however, is a function of the water content. Figure 6.5(b) shows the impact of different RH on the response spectra, illustrating how for increasing RH the characteristic transition frequencies shift to the right. This behavior can explain the decrease of response below a certain water content when measuring at a single frequency. Initially, the excitation frequency falls in the region (ii); as the

water content decreases the transition frequency between region (ii) and (iii) shifts to the higher frequencies, and eventually, the excitation frequency falls in region (iii). This reasoning could also be applied to explain the decrease in response as the water content increase, resulting in an apparent lowering in the response. Nonetheless, Figure 6.5(c) shows that the DC response spectra for different RH decrease with humidity. This is a result of a lowering in ion-hopping energy barriers with hydration.
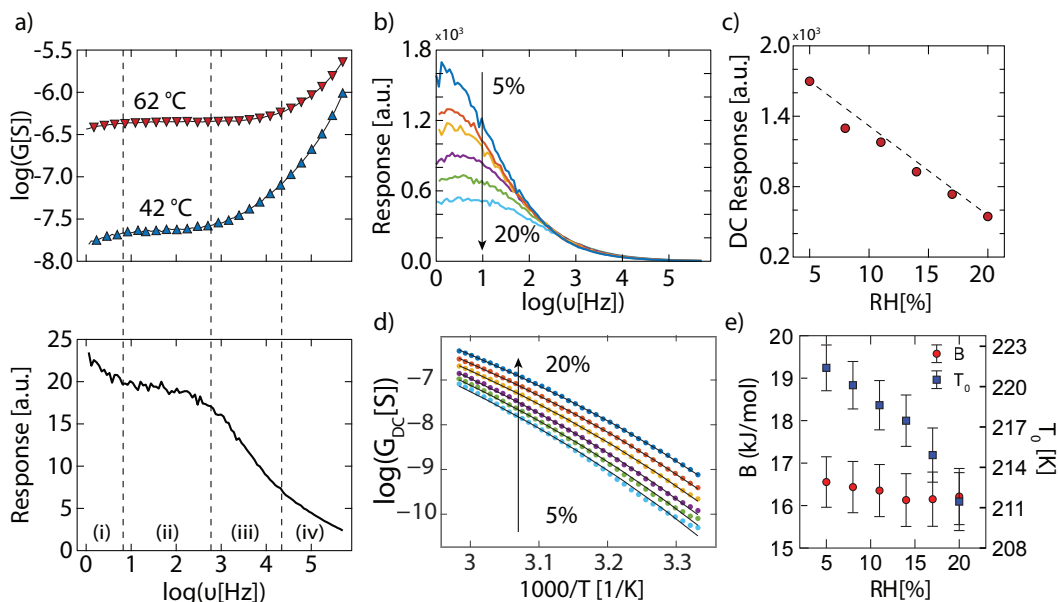

Figure 6.5: Effect of water content on HEA-AA temperature response. Dielectric Spectra as a function of temperature (top) measured at RH 20%. Blue triangles represent the conductance spectrum measured at 315.15 K, while the red triangles represent the conductance spectrum measured at 338.15 K. For clarity, markers are a subgroup of the data points. Corresponding temperature response spectra (bottom). The black line represents the conductance temperature response as a function of the frequency measured at 20% RH. The dashed lines indicate the four different regimes of the response. (b) Response spectra for different RH. Light blue, green, purple yellow, orange, and dark blue correspond respectively to 20%, 17%, 14%, 11%, 8%, and 5% RH. (c) DC temperature response was calculated from the response spectra. (d) Arrhenius plot of data (dots) and the VFT fits (black curves) for the different humidity values. Light blue, green, purple yellow, orange, and dark blue correspond respectively to 20%, 17%, 14%, 11%, 8%, and 5% RH. (e) VTF fitting parameter T_0 and B as a function of humidity.G_0 is set to be constant for varying RH.

To further analyze the effect of water on the temperature dependence of the conductivity, we extracted the Arrhenius plot for different humidity (5% to 20%). In this case, we do not observe a linear relationship in the Arrhenius plot, indicating that the ion transport is coupled with the segmental motion of the polymer (Fig. 6.5(d)). The

conductance G in this scenario is often described by the Vogel–Fulcher–Tammann (VTF) model:

$$G = G_0 \exp\left(-\frac{B}{T - T_0}\right) \tag{6.5}$$

where B and T_0 are fitting parameters. In particular, B is the pseudo-activation energy and T_0 has been empirically found to be 50K lower than the glass transition temperature T_g in polymer electrolytes [24]. The pre-exponential factor G_0 is dependent on the number of charge carriers. In this study, it was kept constant across all RH levels as no significant changes in ion concentration were observed during hydration. During the fitting of the experimental data with the VTF equation, we observe B is relatively constant compared to $k_B T$ for all RH, and changes in T_0 contributed to most of the difference in the temperature dependence at various RH (Fig. 6.5 (e)). In fact, all the VTF curves can be collapsed onto a master curve with shifted temperature(Fig. 6.6 (a)). The shift factor T_0^* for each RH is calculated by keeping B and G_0 constant and only allowing T_0^* to vary during the VFT fitting. T_0^* deviates only slightly from T_0 . As a result, the DC conductivity of HEA-AA can be expressed as:

$$\sigma(T, RH) = \sigma(T - T_0^*) = \sigma_0 \exp\left(-\frac{B}{T - T_0^*}\right), \quad T_0^* = T_0^*(RH) \tag{6.6}$$

This indicates that the drop in DC temperature response and the increase in DC conductivity with hydration can be contributed to decrease in T_0^*, which is related to the glass transition temperature. This further suggests that segmental motion is coupled with the calcium ion transport in HEA-AA. Furthermore, the impedance spectra with similar $T - T_0^*$ overlap across the measured frequency range, strongly suggesting that humidity and temperature affect ion transport and dielectric relaxation via the same mechanism(Fig. 6.6 (b)). Similar temperature-humidity superposition over a large frequency range has only been reported in the polyelectrolyte complexes with dynamic modulus, where both temperature and water affect the polymer chain mobility through a hydrogen bonding mechanism [25].

6.4 Conclusions

In this work, we investigated the effect of water on the transport phenomena in a single ion conductor polymer composed of HEA-AA and calcium ions. We showed that at low RH calcium ions are the dominant carrier and main contributor to the thermal response. Using IR spectroscopy, we discovered that the water
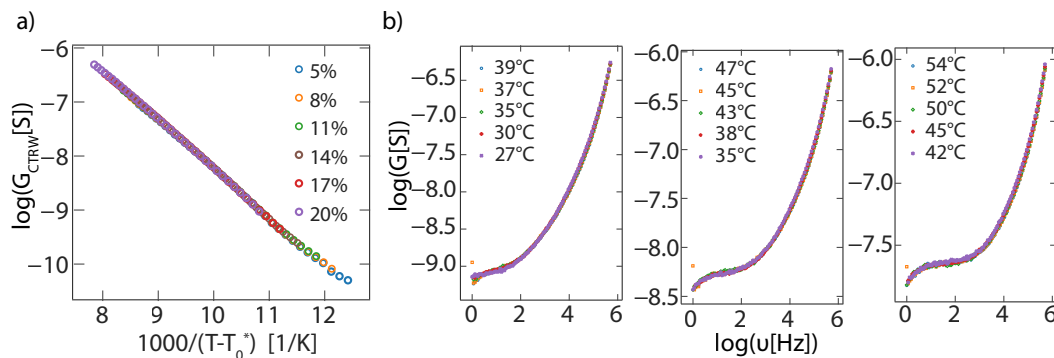
Figure 6.6: Equivalent effects of water and temperature. (a)Data in figure 6.5(d) plotted with temperature shifted by corresponding T_0^* (b) Impedance spectra were taken at similar $T - T_0^*$ values. The $T - T_0^*$ values of spectra plotted in three figures are: 92.45 ± 0.07 K, 100.45 ± 0.07 K and 107.45 ± 0.07 K from left to right. Colors correspond to RHs (same as (a)): blue (5%), yellow(7%), green(11%), red(17%), and purple(20%).

content does not modify the number density of the conducting ions. The humidity-dependent behavior of conductivity predominantly stems from the variation in ion mobility. The relationship between DC conductivity and segmental relaxation frequency suggests a strong coupling between ion transport and polymer segmental motion. This observation was further supported by the fact that the dependence of DC temperature response on RH can be largely attributed to the change in glass transition temperature with RH. Remarkably, for the range of RH and temperature investigated in this paper, we have demonstrated that both water and temperature exert comparable influences on dielectric spectra. This similar impact suggests that both factors operate through similar mechanisms to affect ion transport.

References

[1] Mozhdeh Noorkami, James B. Robinson, Quentin Meyer, Oluwamayowa A. Obeisun, Eric S. Fraga, Tobias Reisch, Paul R. Shearing, and Daniel J. L. Brett. Effect of temperature uncertainty on polymer electrolyte fuel cell performance. *international Journal of Hydrogen Energy*, 39(3):1439–1448, 2014.

[2] Jianlu Zhang, Yanghua Tang, Chaojie Song, Zetao Xia, Hui Li, Haijiang Wang, and Jiujun Zhang. Pem fuel cell relative humidity (rh) and its effect on performance at high temperatures. *Electrochimica Acta*, 53(16):5315–5321, 2008.

[3] Tae Hyun Kim, Zhun Zhou, Yeong Suk Choi, Vincenzo Costanza, Linghui Wang, Joong Hwan Bahng, Nicholas J Higdon, Youngjun Yun, Hyunbum Kang, Sunghan Kim, and Chiara Daraio. Flexible biomimetic block copolymer composite for temperature and long-wave infrared sensing. *Science Advances*, 9(6):eade0423, 2023.

[4] Gang Ge, Yao Lu, Xinyu Qu, Wen Zhao, Yanfang Ren, Wenjun Wang, Qian Wang, Wei Huang, and Xiaochen Dong. Muscle-inspired self-healing hydrogels for strain and temperature sensor. *ACS Nano*, 14(1):218–228, 2019.

[5] Ran An, Xiaoyu Zhang, Linglin Han, Xiangdong Wang, Yulin Zhang, Lingying Shi, and Rong Ran. Healing, flexible, high thermal sensitive dual-network ionic conductive hydrogels for 3d linear temperature sensor. *Materials Science and Engineering: C*, 107:110310, 2020.

[6] Giuseppe Casalbore-Miceli, Mujie Yang, Yang Li, Alberto Zanelli, Alessandro Martelli, S Chen, Yong She, and Nadia Camaioni. A polyelectrolyte as humidity sensing material: Influence of the preparation parameters on its sensing property. *Sensors and Actuators B: Chemical*, 114(2):584–590, 2006.

[7] Hyun Woo Song, Wonbin Choi, Taesu Jeon, and Joon Hak Oh. Recent advances in smart organic sensors for environmental monitoring systems. *ACS Applied Electronic Materials*, 2022.

[8] Mengjia Zhu, Shantonu Biswas, Stejara Iulia Dinulescu, Nikolas Kastor, Elliot Wright Hawkes, and Yon Visell. Soft, wearable robotics and haptics: Technologies, trends, and emerging applications. *Proceedings of the IEEE*, 110(2):246–272, 2022.

[9] Jun Chang Yang, Jaewan Mun, Se Young Kwon, Seongjun Park, Zhenan Bao, and Steve Park. Electronic skin: Recent progress and future prospects for skin-attachable devices for health monitoring, robotics, and prosthetics. *Advanced Materials*, 31(48):1904765, 2019.

[10] Liping Yue, Jun Ma, Jianjun Zhang, Jingwen Zhao, Shanmu Dong, Zhihong Liu, Guanglei Cui, and Liquan Chen. All solid-state polymer electrolytes for

high-performance lithium ion batteries. *Energy Storage Materials*, 5:139–164, 2016.

[11] Anil Arya and AL Sharma. Polymer electrolytes for lithium ion batteries: A critical study. *Ionics*, 23(3):497–540, 2017.

[12] Kenneth A. Mauritz and Robert B. Moore. State of understanding of nafion. *Chemical Reviews*, 104(10):4535–4586, 2004.

[13] Cornelia Cramer, Souvik De, and Monika Schönhoff. Time-humidity-superposition principle in electrical conductivity spectra of ion-conducting polymers. *Physical Review Letters*, 107(2):028301, 2011.

[14] Hyosung An, Touseef Habib, Smit Shah, Huili Gao, Anish Patel, Ian Echols, Xiaofei Zhao, Miladin Radovic, Micah J Green, and Jodie L Lutkenhaus. Water sorption in mxene/polyelectrolyte multilayers for ultrafast humidity sensing. *ACS Applied Nano Materials*, 2(2):948–955, 2019.

[15] Souvik De, Cornelia Cramer, and Monika Schonhoff. Humidity dependence of the ionic conductivity of polyelectrolyte complexes. *Macromolecules*, 44 (22):8936–8943, 2011.

[16] Linghui Wang, Tae Hyun Kim, Vincenzo Costanza, Nick Higdon, and Chiara Daraio. Ion transport in thermal responsive pectin film. *Submitted*.

[17] RM Hodge, TJ Bastow, GH Edward, GP Simon, and AJ Hill. Free volume and the mechanism of plasticization in water-swollen poly (vinyl alcohol). *Macromolecules*, 29(25):8137–8143, 1996.

[18] P Commer, AG Cherstvy, E Spohr, and AA Kornyshev. The effect of water content on proton transport in polymer electrolyte membranes. *fuel cells*, 2 (3-4):127–136, 2002.

[19] Gregory J Tudryn, Michael V O'Reilly, Shichen Dou, Daniel R King, Karen I Winey, James Runt, and Ralph H Colby. Molecular mobility and cation conduction in polyether–ester–sulfonate copolymer ionomers. *Macromolecules*, 45(9):3962–3973, 2012.

[20] Ivan Popov, Shiwang Cheng, and Alexei P Sokolov. Broadband dielectric spectroscopy and its application in polymeric materials. *Macromolecular Engineering: From Precise Synthesis to Macroscopic Materials and Applications*, pages 1–39, 2022.

[21] Friedrich Kremer and Andreas Schönhals. *Broadband dielectric spectroscopy*. Springer Science & Business Media, 2002.

[22] Shihai Zhang, Shichen Dou, Ralph H. Colby, and James Runt. Glass transition and ionic conduction in plasticized and doped ionomers. *Journal of Non-crystalline Solids*, 351(33-36):2825–2830, 2005.

[23] Vincenzo Costanza, Luca Bonanomi, Giovanni Moscato, Linghui Wang, Yeong Suk Choi, and Chiara Daraio. Effect of glycerol on the mechanical and temperature-sensing properties of pectin films. *Applied Physics Letters*, 115(19):193702, 2019.

[24] Kyle M. Diederichsen, Hilda G. Buss, and Bryan D. McCloskey. The compensation effect in the Vogel–Tammann–Fulcher (VTF) equation for polymer-based electrolytes. *Macromolecules*, 50(10):3831–3840, 2017.

[25] Pilar C Suarez-Martinez, Piotr Batys, Maria Sammalkorpi, and Jodie L Lutkenhaus. Time–temperature and time–water superposition principles applied to poly (allylamine)/poly (acrylic acid) complexes. *Macromolecules*, 52(8):3066–3074, 2019.

Chapter 7

CONCLUSIONS

7.1   Summary and conclusions

This thesis presented a study on ion transport in temperature sensitive polyelectrolytes. We first used pectin, an ion-conductive biopolymer with high temperature sensitivity, as an example. We studied the principles governing ion transport and analyzed the molecular origin of its thermal sensitivity. From our examination of pectin, we proposed a new direction for thermally response material development and designed a flexible biomimetic synthetic polymer that outperforms state-of-art temperature sensing material.

Chapter 2 outlined the sample fabrication process and measurement setups. Also, it described the key methods used to study ion transport in thermally responsive polymers in this thesis, including the basis of impedance spectroscopy and models used for impedance spectra analysis. In Chapter 3, we studied ion transport in dehydrated crosslinked pectin, where metal ions were found to be the main charge carriers. The research showed that the elevated ionic conductivity at high temperatures was caused by improved ion mobility, rather than an increase in ion number density. By studying pectin crosslinked with nine different multivalent cations, we revealed that the high temperature response is related to the strong binding between metal ions and pectin. Density functional theory simulations further suggested that carboxyl and hydroxyl groups can play an important role in creating a strong metal ion-pectin binding. Chapter 4 explored the impact of humidity on ion transport in crosslinked pectin. The impedance spectrums analysis showed that hydration improves ion mobility by reducing the activation energy for ion hopping, thus explaining the decreased temperature response in hydrated pectin. We showed that there is a trade-off between conductivity and temperature response with varying water content. In Chapter 5, we presented a flexible block biomimetic copolymer with A block (HEA-AA) containing carboxyl and hydroxyl groups and B block (BA) consisting of flexible poly (n-butyl acrylate) with a high thermal response outperforming other organic thermally sensitive material. We optimized its temperature response with respect to the ratio of carboxyl-to-hydroxyl groups in the A block. Compared to crosslinked pectin, it showed a superior thermal response and

mechanical flexibility. On the other hand, similar to pectin, its temperature response and ionic conductivity were shown to be sensitive to humidity. In Chapter 6, we conducted a systematic examination of the impact of water content on ion transport and thoroughly analyzed its frequency response under varying humidity and temperature conditions. Combining results from gravimetric measurements, infrared spectroscopy, and differential scanning calorimetry at various humidity levels, we showed that water enhances segmental motion and ion mobility in HEA-AA. Also, we found that humidity and temperature affect ion transport and dielectric relaxation in a similar way. As such, it is not possible to decorrelate these two factors through AC electrical measurements.

7.2   Future outlook

This thesis provided a comprehensive examination of ion transport in thermally sensitive polymer electrolytes. However, there are many areas for further exploration in order to fully realize its potential.

s

Optimization of the temperature sensitive polymer

For temperature sensing applications, polymer electrolyte with high ionic conductivity, high thermal sensitivity, and stability is preferred. These properties could be further optimized by exploring the effect of salt concentrations, types of salts, and monomer types. The effect of salt concentration has been studied widely in lithium-polymer electrolyte systems. Ionic conductivity shows a nonmonotonic dependence on the concentration due to its opposite effect on mobility and number density [1]. With higher concentrations, the number density of the current carrier increases. However, at high ion concentrations, the effective number density would be lowered by the formation of ion pairs and ion clusters. In addition, ion-polymer interaction increases the local friction of the polymer chain and can significantly slow down the polymer segmental relaxation, leading to a higher viscosity and glass transition temperature [2]. As a result, the ion diffusion coefficient decreases rapidly with increasing salt concentration. Combining these two effects, ion conductivity exhibits an initial increase followed by a decline with increasing ion concentration. Therefore, the ion conductivity can be further tuned and optimized by doping the polymer with different ion concentrations. On the other hand, the temperature sensitivity will also be affected by ion concentrations partially due to its effect on glass transition temperature [3]. In addition to ion concentration, other types of cation,

such as copper ions and cobalt ions, and other monomer chemical structures, such as 2,3-dihydroxypropyl acrylate, 1,3- dihydroxypropyl acrylate, can also be explored. As shown in Chapter 3, the temperature sensitivity is positively correlated with the binding energy between metal cations and the polymer. DFT simulation could be employed to screen for chemical groups and ion types with high binding energy.

Decorrelation of the effect of humidity from temperature

Similar to other organic electronics, insulation against humidity is one of the main challenges in thermal sensor fabrication based on ion conductive polymers. As pointed out in Chapter 6, humidity and temperature have a similar effect on ion transport in the frequency range we explored. For it to be used as a thermal sensing material, water content needs to be kept constant to ensure a stable and reliable temperature reading. Therefore a water vapor barrier is needed. For traditional organic electronics, such as OLED displays, the organic active material is sealed using glass or metal lids with sealant. Desiccants such as calcium and barium can also be added to absorb extra moisture. Although low gas permeability could be achieved with this method, the encapsulated device is rigid and bulky. For applications that require flexibility, alternative methods such as thin-film barriers can be used. In Chapter 5, we demonstrated that parylene film coating provides good insulation against water vapor during temperature cycling between 15 °C and 45 °C. However, it does not perform well enough for higher temperatures and high RH. Other encapsulation strategies such as inorganic-organic multilayer could be tried, which has been reported to provide superior stability for organic photovoltaics [4]. One caveat is that a minimum amount of water content is needed for ions to conduct. Long-time exposure to a vacuum during the barrier material deposition would render the sample unconducive. Therefore, atmospheric pressure deposition would be preferred. Additionally, to mitigate the impact of dehydration, polar solvents with higher boiling points can be used to replace water, such as DMSO or oligomers of corresponding polymers. Overall, the hydrophilic nature of temperature-sensitive polymer electrolytes necessitates the development of an effective water-vapor barrier for their practical application.

References

[1] Chang Yun Son and Zhen-Gang Wang. Ion transport in small-molecule and polymer electrolytes. *The Journal of Chemical Physics*, 153(10):100903, 2020.

[2] Shihai Zhang, Shichen Dou, Ralph H Colby, and James Runt. Glass transition and ionic conduction in plasticized and doped ionomers. *Journal of Non-crystalline Solids*, 351(33-36):2825–2830, 2005.

[3] Nicolaas A. Stolwijk, Christian Heddier, Manuel Reschke, Manfred Wiencierz, Joachim Bokeloh, and Gerhard Wilde. Salt-concentration dependence of the glass transition temperature in PEO–NaI and PEO–LiTFSI polymer electrolytes. *Macromolecules*, 46(21):8580–8588, 2013.

[4] Luke J. Sutherland, Hasitha C. Weerasinghe, and George P. Simon. A review on emerging barrier materials and encapsulation strategies for flexible perovskite and organic photovoltaics. *Advanced Energy Materials*, 11(34):2101383, 2021.

A p p e n d i x   A

SUPPORTING MATERIALS FOR CHAPTER 3

The work presented in this chapter has been adapted from:

- Linghui Wang, Tae Hyun Kim, Vincenzo Costanza, Nick Higdon, and Chiara Daraio. Ion transport in thermal responsive pectin film. *Submitted to Applied Physics Letters*, 2023

Electrode Fabrication

To fabricate the electrodes for conductivity measurements, polyimide (PI) resin was first coated on a 2-inch silicon wafer at a thickness of 5 μm and fully cured. Next, a layer of photoresist (PR) was spin-coated and patterned using a standard photolithography process, followed by Ti/Au deposition (200/1000 Å, CHA Mark 40 electron beam evaporator) and lift off to expose the electrode design. Finally, to remove the remaining PR residue, the surface of the wafer was treated with O_2 plasma (Plasma-Therm SLR 720). Each interdigitated electrode (2.5x2.5 mm, 30 μm wide with 20 μm spacing) was diced and inspected under the microscope before use.

ORCA input file

A sample input file for DFT frequency calculation is shown below:

```
! RKS B3LYP def2-TZVP def2/J Opt Freq RIJCOSX TIGHTSCF Grid7 NoFinal-
Grid GridX9 NoFinalGridX
! SlowConv PrintBasis Largeprint
%scf
MaxIter 10000
Shift Shift 0.5 ErrOff 0.1 end end
%pal
nprocs 12 end
%geom
maxiter 600
end
%maxcore 12000
```

* xyzfile 1 1 structure.xyz

Electrical Measurements

For electrical measurements, we used gold interdigitated electrodes fabricated using methods described above. 100 mV was applied and current was measured using a Keithley 2636 SYSTEM SourceMeter. To measure the temperature response, a Peltier element and a thermal camera (FLIR) were used to control the temperature. Thermal cycles run between 18°C and 47°C for 2 hours (Fig. A.1). We took only the equilibrated cycles for the subsequent analysis. The temperature response was calculated by dividing the averaged current at 45°C by the averaged current at 20 °C. For each type of metal ions, at least 3 samples were fabricated and measured. Means and standard deviations were calculated for their responses and activation energies. Because we used planar interdigitated electrodes for the measurement, the conductivity is difficult to obtain. However, since the electrode configuration is consistent in our study, the ratios between conductance and conductivity for all the measurements would be the same.
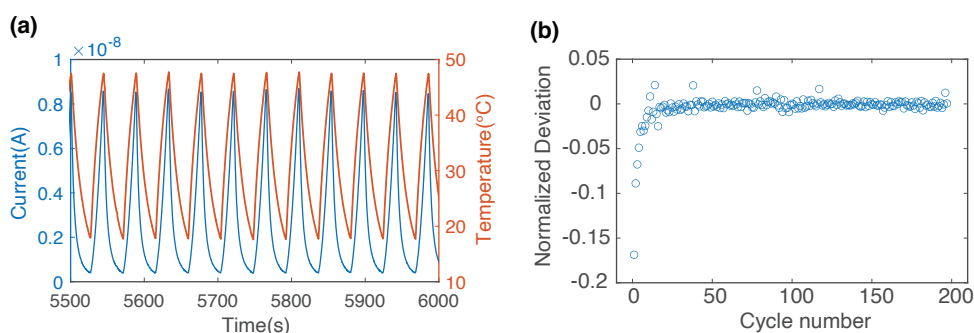
Figure A.1: Characterization of the Temperature Response. (a) A snapshot of measured electrical current with temperature variations. (b) The averaged normalized standard deviation of current between adjacent cycles versus cycle number.
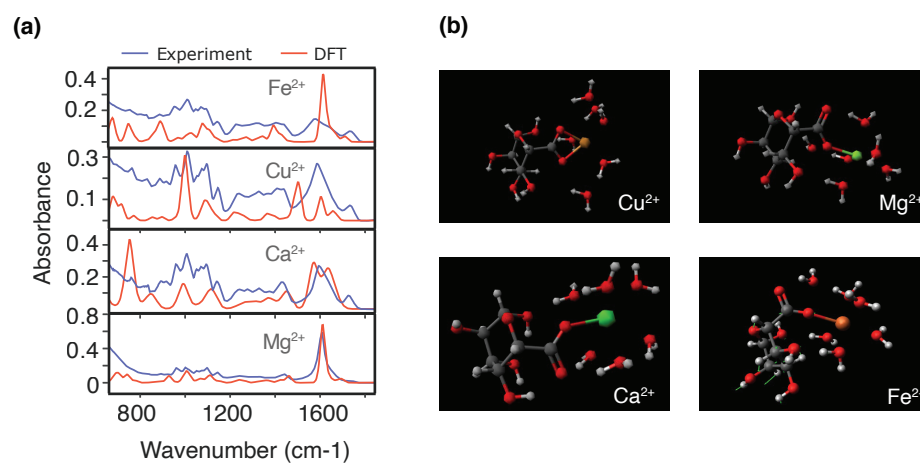
Figure A.2: DFT calculation. (a) Comparisons between IR spectra generated by DFT and IR spectra measured experimentally. Blue lines correspond to the experimental results and red lines correspond to the DFT calculation.(b) Optimized geometries for galacturonate-metal-ion-water complexes.

A p p e n d i x B

SUPPORTING MATERIALS FOR CHAPTER 4

The work presented in this chapter has been adapted from:

- Linghui Wang, and Chiara Daraio. Effect of water content on the ion transport in pectin films. *In preparation*, 2023.

For the impedance data, the conductivity was calculated by $\sigma = \frac{V}{I}\frac{d}{A}$, where V is the applied voltage, I is the measured current, d is the thickness of the sample and A is the area of the gold electrodes. The parasitic effect of the circuit has been verified to have little effect on the measured impedance spectra. DC ionic conductivity corresponds to the real part of the conductivity in the plateau region of the frequency spectrum. Specifically, in the model-free approach, we first interpolated the loss tangent curve and the real conductivity spectrum. Then, the DC conductivity is identified as the real conductivity at the frequency where loss tangent peaks[23]. In the model-fitting approach, we fit the real and imaginary parts of the conductivity at the same time to the complex conductivity model. Mean squared logarithmic error(MSLE) was used as the loss function for the nonlinear regression. The usual mean squared error was not chosen here because our impedance data span several orders of magnitude in conductivity. Minimizing the mean squared error always led to overfitting of the high conductivity region and large percentage error in the low conductivity. To find the global minimum of the fit, we used basin hopping minimization. We also computed 68.27% confidence level for all the fitting parameters using the covariance matrix.

For the linear fitting between σ_{CTRW} and f_{CTRW}, orthogonal distance regression was used with standard deviation in both terms taken into account.
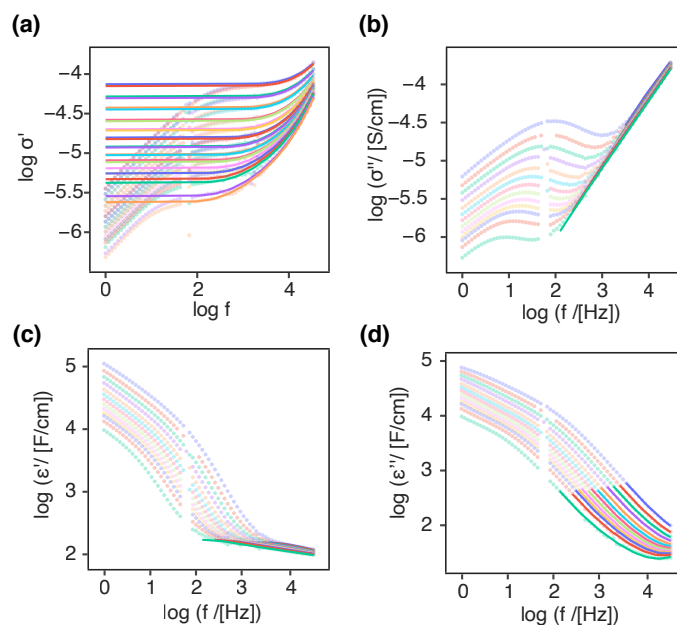
Figure B.1: Impedance and Dielectric Spectra. (a) The real part of conductivity spectra. Faded dots correspond to the measured data, and lines correspond to the fitting of CTRW+Debye model. Here fitted curves are extended to show how the model behaves at unfitted, lower-frequency regions. Since the electrode polarization effect is not included in this model, fitted curves show plateaus at that region as expected. (b) The imaginary part of conductivity spectra. (c) The real part of the dielectric spectra. (d) The imaginary part of the dielectric spectra.

A p p e n d i x   C

SUPPORTING MATERIALS FOR CHAPTER 5

The work presented in this chapter has been adapted from:

A

| 1 2-Hydroxyethyl acrylate | 2 *tert*-Butyl acrylate | 3 S,S-Dibenzyl trithiocarbonate |

AIBN
75 °C

4 *n*-butyl acrylate

Macro CTA Polymer 'A' block protected

AIBN
75 °C

Polymer 'ABA' block protected

DCM,TFA
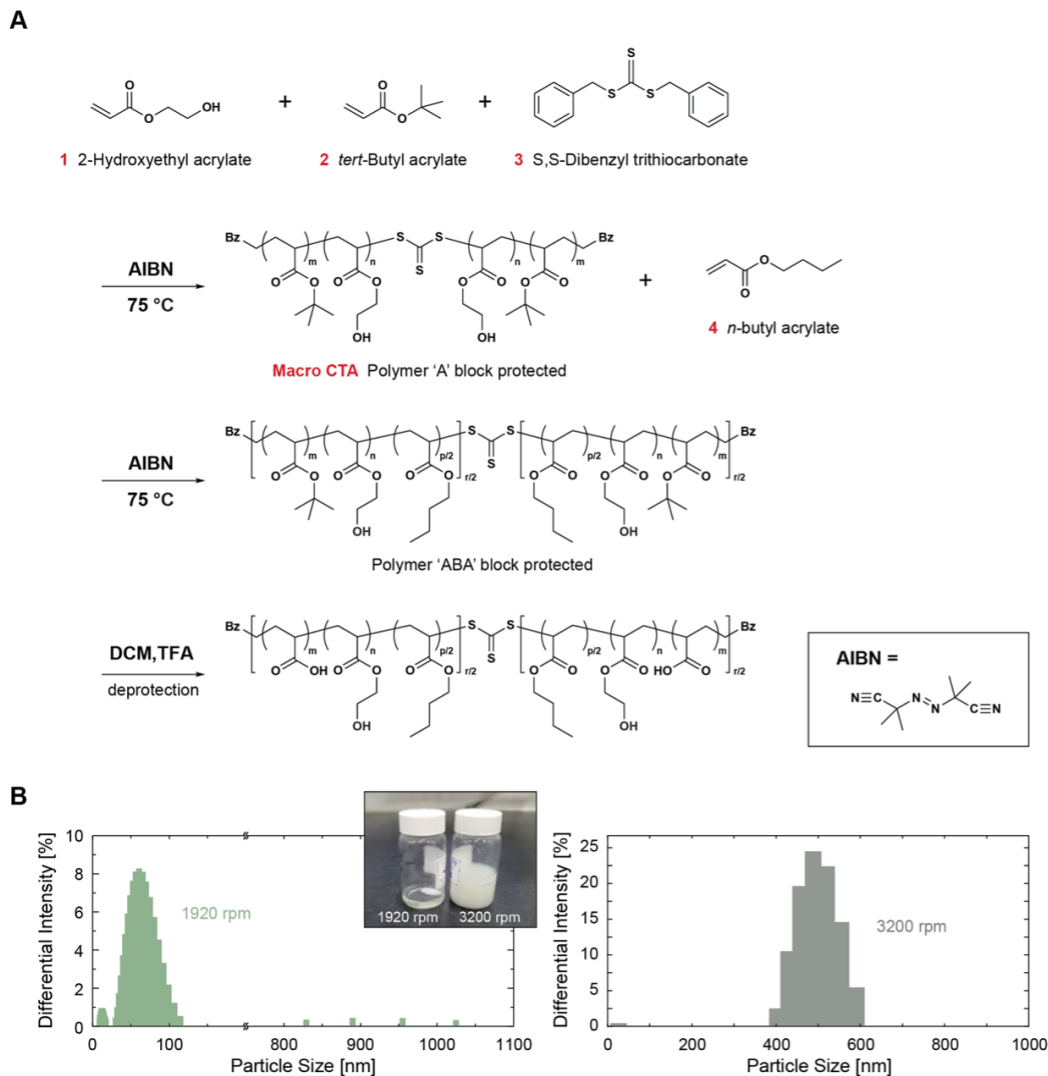deprotection

AIBN =

B

Figure C.1: Synthesis procedure of the ABA type block copolymers. (A) ABA type block copolymers are prepared via a reversible addition-fragmentation chain transfer (RAFT) polymerization method. (B) Increasing the rotation speed during sample vortex, the polymer solution became opaque. This change in opacity relative to the mixer speed is a typical behavior found in emulsion systems through Ostwald Ripening, indicating that the synthesized polymer exists in colloidal states in ethanol. The particle size in the transparent (left, 1920 rpm) and opaque solution (right, 3200 rpm) is 97 ± 29 nm and 491 ± 151 nm respectively.
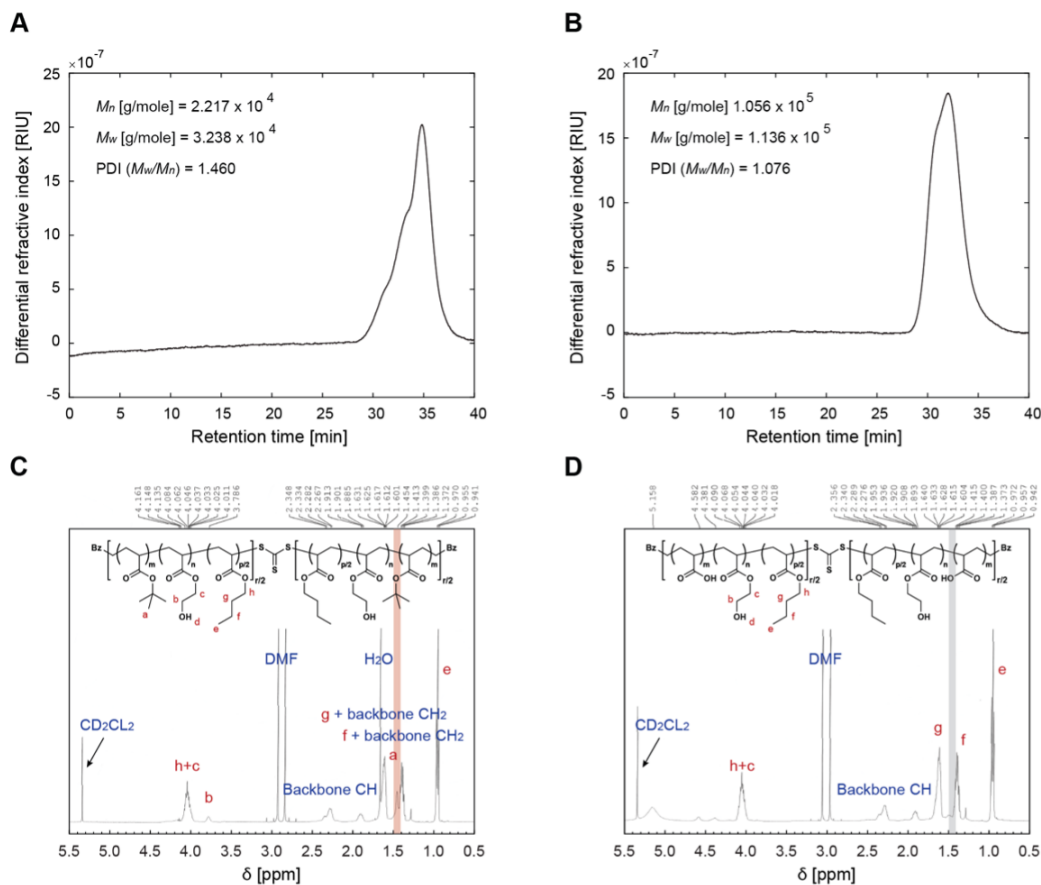
Figure C.2: Polymer characterization using GPC and NMR. (A) GPC traces of bis[p(t-BA-r-HEA)$_{10}$] trithiocarbonate (macro-CTA) and (B) p[(t-BA$_5$-r-HEA$_5$)-b-(n-BA)$_1$00-b-(t-BA$_5$-r-HEA$_5$)]$_r$ (deprotected copolymer). The weight average molecular weight (M$_w$) and number average molecular weight (M$_n$) of the final deprotected block copolymer are high and comparable to that of pectin, but with a very narrow molecular weight distribution (dispersity = M$_w$/M$_n$). Because of this narrow dispersity, the molecular weight distribution effect can be neglected while comprehending the thermal sensing properties and the mechanical performance of the block copolymer. (C) ^{1}H NMR spectrum of p[(t-BA$_5$-r-HEA$_5$)-b-(n-BA)$_{100}$-b-(t-BA$_5$-r-HEA$_5$)]$_r$ dissolved in CD$_2$Cl$_2$, prior to deprotection of tert-butyl group. (D) 1H NMR spectrum of p[(AA$_5$-r-HEA$_5$)-b-(n-BA)$_{100}$-b-(AA$_5$-r-HEA$_5$)]$_r$ dissolved in CD2Cl$_2$, after deprotection of tert-butyl group. The disappearance of the peak at 1.45 ppm indicates complete removal of tert-butyl group, resulting in free acid.
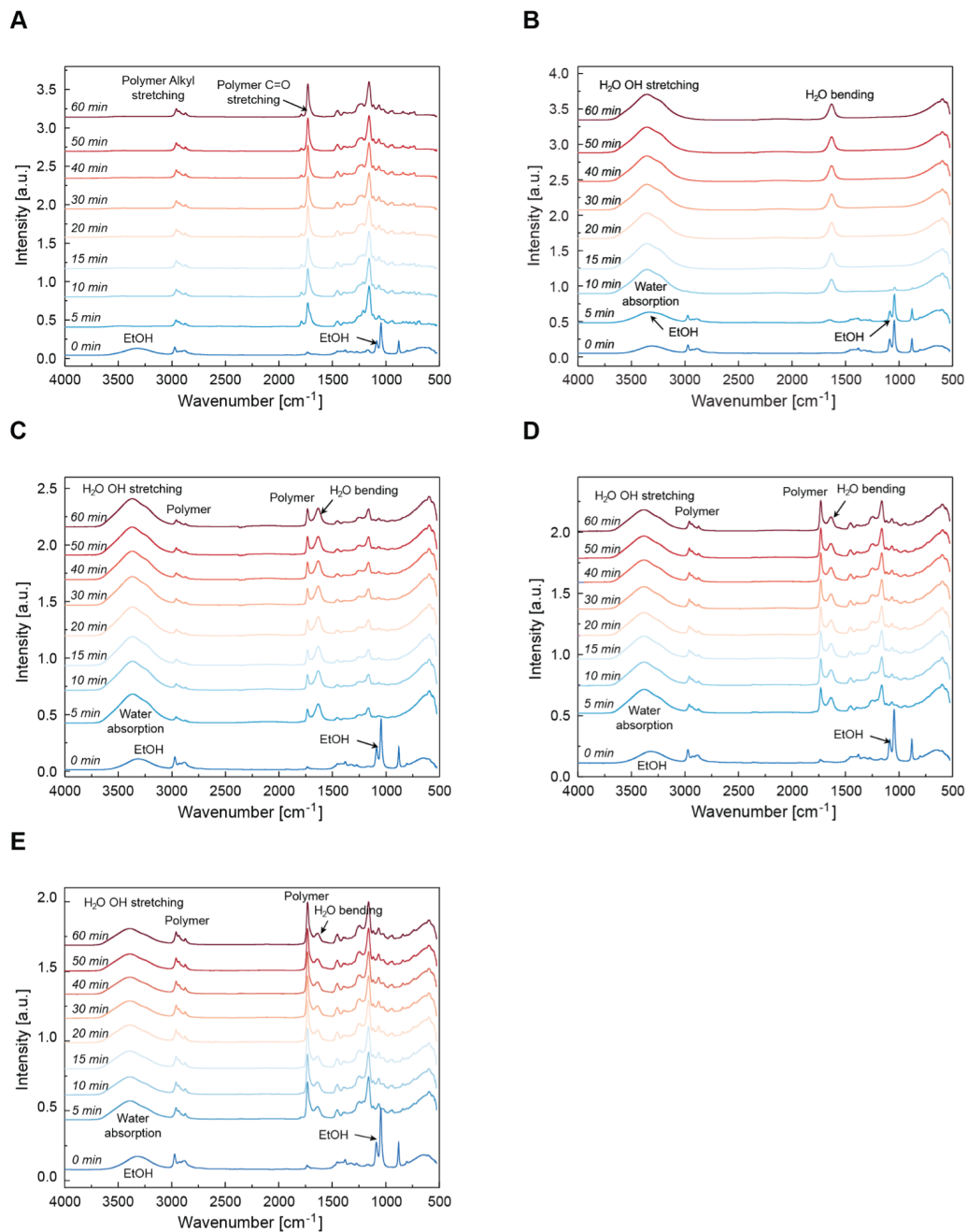
Figure C.3: Caption next page.

Figure C.3: ATR-FTIR spectra of the block copolymer and CaCl$_2$ dissolved in ethanol, and the block copolymer-metal ion complex. Prior to observing the in-situ film formation behavior of the block copolymer-metal ion complex, the ATR-FTIR spectra of each component is measured for control and plotted with respect to drying time: (A) the block copolymer and (B) CaCl$_2$. In both cases, ethanol evaporates with less than 10 minutes. After this solvent removal, water molecules are absorbed on the metal ions, whereas no water absorption is observed in the block copolymer. ATR-FTIR spectra of the composite mixture of block copolymer with (C) 50 %, (D) 25 %, and (E) 10 % concentration of CaCl$_2$ (Table C.6) plotted with respect to drying time. In the beginning, characteristic peaks of the solvent, ethanol, appear dominantly on the spectrum; O-H stretching (3314 cm^{-1}), CH stretching (2972 cm^{-1} - 2878 cm^{-1}), and C-O stretching (1087 cm^{-1} and 1045 cm^{-1}), respectively. However, after 5 minutes, the peaks near the O-H stretching region broaden due to water absorption (3678 cm^{-1} - 3011 cm^{-1}) and peaks initially assigned to the CH stretching and C-O stretching disappear. Ethanol evaporation and water absorption occur very fast due to the relative hydrophobicity of polymer. Meanwhile new peaks also emerge; H$_2$O bending (1636 cm^{-1}); CH3 stretching of n-BA (2958 cm^{-1}), CH stretching of AA (2934 cm^{-1}), CH2 stretching of HEA (2873 cm^{-1}); C=O stretching of n-BA (1730 cm^{-1}), AA (1723 cm^{-1}), HEA (1719 cm^{-1}); C-O stretching of n-BA and HEA (1065 cm^{-1} and 1160 cm^{-1}). The arising new peaks correspond to the ABA block copolymer. The unique H$_2$O bending peak at 1636 cm^{-1} from the ATR-FTIR spectra after 1 hour elucidates that the intensities around 3678 cm^{-1} - 3011 cm^{-1} are due to water molecules absorbed on CaCl$_2$, confirming complete removal of ethanol.
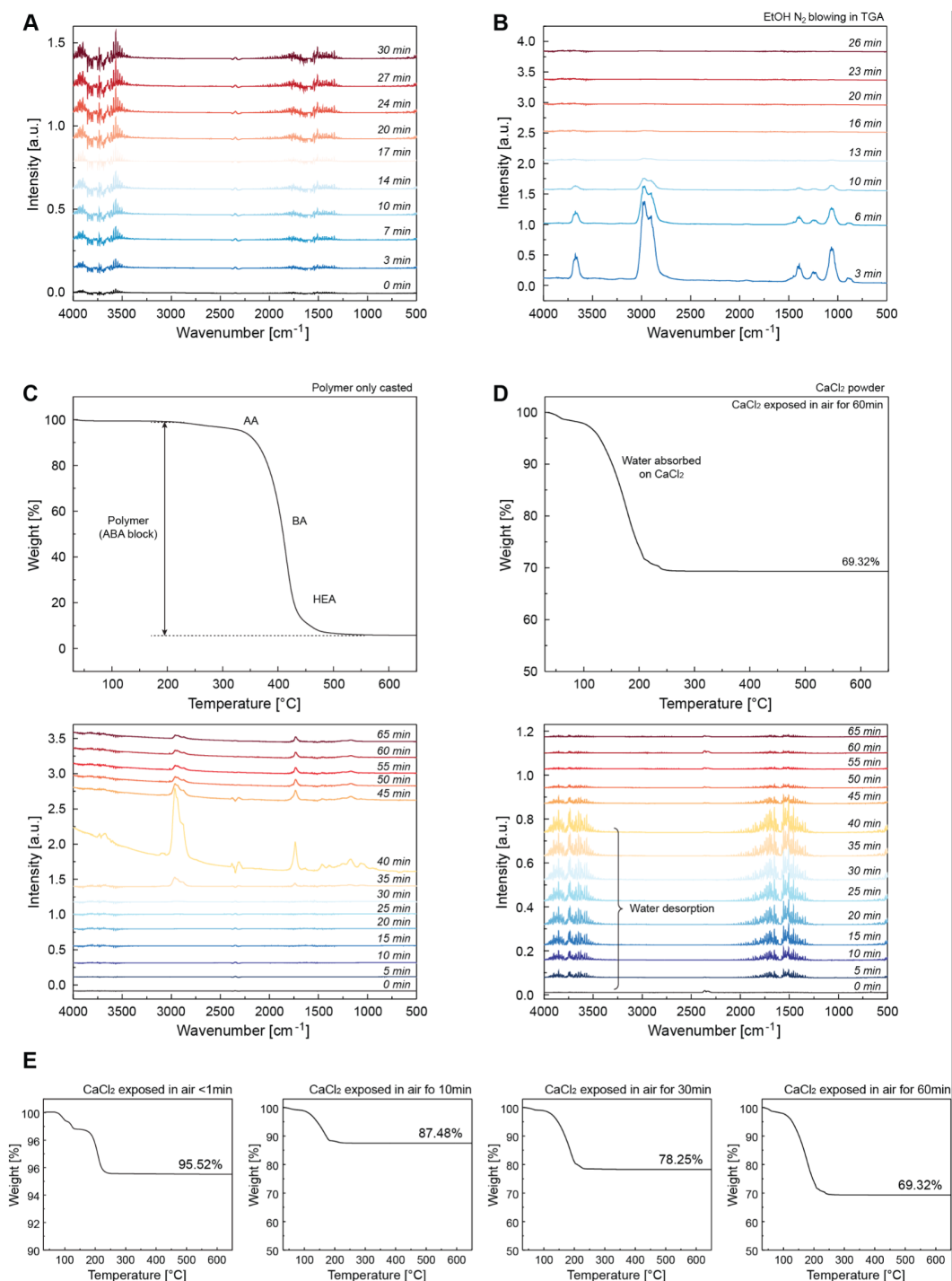
Figure C.4: Caption next page.

Figure C.4: TGA-FTIR spectra of water, ethanol, the block copolymer casted film, and CaCl₂ powder. TGA-FTIR spectra of (A) water and (B) ethanol plotted over time to distinguish the gas-phase materials diffused from TGA. The gas-phase FTIR spectra of water shows discrete peaks in the temperature range of 30 ℃ - 250 ℃. Ethanol exhibits a strong alkyl stretching (3056 cm^{-1} - 2746 cm^{-1}) and OH vibration (3747 cm^{-1} - 3574 cm^{-1}) when purged with N_2 at RT. (C) TGA profile and the corresponding FTIR spectra of the non-crosslinked polymer solution previously dried for 12 hours. A first plateau appears in the temperature range of 30 ℃ - 210 ℃, followed by a dip in the weight loss at 210 ℃ - 500 ℃, indicating polymer degradation. A second plateau appears between 500 ℃ - 650 ℃ (residue: 5.798 %). No sign of water is detected even after an additional 12 hours of drying time. (D) TGA profile and the corresponding FTIR spectra of $CaCl_2$. The first, stepwise weight loss is observed below 210 ℃, revealing the presence of water molecules absorbed on the metal ions. This is further confirmed from the gas phase FTIR spectra. Later, a slow weight loss is detected between 210 ℃ - 650 ℃. (E) TGA profiles of $CaCl_2$ powder exposed in air for different time period. The water absorbed on the metal ions increases with increasing time of exposure to the atmosphere.
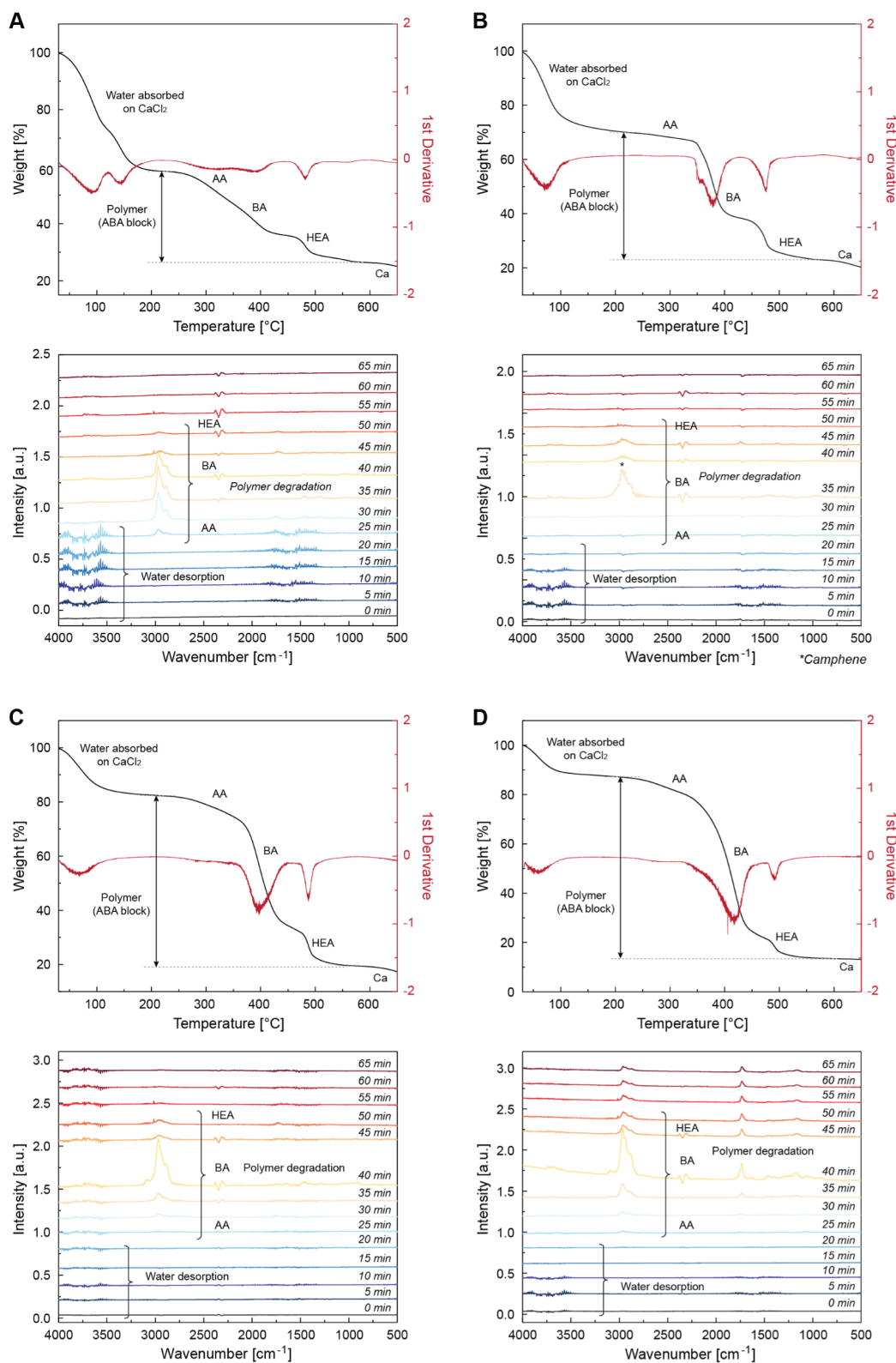
Figure C.5: Caption next page.

Figure C.5: TGA-FTIR spectra of the block copolymer-metal ion complex. TGA profiles and corresponding gas-phase FTIR spectra of the composite film formed using the ionically crosslinked block copolymer solution with varying amount of $CaCl_2$ concentration: (A) 100%, (B) 50 %, (C) 25 %, and (D) 10 % (Table C.7). The films are dried for 12 hours before measurement. The first weight loss appears between RT and 210 °C and represents the evaporation of the water molecules bound to $CaCl_2$, as shown in the characteristic peaks of the gas-phase FTIR spectra measured in the first 20 minutes. The following weight loss observed in the temperature range between 210 °C - 550 °C corresponds to the degradation of the block copolymer (AA, n-BA, HEA, and IPC), which is confirmed from the gas-phase FTIR spectra observed between 25 to 55 minutes (46–48). Finally, the slow weight loss detected in the range of 550 °C- 650 °C is caused by $CaCl_2$, confirmed by the gas-phase FTIR spectra between 55 to 65 minutes. The corresponding temperature of these events are identified by the 1st derivative of the TGA profile (red line). As the amount of $CaCl_2$ is increased, the following amount of water adsorbed in the polymer matrix increased, showing a linear relationship of $R^2 = 0.987$.
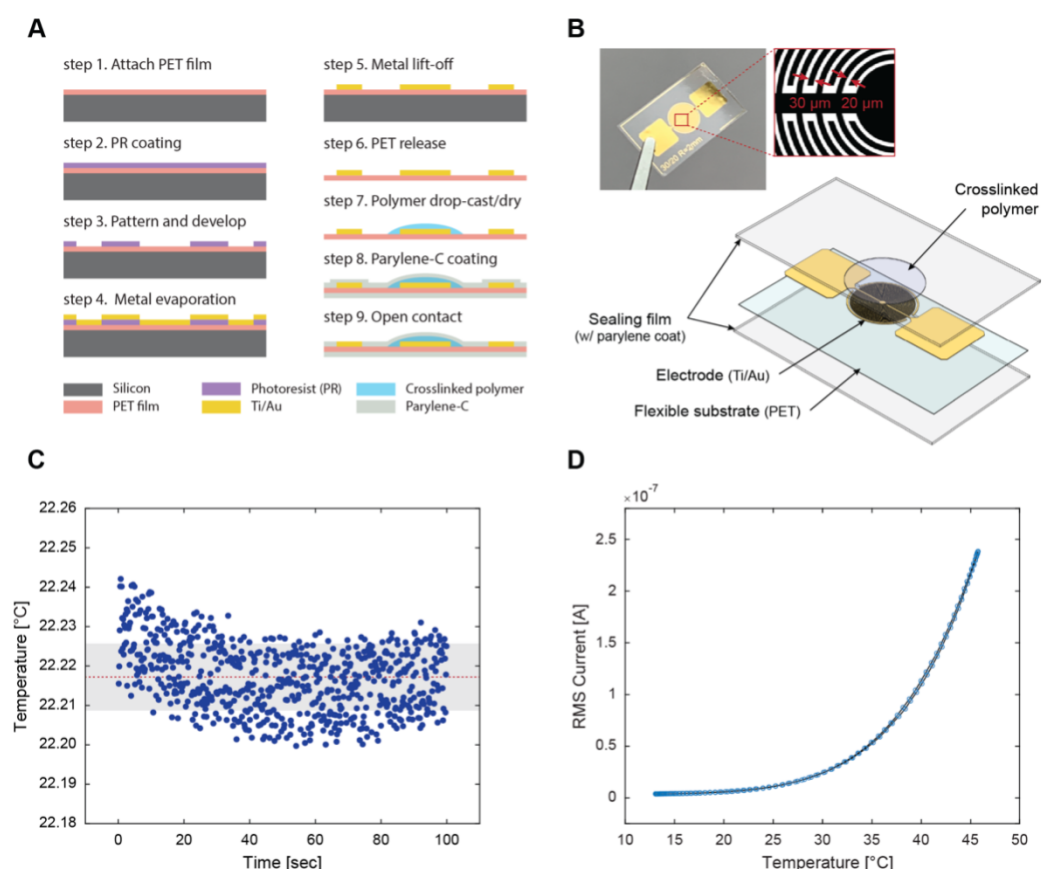
Figure C.6: Schematic and fabrication process of the block copolymer temperature sensor and the measured noise level and hysteresis curve. (A) Device fabrication procedure. (B) Schematic (bottom) and optical image (top) of the fabricated sensor. (C) Temperature variation measured in air. The sensor's sensitivity is derived by calculating the standard deviation of the temperature fluctuation measured while placing the sensor on a constant temperature reservoir for 100 seconds. AC voltage of 300 mV used at 200 Hz for readout. (D) The sensor displays negligible hysteresis in the current readout.
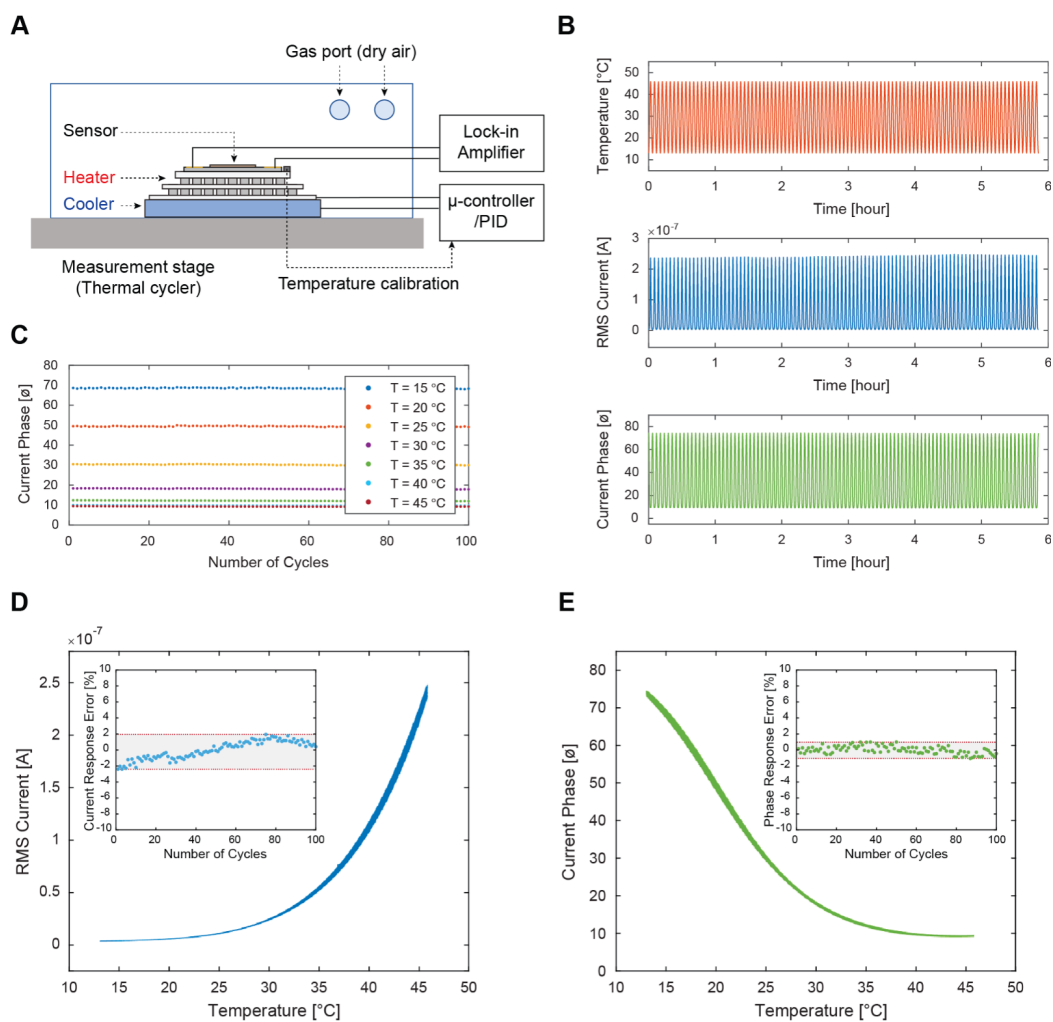
Figure C.7: Cyclic stability characterization of the block copolymer temperature sensor. (A) Schematic of the measurement set up. (B) Profile of the temperature cycles applied over time and the recorded RMS current and phase. (C) Current phase plotted by temperature during the 100-cycle measurement. Overlaid (D) RMS current (E) and phase recorded during 100 cycles of continuous measurement. Inset: The current response error and phase error between each cycle.
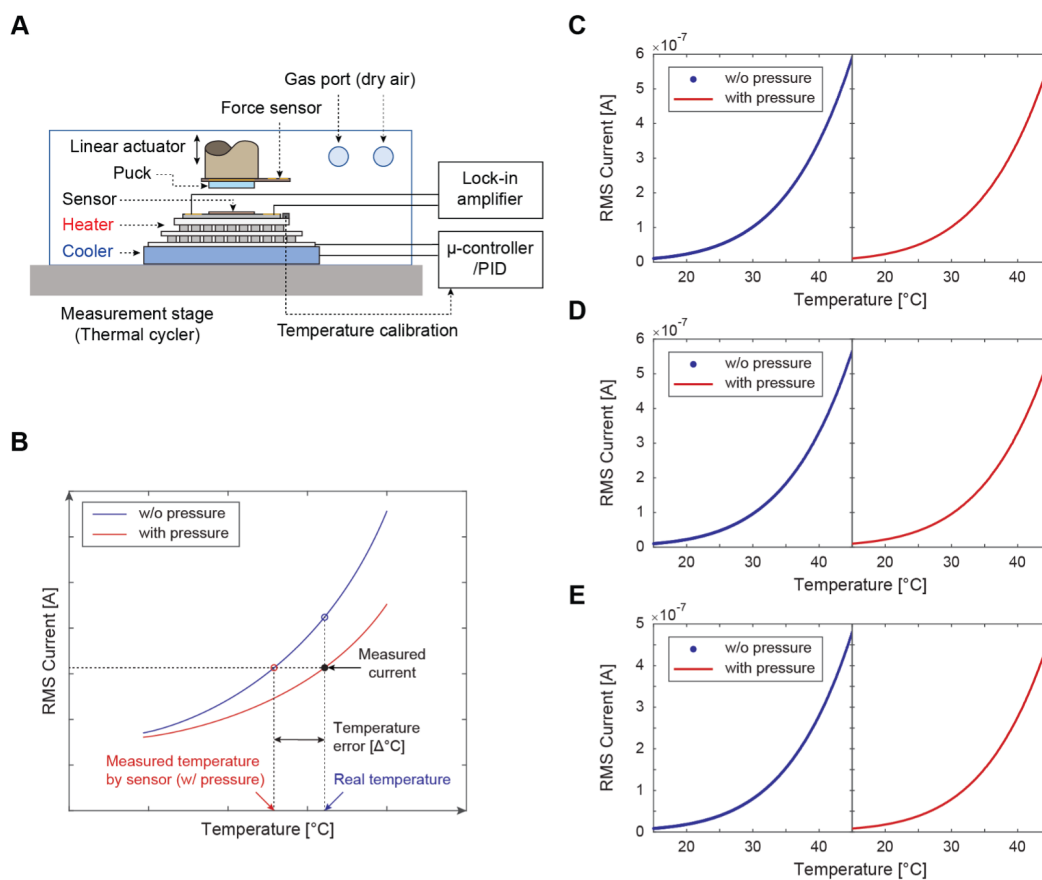
Figure C.8: Effect of normal strain on the block copolymer temperature sensor. (A) Schematic of the measurement set up. An external pressure is applied through a linear actuator vertically placed on top of the sensor. (B) Diagram illustrating method for calculating temperature error induced by the applied external pressure. The blue line represents the ideal RMS current measured when no pressure is applied, while the red line represents the RMS current measured when external pressure is applied. Current as a function of temperature measured with and without (C) 2.5 kPa, (D) 25 kPa, and (E) 250 kPa of normal pressure applied to the sensory material.

Hydrophilic and hydrophobic groups in the 'A' block		Group number (a)	Number of group number (b)	(a) x (b)
Hydrophilic	ester (free)	2.4	0.934	2.24
	-COOH	2.1	1	2.1
	OH (free)	1.9	0.934	1.77
	-O-	1.3	0.934	1.21
Hydrophobic	CH-	-0.475	1.934	-0.91
	-CH2-	-0.475	3.802	-1.80
HLB value of the 'A' block (Davies' method)		$HLB = 7 + \sum_{n=1}^{m} H_i - n \times 0.475$		13.03

Table C.1: HLB calculation of the polymer's 'A' block. m corresponds to the number of hydrophilic groups in the molecule; n corresponds to number of lipophilic groups in the molecule; H_i corresponds to value of the ith hydrophilic group.

Functional Groups	d [ppm]	Protected Intensity	Deprotected Intensity
h+c (n-BA, HEA, Methylene (CH2) -OC(=O)-C)	4.01 - 4.09	0.71	0.68
b (HEA, Methylene (CH2) -O)	3.78 → 4.38	0.1	0.08
Backbone (Methine (CH))	2.26 - 2.34	0.35	0.35
Backbone (Methylene (CH2))	1.88 - 1.91	0.18	0.18
g+Backbone (n-BA, Methylene (CH2))	1.60 - 1.63	0.94	1.06
a (t-BA, Methyl (-CH3))	1.45	0.37	(trace)
f+Backbone (n-BA, Methylene (CH2))	1.38 - 1.41	0.70	0.73
e (n-BA, Methyl (CH3))	0.94 - 0.97	1	1

Table C.2: ^{1}H NMR measurement of the synthesized polymer. The monomer ratio of the as-synthesized copolymer (protected form) was determined by the peak ratio between HEA ethylene (b, 3.78 ppm) and t-BA methyl (a, 1.45 ppm) as well as n-BA methyl (e, 0.94 - 0.97 ppm) and t-BA methyl (a, 1.45 ppm): HEA/t-BA = (b/2)/(a/9) = 0.97, n-BA/t-BA = (e/3)/(a/9) = 8.1 (Fig. C.2 c, d). The conversion of t-BA to AA was confirmed by the disappearance of t-BA methyl (a, 1.45 ppm) peak after the reaction with TFA in the deprotection step. (Deprotection rate = 100 %)

Monomer	Feed mole [μmol] (molar ratio)	Measured NMR ratio	Molecular weight [g/mol]	Adjusted mass of monomers with NMR ratio [g/mol]	Calculated mass of copolymer [g/mol]	Monomer numbers in the copolymer chain
HEA	10 (1)	0.97	116	112.64	9,292.4	80
t-BA	10 (1)	1	128.17	128.17	10,981.5	86
n-BA	100 (10)	8.1	128.17	995.88	85,326.1	694
Sub sum	120 (12)	10.07	372.34	1,236.69	105,600	860

Molecular weight GPC (Mn) [g/mol]	Mass of repeating unit [g/unit]	Repeating unit numbers in the block copolymer chain
105,600	1,236.69	85.4

Table C.3: Estimation of repeating unit numbers based on the NMR spectrum.

0 min	3314 [cm⁻¹]	2972 [cm⁻¹]	2927 [cm⁻¹]	2878 [cm⁻¹]	Polymer Film + CaCl₂										1087 [cm⁻¹]	1045 [cm⁻¹]
Assign	OH Stretching EtOH	CH Stretching EtOH													C-O stretching EtOH	
5 min	3610 - 3200 ①	2958 ②	2934 ②	2872 ②	1729 ③	1723 ③	1719 ③	1634 ④	1454 ⑤	1397 ⑥	1378 ⑥	1246 ⑦	1160 ⑦	1065 ⑧		
10 min	3610 - 3200	2959	2933	2872	1730	1723	1719	1636	1450	1397	1378	1243	1160	1065		
15 min	3610 - 3200	2958	2934	2873	1730	1723	1719	1634	1450	1397	1378	1245	1160	1065		
20 min	3610 - 3200	2958	2934	2873	1730	1723	1719	1636	1450	1397	1378	1243	1160	1065		
30 min	3610 - 3200	2958	2934	2873	1730	1723	1719	1636	1450	1397	1378	1243	1160	1065		
40 min	3610 - 3200	2958	2934	2873	1730	1723	1719	1636	1450	1397	1378	1245	1160	1065		
50 min	3610 - 3200	2958	2934	2873	1730	1723	1719	1636	1450	1397	1378	1243	1160	1065		
60 min	3610 - 3200	2958	2934	2874	1730	1723	1719	1636	1454	1397	1378	1242	1160	1065		
Assign	Free OH (3630 - 3670 cm⁻¹) Dimer OH (OH-OH) Intramolecular OH (OH-O=C) (3540 - 3550 cm⁻¹) Intermolecular OH (3400 - 3450 cm⁻¹) OH Stretching HEA+AA+H₂O on Ca Aggregate OH (3240 - 3280 cm⁻¹)	CH₃ Stretching n-BA	CH Stretching AA	CH₂ Stretching HEA	C=O Stretching (Interpolymer Complex, IPC) n-BA 1730 cm⁻¹ AA 1723 cm⁻¹ HEA 1719 cm⁻¹			H₂O Bending	CH in-plane bending n-BA	C-O-H Deformation AA		C-O Stretching n-BA	C-O Stretching HEA AA (IPC)	C-O Stretching HEA		

Table C.4: ATR-FTIR peak assignment

Materials	Percentage of CaCl₂ mixed			
	100 %	50 %	25 %	10 %
ABA block copolymer (140 mg/10 mL)	100 mL	100 mL	100 mL	100 mL
Ca (1 M in EtOH)	52 mL	26 mL	13 mL	6.5 mL

Table C.5: Composition of the tested mixtures during the ATR-FTIR and TGA-FTIR spectra measurement.(in-situ monitoring of film formation)

Material	Molecular weight [g/mol]	Input solution volume [µL]	Mass in input solution [g]	Number of molecules	Number of repeating unit	Total number of AA and Ca^{2+} ions input
Polymer	105600	99.90	1.40×10^{-2}	7.95×10^{16}	85.7	6.81×10^{19}
CaCl$_2$ (100 %)	110.98	172.80	5.75×10^{-3}	3.11×10^{19}	1	3.11×10^{19}

Number of bound Ca^{2+}	3.11×10^{19} x 11.62 %	0.36×10^{19}
Number of bound AA	(Number of bound Ca^{2+}) x 2	0.72×10^{19}
Number of AA that can form IPC	6.81×10^{19} – (Number of bound AA)	6.09×10^{19}
Maximum number of AA involved in IPC formation	(Number of AA that can form IPC) x 0.97 * AA to HEA ratio in polymer = 0.97	5.91×10^{19}

Free AA (Ca^{2+} bound)	0.72×10^{19} / 6.81×10^{19} x 100	10.61 %
AA forming IPC	5.91×10^{19} / 6.81×10^{19} x 100	86.13 %

Table C.6: Percentage of IPC formed in the composite film. Number of AA functional groups and Ca^{2+} ions in the polymer-CaCl$_2$ solution mixture (top). Estimating the number of AA involved in Ca^{2+} binding and IPC formation based on AA-Ca^{2+} titration analysis (middle). Percentage of AA forming IPCs in the composite film (bottom). The total number of bound Ca^{2+} is first calculated based on the total number of input metal ions and the percentage of the unwashed portion measured during titration analysis. By subtracting the total number of Ca^{2+} bound AA to the total number of AA present in the BTS polymer, the amount of AA that can form IPCs can be obtained. Since the AA to HEA ratio in the polymer is 0.97, the maximum number of AA that can engage in the IPC formation becomes 5.91×10^{19}. Finally, the percentage of AA that forms IPC can be calculated by dividing this value with the total number of AA existing in the block copolymer.

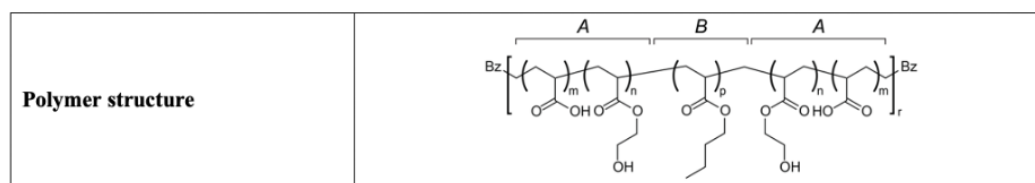|	Type 1	Type 2	Type 3
AA:HEA ratio	5:5	4:7	10:0
Amount of AA + HEA content	10	11	10
Amount of AA content	5	4	10
Amount of IPC content	5	4	0
Polymer structure			

Table C.7: Composition of the three different types of polymers synthesized for response comparison.

A p p e n d i x   D

SUPPORTING MATERIALS FOR CHAPTER 6

The work presented in this chapter has been adapted from:

- Linghui Wang, Vincenzo Costanza, Nick Higdon, Tae Hyun Kim, and Chiara Daraio. Ion transport phenomena in thermally responsive polyelectrolytes. *In preparation*, 2023.

Density Functional Theory (DFT) Calculation

In-order to evaluate the potential mechanisms of ion conduction and the origin of the temperature response behavior, binding energy was evaluated in density functional theory (DFT) studies (Table D.1). Due to the complexity of ion binding in the polymer system, crude model complexes were constructed that we believe will approximate the possible binding energies of individual ligating atoms. We do not believe that these models capture the actual binding energies of the ions to our polymer, however they provide approximate numbers to evaluate the relative strengths of the interaction energies. While the inclusion of solvent dramatically effects the binding energies, due to the typically dry state of the polymer the significance of these results in the experimental system are questionable. Due to the crudeness of these models and their relatively small contributions (based on prior calculations by the authors on related complexes), we selected to not apply a diffuse basis set, nor account for basis set superposition exchange.

	ΔE **(kJ/mol)**		
	Simple	**Dispersion**	**Dispersion + Solvent**
Acetate + H_3O -> Acetic + H_2O	-770.2478984	-771.0995595	-159.160797
Ca(OH$_2$)$_7$(OH) + H$_3$O -> Ca(OH$_2$)$_8$ + H$_2$O	-33.64510117	-29.38277016	-161.1668762
Ethanol + Cl -> Ethanol-Cl	-79.39251464	-85.26912124	-20.16709658
Acetic + Cl -> Acetic-Cl	-95.56442033	-101.0382359	-22.59774426
Ca + Cl -> CaCl	-1253.876986	-1263.892656	-143.3417044
Ca + Acetic -> Ca(acetic)	-353.1909149	-367.4831333	-98.73297116
Ca + Acetate -> Ca(acetate)	-1373.59385	-1382.246964	-218.8853694
Ca + Acetic + H$_2$O -> Ca(acetate) + H$_3$O	-603.3459513	-611.1474049	-59.72457244
Na + acetic -> Na(acetic)	-129.047022	-134.8789723	-23.10550503
Na + acetate -> Na(acetate)	-627.5335146	-632.8476863	-58.25160357
Na+acetic + H$_2$O -> Na(acetate) + H3O	142.7143839	138.2518732	100.9091934

Table D.1: Binding energies calculated using DFT.

Differential Scanning Calorimetry (DSC)

Thermal measurements were conducted using Differential Scanning Calorimetry 250 from TA instruments. Nitrogen gas purging was set at 50ml/min flow rate. 40 μL HEAAA was deposited in a Tzero aluminium pan. After dehydration in a nitrogen box at room temperature over 24 hours, its weight was measured to be 3.3 mg. The temperature scanning was performed at 10 °C/min, cycling from -40°C to 100 °C. During the measurement, the remaining water in the sample evaporates at high temperature. After the DSC scans, the weight of the sample decreased to 3.1 mg.

Gravimetric Measurement

Gravimetric measurements of the samples were performed via a precision quartz microbalance (openQCM Q-1, 5MHz). 500 nL of HEAAA with a concentration of 0.3 g/mL was deposited on the active area of the quartz (12 mm diameter) and dehydrated in a vacuum chamber for half an hour. The so prepared samples were kept overnight in a glove box flushed with nitrogen to eliminate excess ethanol and water from the polymer matrix. The resonance of the so prepared sample was then measured in the humidity box at different RH.

FTIR

P3A with calcium was drop cast onto a piece of silicon wafer and dried at 70 °C on a hotplate for several days. The sample was then stored in a desiccator. Transmission Fourier transform infrared spectroscopy (FTIR) was acquired on a Nicolet 6700 FTIR purged with nitrogen. A blank spectrum was taken on silicon wafer at several intervals over a 25 minute period to observe the removal of gases introduced during the sample placement. The spectrum taken at 25 minutes was used as the reference for calculating absorption of the sample. FTIR of the dried sample was then taken at several intervals over a 20 minute period. The spectrum taken at 20 minutes was used at the dried sample spectrum. The sample was then placed on an elevated platform in a sealed container with a small quantity of water, for 15 minutes. The sample was removed from the humidity chamber and FTIR was then taken at several intervals over a 180 minute period. The FTIR data was fit utilizing a custom python script for the data from 1519.66-1897.64 cm^{-1}. It was fit with 8 gaussian peaks and a linear background. Peak locations and widths were identically constrained for all fits, constraints were set by visual inspection of the data. Peaks at 1563 cm^{-1} and 1597 cm^{-1} were assigned to the calcium bound carboxylic acid. The peak at

1620-1630 cm^{-1} was assigned to water. The areas of the peaks were evaluated and plotted.

Impedance Spectrum

5 μL of HEAAA -CaCl$_2$(1g/mL) were then deposited on polyimide substrates, prepatterned with gold electrodes and dried under vacuum for half an hour. The so prepared samples were kept overnight in a glove box flushed with nitrogen to eliminate ethanol/water excess from the polymer matrix. The impedance spectra were acquired by an impedance analyzer (Zurich Instrument, MFIA 5 MHz). The samples were kept at room temperature (40 °C) for the whole duration of the experiment. This temperature was chosen in order to obtain an appropriate water content for the humidity range tested. In addition, to ensure that the water content reached the equilibrium we kept the samples at the specific humidity for 8 hours at 1Hz before starting the frequency sweep. After this time, we acquired the impedance spectra between 1 Hz and 5 MHz with different current ranges (i.e. 1 µA, 10 µA and 100 µA), to ensure the highest accuracy. The data sets were then merged. The humidity was increased from 5% to 50%. It should be noted that the data shown in this work, are presented in form of conductance rather than its dimensionless counterpart conductivity, given the planar geometry at which the measurements were performed. This might sound uncommon practice, however, when looking at the same sample, the ion conductivity will scale in the same way, therefore when calculating the slopes of group of points over frequency or measure temperature response, it will be independent from the geometry of the sample. We measured the impedance of the empty cell (comprising of the substrate, connectors and cables) and subtracted these values from the one of the full sample to eliminate parasitic effects arising from spurious capacitance (Fig. D.1).

Response Calculation

Temperature cycles on the films were actuated by a Peltier-Element (model Qc-31-1.4-8.5m). The temperature was independently measured with a Pt100 platinum resistance thermometer placed on the polyimide substrate near the polymer. The Pt100 sensors were previously calibrated with a FLIR thermal camera (A655SC). A PID controller was implemented to generate a sinusoidal temperature between 27 and 62 °C. The substrates and the reference Pt100 were electrically connected through an interface board that could be connected with the impedance analyzer and the temperature control board. The current was measured with the impedance
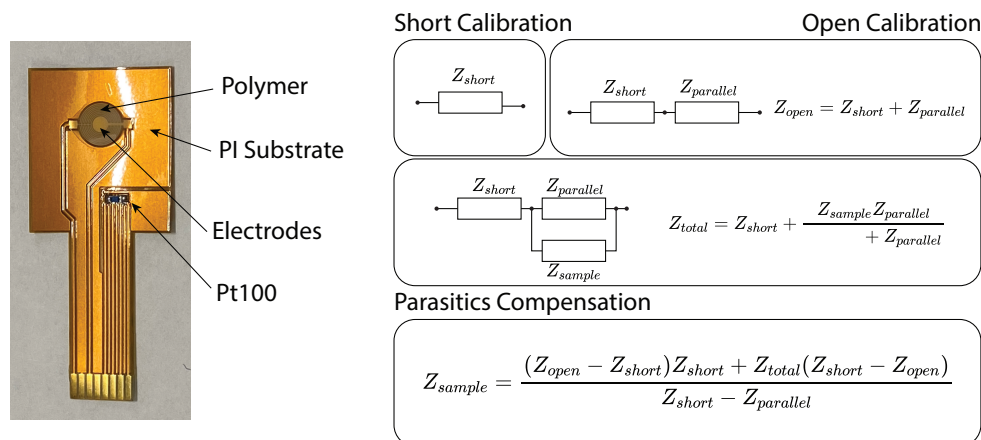
Figure D.1: Parasitics compensation. (a) Image of the substrates used for the impedance spectroscopy measurements. (b) Parasitics compensation procedure.

analyzer with an average sampling rate of 10 S/s. The temperature response as a function of frequency was isochronically measured: the frequency was kept constant within one temperature cycles and then changed to the next frequency at the next temperature cycle. The frequency was swept from 1 Hz to 500 kHz. To avoid the thermal hysteresis due to the sample mass we then considered only the increasing part of the temperature response and sampled the current at different temperatures. The real part of the temperature response after each thermal cycle were calculated as the ratio between the conductance measured at 62 °C and 27 °C. The humidity was kept constant for 10 hours and then switched to the next value. Relative humidity was swept from 5% to 20% in increase of 3%.

Almond-West formalism and Continuous Time Random Walk model comparison

In order to verify the accuracy of the fitted data we calculated the DC conductance and onset frequency using two different methods: the AW formalism and the CTRW model. For the AW the DC conductance G_{DC} was calculated from the intersection between the frequency corresponding to the maximum of the tangent loss and the conductance data. The onset frequency was then calculated as the frequency at which $G(\nu^*) = 2G_{DC}$ (Fig. D.2 (a)). Because of the limited frequency range, the spectra at RH higher than 35% could not be fitted using this method because the portion of the spectrum were the line $2G_{DC}$ intercepts the conductance were outside of the measured frequency range. On the other hand, the the DC conductance G_{DC} and the onset frequency ν^* using the CTRW model modified with a Debye relaxation term was calculated directly from the fitting of the data to the model (Fig. D.2 (b)).

The two onset frequencies slightly differ from each other (Fig. D.2 (c)). Nonetheless the relationship between the DC conductivity and the onset frequencies calculated with the two different method preserve the same shape (Fig. D.2 (d) and (e)).
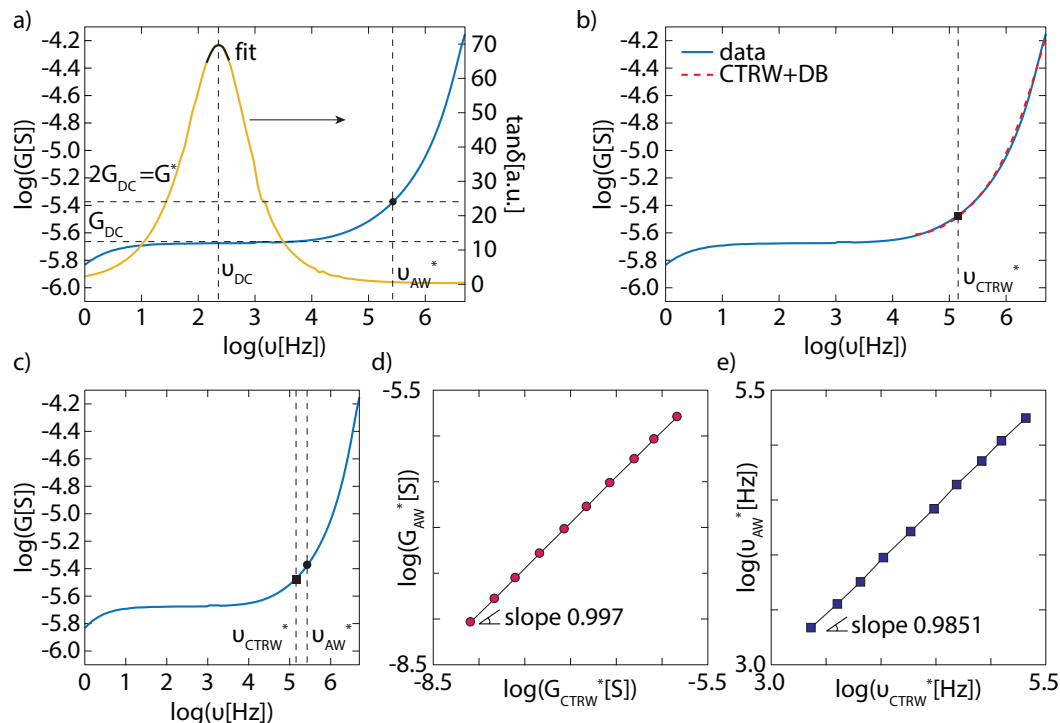

Figure D.2: Comparison between the AW formalism and the CTRW model to calculate the onset frequency and DC conductivity. (a) AW formalism to calculate v^* for a sample at RH 35%. The tangent loss $tan(\delta)$ was used to calculate σ_{DC}. (b) CTRW fitting and corresponding v^* for the same sample. (c) Comparison between the onset frequency calculated with the AW formalism and the CTRW model. The two onset frequency v^*_{AW} and v^*_{CTRW} are plotted on the correspective conductance plot. (d) Comparison between the DC conductivity $log(G^*)$ calculated with the two different methods for different humidity. (e) Comparison between the onset frequency $log(v^*)$ calculated with the two different methods for different humidity.

Data fitting

All the impedance data were corrected for the parasitic effect before the fitting routine using methods described above. Both the real and imaginary parts of the conductance data were used for the nonlinear regression (Fig. D.3). We chose the mean squared logarithmic error (MSLE) as the loss function because the fitted conductance spans several orders of magnitude over the measured frequency range and MSLE is a better measure to minimize the percentage error of our fitting. Basin hopping minimization method was used to find the global minimum of the loss function. 68.27% confidence level were calculated for all fitting parameters

using covariance matrix. For the linear fitting between DC conductivity and AC onset frequency, we used the orthogonal distance regression to take into account the uncertainties of both variables.

For the VTF fitting, we assume that G_0 is the same for measurements at all RH. Due to experimental constraints, the conductivity data were collected for a relatively small temperature range. Fitting B, T_0 and G_0 simultaneously, for each RH results in multiple local fitting minimums. Since G_0 is the conductance at the infinite temperature and is proportional to the concentration of all the possible current carriers in the system, it should not change with RH. Therefore, during the fitting we set G_0 as the shared parameter for all RH.
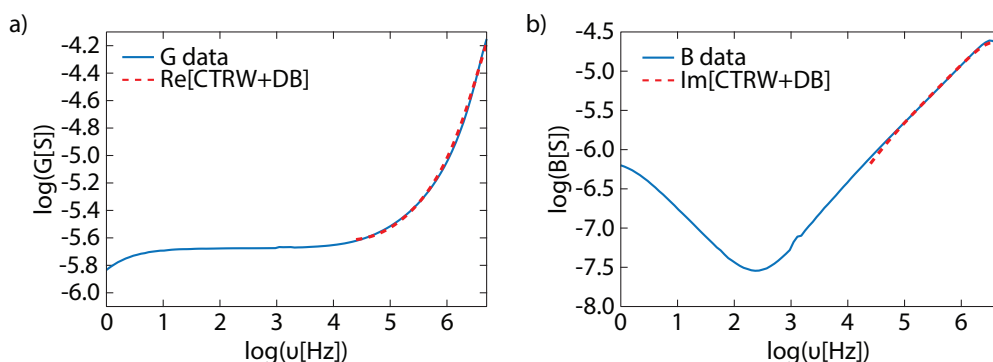

Figure D.3: Complex fit method. Complex fit results when compared to the sample's (a) conductance and (b) susceptance.

HEA-AA Only comparison

Samples were fabricated by depositing 5 μL of HEAAA (1g/mL) on the polyimide substrates and dried. Impedance spectrums were measured following the same steps described in the Impedance Spectrum section. The G_{DC} and v were extracted by fitting the Continuous Time Random Walk model as shown in figure D.4.

Time-Humidity-Superposition

To check whether impedance spectrum at various RH superimpose and follow the Summerfield scaling, we plotted them in the scaled axes :G/G_{DC} and v/G_{DC}. As shown in figure D.5, significant deviations could be observed in the dispersion regime. Time-Humidity-Superposition principle does not apply in our system because the ion hopping process and the high-frequency relaxation respond to humidity change differently.
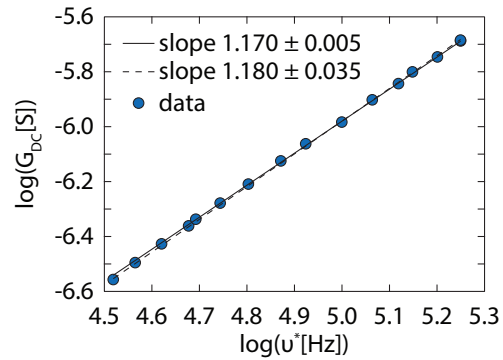
Figure D.4: Onset frequency vs onset conductance as a function of different RH (between 5% and 50%). The linear fit of 5 points at higher RH (50%,47%,44%,41%,38%) results in 1.180 ± 0.035. The slope of the rest of data points is 1.170 ± 0.005. Since this difference of these two slopes are within the confidence level, we claim that there is no change of the slope.
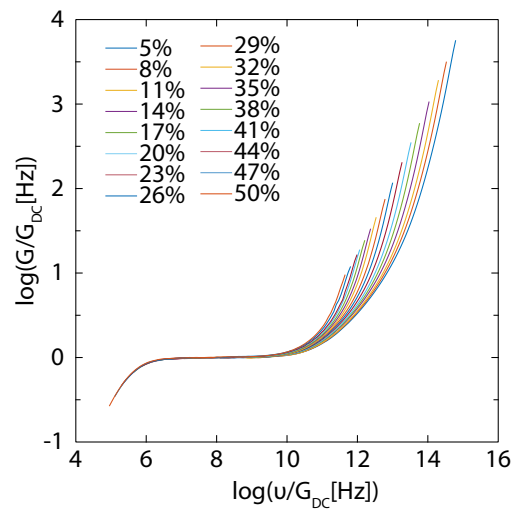

Figure D.5: Superimposed spectra at different RH.